



Influence of structural disorder on plasmonic metasurfaces and their colors—a coupled point dipole approach: tutorial

EDIZ HERKERT,^{1,2}  FLORIAN STERL,¹  STEFFEN BOTH,¹  SERGEI G. TIKHODEEV,^{3,4} 
THOMAS WEISS,^{1,5,*}  AND HARALD GIESSEN¹ 

¹4th Physics Institute and Research Center SCoPE, University of Stuttgart, Stuttgart 70569, Germany

²Institut de Ciències Fotoniques (ICFO), The Barcelona Institute of Science and Technology, Barcelona, Spain

³M. V. Lomonosov Moscow State University, Leninskie Gory 1, Moscow 119991, Russia

⁴A. M. Prokhorov General Physics Institute, Russian Academy of Sciences, Vavilova Street 38, Moscow 119991, Russia

⁵Institute of Physics, University of Graz, and NAWI Graz, Universitätsplatz 5, 8010 Graz, Austria

*thomas.weiss@uni-graz.at

Received 4 October 2022; revised 1 February 2023; accepted 4 February 2023; posted 6 February 2023; published 1 March 2023

The optical properties of plasmonic metasurfaces are determined not only by the shape and size of the constituting nanostructures, but also by their spatial arrangement. The fast progress in nanofabrication has facilitated the emergence of many advanced metasurface designs that enable controlling the propagation of light on the nanoscale. While simple metasurface designs can be derived from theoretical considerations, it is inevitable to employ computational approaches for complex manipulations of incident light. However, most of the currently available full-wave simulation approaches such as the finite element method (FEM) or finite difference time domain method come with drawbacks that limit the applicability to certain usually simplified or less complex geometries. Within this tutorial, different approaches are outlined for modeling light propagation in complex metasurfaces. We focus on an approach that approximates the nanostructure ensemble as a coupled set of point dipoles and determine their far-field response via the reciprocity theorem. This coupled point dipole approximation (CPDA) model is used to examine randomly distributed, oriented, and scaled nanostructure ensembles. A disorder formalism to introduce the randomness is developed that allows one to progressively perturb periodic arrangements of identical nanostructures and thereby investigate the effects of disorder and correlation. Several disorder metrics are provided that allow one to quantify the disorder, and the relation with the far-field scattering properties is discussed. Spatially and angle resolved hyperspectral datasets are computed for various disordered metasurfaces to assess the capabilities of the CPDA model for different polarization states and incidence angles, among others. The hyperspectral datasets are converted into sRGB color space to deduce the appearances in the image and FOURIER planes. Very good agreement of the simulation results with MIE theory, FEM results, and experiments is observed, and possible reasons for the present differences are discussed. The presented CPDA model establishes a highly efficient approach that provides the possibility to rapidly compute the hyperspectral scattering characteristics of metasurfaces with more than 10,000 structures with moderate computational resources, such as state-of-the-art desktop computers with sufficient memory; 16 GB allow for the simulations in this paper, whereas scaling to up to more memory by the factor of N^2 allows for the simulation of N times more dipoles. For that reason, the CPDA is a suitable approach for tailoring the bidirectional reflectance distribution function of metasurfaces under consideration of structural perturbations and experimental parameters. © 2023 Optica Publishing Group

<https://doi.org/10.1364/JOSAB.477169>

1. INTRODUCTION

The availability of increasingly powerful and affordable computational resources has opened up many new opportunities in science. Problems that do not have an analytical solution or require the evaluation of large datasets are particularly suitable to solve by computational models. The experimental

examination of such problems is often also possible, but is commonly associated with high cost and time expenses. Besides that, experiments can suffer from artifacts or unexpected effects originating from perturbations in the experimental setup. For that reason, it is often desirable to have simulation models that can be used to support the experimental findings or predict the possible experimental outcomes.

In the field of photonics, a variety of established computational methods exist that can be applied on a wide range of different problems. Some of the most commonly used approaches are the finite element method (FEM), finite integral technique (FIT), finite difference time domain (FDTD) method, volume integral method (VIM), surface integral method (SIM), and FOURIER modal method (FMM) [1–8]. All of these methods are powerful tools that can be used to efficiently and accurately tackle several challenges in photonics. However, depending on the use case, each of these methods exhibits disadvantages that make them unsuitable for solving the problem. The FEM, FIT, FDTD, and FDFD are differential equation solvers that often lack to provide the desired efficiency due to their precision and broad generality. This is particularly a problem for systems that consist of large amounts of coupled sub-units that could be approximated by much simpler descriptions. While the FMM can efficiently deal with periodically arranged plasmonic and dielectric systems, its conventional formulation breaks down for arbitrarily arranged structures without periodicity. Thus, none of the previously mentioned methods is ideal for this study, since we aim to find an approach that efficiently predicts the scattering properties of arbitrarily distributed, oriented, and scaled plasmonic nanostructure ensembles.

Tailoring disorder has proven to be a promising approach to enhance the performance of advanced photonic applications such as solar cells [9–11] or spectrometers [12,13] and for creating and understanding structural colors [14–17]. In many cases, we can learn directly from nature [18]. Also, significant advances have been achieved in fabricating disordered structures [19–23]. Because of that, it is of special interest to further understand the influence of disorder on optical scattering properties and thus gain more control over it. Since metasurfaces exhibit widely tunable scattering properties, they hold great promise to enable many new advanced applications in photonics. Optical metasurfaces are flat arrangements of dielectric or metallic nanostructures with different sizes and orientations that allow tailoring the light propagation in a layer of subwavelength thickness [24]. Thus, it is possible to control the phase and polarization of light beams, with applications such as flat lenses [25], holograms [26], or classical and quantum sensors [27,28]. Even chiral multilayer metasurfaces with tailored disorder can be fabricated nowadays [29]. However, the initial fabrication of metasurfaces can be very time consuming, so that their experimental examination is not an effective tool for rapid prototyping. For the reasons mentioned previously, many of the existing simulation approaches are also not suitable for this task.

More sophisticated approaches have to be developed for that purpose. One option would be to describe disorder via perturbation theory. Muljarov *et al.* propose using the resonant-state expansion to calculate resonant states, also known as quasi-normal modes, of a perturbed system from the resonant states of an unperturbed system [30,31]. In that case, the resonant states of the unperturbed system are used as bases to set up an eigenvalue problem, which results in resonance frequencies and resonant field distributions of the perturbed system as eigenvalues and eigenvectors, respectively. The unperturbed system can be a planar waveguide [32,33] or a spherical particle [34,35], and the perturbation can be rather large if the set of

basis resonant states is large enough. For instance, in Ref. [33], the resonant states of a periodic system are obtained from those of a planar slab. Alternatively, it is possible to obtain results for a metallic sphere from those of a dielectric system [34] or to switch from a spherical system to a disk [35]. While this approach is very flexible regarding geometrical modifications, it has been rarely demonstrated for modeling disordered systems consisting of several building blocks [36,37].

Alternatively, the Lemmer group in Karlsruhe has implemented a transition matrix (T-matrix) method that is optimized to be operated on graphic cards and allows for describing the interaction of thousands of spherical nanoparticles [38,39]. In that case, the analytic T-matrix for each nanoparticle is used to calculate the scattered field at each particle for a background field that consists of the incident field and the field scattered by all other spheres. While the number of nanoparticles can be rather huge, this approach has been rarely used to describe the interaction of nonspherical scatterers. In contrast, Abass *et al.* suggest a Green's function method for forward and inverse modeling of quasi-periodic nanostructured surfaces [40], which is well suited for surfaces with varying height profiles.

Lalanne *et al.* suggest analyzing resonant states and their eigenfrequencies based on a dipolar approximation of line scatterers to investigate effects such as light localization [41]. Similarly, the Gippius group has considered the coupling of nanoantennas in periodic arrangements based on a dipolar approximation [42]. This approximation is also the basis for the well-known discrete dipole approximation [2] and used to describe surface lattice resonances [43]. We combine the various advantages of these methods into our implementation of the coupled point dipole approximation (CPDA).

This CPDA model is capable of predicting the spectrally resolved angular and spatial scattering properties of disordered plasmonic metasurfaces by using the reciprocity theorem. While we have used this model already in a recent publication to predict the visible appearance of disordered metasurfaces [16], we provide in this tutorial the theoretical background and an implementation in PYTHON. The examined metasurfaces are perturbed with a novel disorder formalism that allows one to randomly change the location, orientation, and size of each nanostructure in a correlated or uncorrelated manner. The formalism is designed such that the disorder is progressively introduced, starting from the well-understood situation of periodically arranged nanostructures with equal dipolar properties. This enables us to slowly approach truly disordered metasurfaces and hence to analyze the effects of disorder step by step. The Cartesian and radial two-point correlation function (TPCF) as well as the structure factor (SF) are applied as metrics to quantify the disorder and relate them with the observed scattering properties of disordered metasurfaces. Together with the CPDA simulations, this provides an understanding of which scattering features are dominated by structural effects or the radiation of individual nanostructures.

The CPDA model not only provides the possibility to simulate the scattering of almost arbitrarily designed plasmonic metasurfaces, but also enables to change experimental parameters such as the NA of the objective, input and output polarization, or incidence angle of light. The latter makes the CPDA particularly suitable for computation of the highly

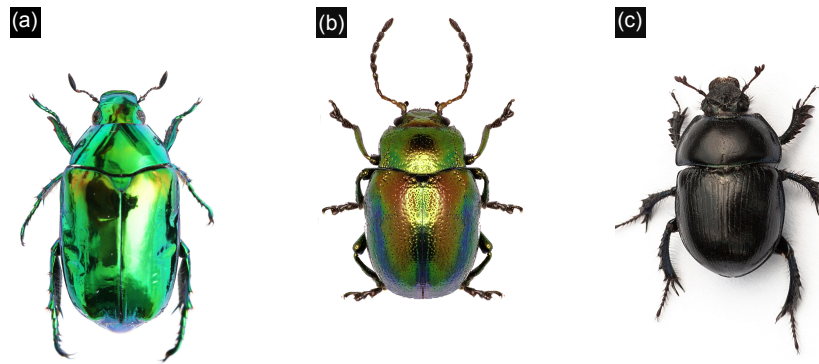


Fig. 1. Naturally occurring examples of surface dependent reflection. The bidirectional reflectance distribution function (BRDF) determines whether we recognize the beetles as being shiny [(a), (b) specular reflection] or matte [(c) angle-independent reflection]. Tailoring the disorder of metasurfaces can shape the BRDF to obtain the desired surface appearance and color.

multidimensional bidirectional reflectance distribution function (BRDF) [44]. The BRDF specifies the angular scattering of surfaces for different incidence angles, but can be extended to comprise polarization and wavelength dependence. It is regularly deployed for computer graphics or computer vision and allows one to deduce the appearance of surfaces with a dedicated color model. Vynck *et al.* demonstrated that it is possible to tailor the BRDF via disorder in metasurfaces. For reconstruction of the visible appearance [16,17], a modified sRGB color model can be used to compute the spatially and angle resolved appearance from the simulated hyperspectral data. This establishes the CPDA as a highly effective tool for the wavelength and polarization dependent BRDF computation of almost arbitrary plasmonic metasurfaces.

When looking at natural surfaces, such as those from beetles, one can see huge differences in color as well as in structural appearance. Some surfaces appear shiny with a metallic luster [see Figs. 1(a) and 1(b)], whereas others look matte [see Fig. 1(c)]. Especially, the beetles in Figs. 1(a) and 1(b) indicate that structures on the surface are extremely important for the BRDF, as they influence strongly the angle dependent reflectivity. In contrast to the beetle in (a) characterized by specular reflection, the beetle in (c) is rather dark and matte. From this simple example, one notices that tailoring the BRDF is crucial, and we ask ourselves the question whether a disordered metasurface with specific metasurface unit cells with a given three-dimensional differential scattering cross section when arranged in the appropriate fashion can tailor any desired appearance, as one would expect from rendering and ray tracing programs. Figure 2 illustrates the key question of our ansatz: can one tailor the correlation function (CF) and form factor (emission cone) of a metasurface such that any desired BRDF can be obtained?

The tutorial is organized as follows: in Section 2, we introduce the basic theory related to the CPDA, the reconstruction of near and far fields via the reciprocity theorem, and disorder metrics. Furthermore, we recapitulate how to image the FOURIER and image planes, and we discuss concepts for lensless imaging via FOURIER transform of the far-field image and phase-retrieval algorithms. Finally, we give some introduction to color science, which is necessary for constructing the visible appearance of

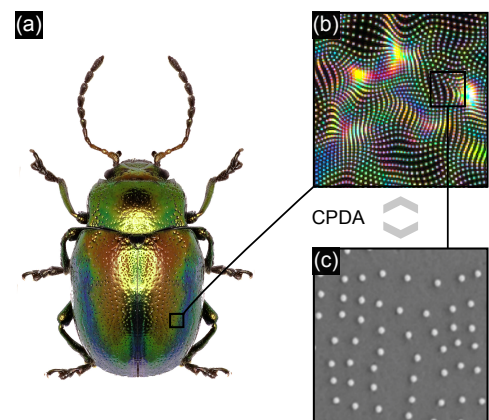


Fig. 2. Concept describing the key question. (c) How can one tailor the correlation function and form factor of metasurfaces, using the individual unit cells, to obtain any desired BRDF and appearance (color, i.e., spectral reflectance amplitude, angular and polarization distribution of reflectance), as (a), (b) in the shell of beetles? The key question we study with our CPDA is what role the type and the correlation of the disorder plays for the appearance of surfaces. The images in (b) and (c) are for illustration only and do not represent the actual beetle shell.

metasurfaces. In Section 3, we explain how our PYTHON software package is organized. Then, we provide simulation results for the reflection of ordered and disordered metasurfaces at normal and oblique incidences in Section 4. This includes a demonstration of beam switching [45] and tailored angular scattering via the phase-retrieval algorithms described in Section 2 by our software package. Finally, we validate our model by comparison with analytical results and full-wave simulations as well as experimental results. The tutorial concludes with a summary and outlook.

2. THEORETICAL BACKGROUND

This section provides the theoretical framework behind the computational approach presented in this tutorial. All important concepts necessary to understand the content of this tutorial are summarized in three sections. In the first section, the electromagnetic interaction model describing the properties of

plasmonic metasurfaces is derived. The second section introduces different types of structural disorder and provides metrics that characterize disorder. Finally, the color science behind the transition from spectral intensities to perceived colors is explained and discussed.

A. Dipolar Approximation of Plasmonic Metasurfaces

The key assumption of the introduced computational approach is that the nanostructures that constitute any plasmonic metasurface can be approximated as an ensemble of point dipoles. To understand the implications of this approximation, it is crucial to derive the most important laws starting from the fundamental MAXWELL equations. This way, one can keep track of all approximations introduced and get a feeling for the strengths and limits of this approach.

The frequency domain representation of MAXWELL equations is given in SI units as

$$\nabla \cdot \mathbf{D}(\mathbf{r}, \omega) = \varrho(\mathbf{r}, \omega), \quad (1a)$$

$$\nabla \cdot \mathbf{B}(\mathbf{r}, \omega) = 0, \quad (1b)$$

$$\nabla \times \mathbf{E}(\mathbf{r}, \omega) - i\omega\mathbf{B}(\mathbf{r}, \omega) = 0, \quad (1c)$$

$$\nabla \times \mathbf{H}(\mathbf{r}, \omega) + i\omega\mathbf{D}(\mathbf{r}, \omega) = \mathbf{j}(\mathbf{r}, \omega). \quad (1d)$$

Here, ϱ and \mathbf{j} indicate the free charge and current densities. Furthermore, the electric displacement \mathbf{D} and magnetic induction \mathbf{B} are linked to the electric and magnetic fields \mathbf{E} and \mathbf{H} , respectively, via

$$\mathbf{D} = \varepsilon_0 \hat{\varepsilon} \mathbf{E}, \quad (2)$$

$$\mathbf{B} = \mu_0 \hat{\mu} \mathbf{H}, \quad (3)$$

where $\hat{\varepsilon}$ and $\hat{\mu}$ denote the permittivity and permeability tensors, respectively, and $c_0^2 = 1/\varepsilon_0\mu_0$. For the sake of simplicity, we assume henceforth scalar permittivity and permeability values and omit the hat on top.

Assuming a spatially constant permeability μ , the wave equation can be derived using MAXWELL Eqs. (1c) and (1d) and Eqs. (2) and (3):

$$(-k_0^2 \varepsilon + \nabla \times \nabla \times) \mathbf{E}(\mathbf{r}, \omega) = i\omega\mu_0\mu\mathbf{j}(\mathbf{r}, \omega). \quad (4)$$

The wave equation describes an electromagnetic wave generated by a source \mathbf{j} that propagates in a medium with relative permittivity ε and permeability μ . Henceforth, we restrict us to spatially constant ε , so that we can assign the medium wavenumber $k = \sqrt{\varepsilon\mu}k_0$, where $k_0 = \omega/c_0$ is the vacuum wavenumber.

The scalar solution of the wave equation can be found in the absence of free charges ($\nabla \cdot \mathbf{D} = 0$) by computing the GREEN's function, which is the solution for an excitation by a point source,

$$(k^2 + \Delta) G(\mathbf{r}, \omega) = -\delta(\mathbf{r}), \quad (5)$$

and equals a spherical wave [46]:

$$G(\mathbf{r}, \omega) = \frac{e^{ikr}}{4\pi r}. \quad (6)$$

By using the GREEN's dyadic we can also find the solution for the multidimensional wave equation driven by a point source:

$$(k^2 + \nabla \times \nabla \times) \hat{G}(\mathbf{r}, \omega) = \hat{1}\delta(\mathbf{r}). \quad (7)$$

It can be shown that the GREEN's dyadic can be expressed in terms of the GREEN's function [46]

$$\begin{aligned} \hat{G}(\mathbf{r}, \omega) &= \left(\hat{1} + \frac{\nabla \otimes \nabla}{k^2} \right) G(\mathbf{r}, \omega) \\ &= \hat{G}_{\text{near}}(\mathbf{r}, \omega) + \hat{G}_{\text{inter}}(\mathbf{r}, \omega) + \hat{G}_{\text{far}}(\mathbf{r}, \omega). \end{aligned} \quad (8)$$

Here, \otimes denotes the outer vector product. As indicated in the second line of the equation above, the GREEN's dyadic can be separated into contributions that dominate in different spatial regimes:

$$\hat{G}_{\text{near}}(\mathbf{r}, \omega) = \frac{1}{(kr)^2} \left(-\hat{1} + 3\frac{\mathbf{r} \otimes \mathbf{r}}{r^2} \right) \frac{e^{ikr}}{4\pi r}, \quad (9a)$$

$$\hat{G}_{\text{inter}}(\mathbf{r}, \omega) = \frac{i}{kr} \left(\hat{1} - 3\frac{\mathbf{r} \otimes \mathbf{r}}{r^2} \right) \frac{e^{ikr}}{4\pi r}, \quad (9b)$$

$$\hat{G}_{\text{far}}(\mathbf{r}, \omega) = \left(\hat{1} - \frac{\mathbf{r} \otimes \mathbf{r}}{r^2} \right) \frac{e^{ikr}}{4\pi r}. \quad (9c)$$

Although there is obviously no discrete transition between the different regimes, these contributions are commonly referred to as near field, intermediate field, and far field. The names originate from the fact that the fields dominate in different distances to the point source, depending on the ratio $1/kr$.

Knowing the GREEN's dyadic, we can now find the particular solution of the wave equation in Eq. (4) by convoluting the GREEN's dyadic with the driving source:

$$\begin{aligned} \mathbf{E}(\mathbf{r}, \omega) &= \hat{G}(\mathbf{r}, \omega) * (i\omega\mu_0\mu\mathbf{j}(\mathbf{r}, \omega)) \\ &= \int \hat{G}(\mathbf{r} - \mathbf{r}', \omega) i\omega\mu_0\mu\mathbf{j}(\mathbf{r}', \omega) dV' \\ &\approx_{r \gg r'} \hat{G}(\mathbf{r}, \omega) i\omega\mu_0\mu \int \mathbf{j}(\mathbf{r}', \omega) dV'. \end{aligned} \quad (10)$$

The last step in the derivation above involves the assumption that $\hat{G}(\mathbf{r} - \mathbf{r}', \omega)$ is independent of \mathbf{r}' for distances \mathbf{r} much larger than \mathbf{r}' , and consequently, the integral can be evaluated independently. The remaining integral can be solved by expressing the current density in terms of the dipole moment via [46]

$$\frac{i}{\omega} \int \mathbf{j}(\mathbf{r}, \omega) dV = \mathbf{p}(\omega) = \int \varrho(\mathbf{r}, \omega) \mathbf{r} dV. \quad (11)$$

After inserting this expression into Eq. (10), we find that the electric field radiated by a point source $\mathbf{j}(\mathbf{r}, \omega) = \mathbf{J}(\omega)\delta(\mathbf{r})$ is given by

$$\mathbf{E}(\mathbf{r}, \omega) \approx \hat{G}(\mathbf{r}, \omega) \omega^2 \mu_0 \mu \mathbf{p}(\omega). \quad (12)$$

By replacing the angular frequency ω with the wavenumber k , we can define the electric field radiated by a point dipole in terms of the wavenumber:

$$\mathbf{E}_d(\mathbf{r}, k) = \frac{k^2}{\varepsilon_0 \varepsilon} \hat{G}(\mathbf{r}, k) \mathbf{p}(k). \quad (13)$$

1. Dipolar Coupling Model

So far, we have considered only the situation of a single dipole. For a higher number of dipoles, coupling effects start to play a role and thus need to be considered in the dipole model. To describe these coupling processes mathematically, we need to recapitulate that the polarizability tensor $\hat{\alpha}$ is a dipole dependent property that provides the induced dipole moment \mathbf{p} for a given electric field \mathbf{E}_{tot} at the position of that dipole. In the following derivations, the index $m = 1, 2, \dots, N$ labels each dipole situated at position \mathbf{r}_m and characterized by the polarizability tensor $\hat{\alpha}_m$. This means that we can express each dipole moment induced by the total electric field \mathbf{E}_{tot} as

$$\mathbf{p}_m(k) = \varepsilon_0 \varepsilon \hat{\alpha}_m(k) \mathbf{E}_{\text{tot}}(\mathbf{r}_m, k). \quad (14)$$

Here, the total electric field consists of contributions from an external incident electric field $\mathbf{E}_{\text{inc}}(\mathbf{r}_m, k)$ and fields radiated by all other $N - 1$ dipoles $\mathbf{E}_{d,n}(\mathbf{r}_m, k)$. Hence, the total electric field at position \mathbf{r}_m is

$$\begin{aligned} \mathbf{E}_{\text{tot}}(\mathbf{r}_m, k) &= \mathbf{E}_{\text{inc}}(\mathbf{r}_m, k) + \sum_{n \neq m}^N \mathbf{E}_{d,n}(\mathbf{r}_m, k) \\ &\stackrel{\text{Eq. (13)}}{=} \mathbf{E}_{\text{inc}}(\mathbf{r}_m, k) + \frac{k^2}{\varepsilon_0 \varepsilon} \sum_{n \neq m}^N \hat{G}(\mathbf{r}_m - \mathbf{r}_n, k) \mathbf{p}_n(k). \end{aligned} \quad (15)$$

By inserting this expression into Eq. (14), one obtains an expression for the m th dipole moment in dependence of the incident electric field and all other dipole moments $\mathbf{p}_n(k)$:

$$\mathbf{p}_m(k) = \hat{\alpha}_m(k) (\varepsilon_0 \varepsilon \mathbf{E}_{\text{inc}}(\mathbf{r}_m, k) + k^2 \sum_{n \neq m}^N \hat{G}(\mathbf{r}_m - \mathbf{r}_n, k) \mathbf{p}_n(k)). \quad (16)$$

This set of coupled equations describes the coupling of the dipole ensemble, given an incident electric field \mathbf{E}_{inc} . By rearranging the equation, we can express our equation system as the matrix equation

$$\begin{aligned} &\underbrace{\begin{pmatrix} \hat{\alpha}_1(k)^{-1} & \cdots & -k^2 \hat{G}(\mathbf{r}_1 - \mathbf{r}_N, k) \\ \vdots & \ddots & \vdots \\ -k^2 \hat{G}(\mathbf{r}_N - \mathbf{r}_1, k) & \cdots & \hat{\alpha}_N(k)^{-1} \end{pmatrix}}_{\hat{T}_M} \underbrace{\begin{pmatrix} \mathbf{p}_1(k) \\ \vdots \\ \mathbf{p}_N(k) \end{pmatrix}}_{\mathcal{P}_M} \\ &= \varepsilon \varepsilon_0 \underbrace{\begin{pmatrix} \mathbf{E}_{\text{inc}}(\mathbf{r}_1, k) \\ \vdots \\ \mathbf{E}_{\text{inc}}(\mathbf{r}_N, k) \end{pmatrix}}_{\mathcal{E}_M}, \end{aligned} \quad (17)$$

where we define \hat{T}_M as the transfer matrix, \mathcal{P}_M as the dipole moment vector, and \mathcal{E}_M as the incident electric field vector.

Obviously, the main diagonal of the transfer matrix contains only the dipole polarizabilities without any information about the coupling processes. All the coupling information is fully provided by the non-diagonal elements of \hat{T}_M , which solely depend on the wavenumber of the radiated light and the GREEN'S dyadic. Inverting the transfer matrix solves Eq. (17) for the dipole moment vector and yields

$$\mathcal{P}_M = \hat{T}_M^{-1} \mathcal{E}_M. \quad (18)$$

At this point, it may not be entirely obvious why it is necessary to calculate the dipole moments to ultimately predict the far-field response of the dipole ensemble. However, the dipole moments are required for applying the reciprocity theorem, which is discussed in the following section.

2. Reciprocity Theorem

The reciprocity theorem forms the basis for various computational approaches in electromagnetics [41,47–50] and is also essential for the CPDA model presented in this study. Although the starting point of the mathematical derivation of the reciprocity theorem might seem less intuitive, it eventually returns the physical laws required for the CPDA model. More specifically, we follow here the idea of the near-to-far-field transformation [48,50] that is illustrated in Fig. 3 to derive the field emitted by an array of dipoles. Thus, let us consider two sources \mathbf{j}_1 and \mathbf{j}_2 that generate electromagnetic fields \mathbf{E}_1 and \mathbf{E}_2 . By applying the divergence operator and cross product on these fields, we get

$$\begin{aligned} &\nabla \cdot (\mathbf{E}_1 \times \mathbf{H}_2 - \mathbf{E}_2 \times \mathbf{H}_1) \\ &= (\nabla \times \mathbf{E}_1) \cdot \mathbf{H}_2 - (\nabla \times \mathbf{H}_2) \cdot \mathbf{E}_1 \\ &\quad - (\nabla \times \mathbf{E}_2) \cdot \mathbf{H}_1 + (\nabla \times \mathbf{H}_1) \cdot \mathbf{E}_2. \end{aligned} \quad (19)$$

The curl of the electric and magnetic fields can be replaced by using MAXWELL equations Eqs. (1c) and (1d):

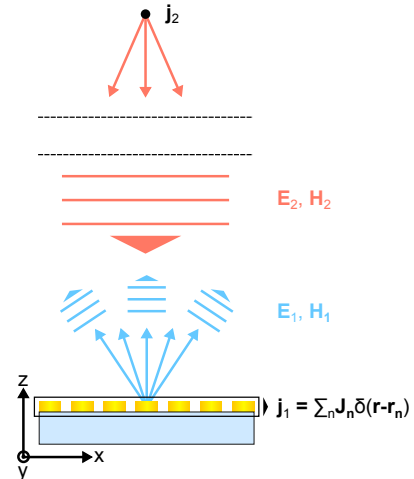


Fig. 3. Explanation of the reciprocity theorem. Within this work, the reciprocity theorem is applied for an illuminating source \mathbf{j}_2 located at infinite distance to the sources \mathbf{j}_1 that constitute the metasurface. The substrate beneath the sources \mathbf{j}_1 is only for illustration and is not considered for the approach presented in this tutorial.

$$\begin{aligned} & \underset{\text{Eq. (19)}}{=} i\omega \mathbf{B}_1 \cdot \mathbf{H}_2 - (\mathbf{j}_2 - i\omega \mathbf{D}_2) \cdot \mathbf{E}_1 \\ & - i\omega \mathbf{B}_2 \cdot \mathbf{H}_1 + (\mathbf{j}_1 - i\omega \mathbf{D}_1) \cdot \mathbf{E}_2, \end{aligned} \quad (20)$$

and subsequently, material equations Eqs. (2) and (3):

$$\begin{aligned} & \underset{\text{Eq. (20)}}{=} i\omega \mu_0 \mu \mathbf{H}_1 \cdot \mathbf{H}_2 - (\mathbf{j}_2 - i\omega \varepsilon_0 \varepsilon \mathbf{E}_2) \cdot \mathbf{E}_1 \\ & - i\omega \mu_0 \mu \mathbf{H}_2 \cdot \mathbf{H}_1 + (\mathbf{j}_1 - i\omega \varepsilon_0 \varepsilon \mathbf{E}_1) \cdot \mathbf{E}_2, \end{aligned} \quad (21)$$

which can be further simplified for reciprocal materials ($\hat{\varepsilon} = \hat{\varepsilon}^T$, $\hat{\mu} = \hat{\mu}^T$):

$$\underset{\text{Eq. (21)}}{=} \mathbf{j}_1 \cdot \mathbf{E}_2 - \mathbf{j}_2 \cdot \mathbf{E}_1. \quad (22)$$

In summary, this means that we can write

$$\nabla \cdot (\mathbf{E}_1 \times \mathbf{H}_2 - \mathbf{E}_2 \times \mathbf{H}_1) = \mathbf{j}_1 \cdot \mathbf{E}_2 - \mathbf{j}_2 \cdot \mathbf{E}_1, \quad (23)$$

which is the differential form of the reciprocity theorem. The integral form is obtained by integrating over a finite volume V and applying the divergence theorem to the left-hand side:

$$\oint (\mathbf{E}_1 \times \mathbf{H}_2 - \mathbf{E}_2 \times \mathbf{H}_1) \cdot d\mathbf{S} = \int (\mathbf{j}_1 \cdot \mathbf{E}_2 - \mathbf{j}_2 \cdot \mathbf{E}_1) dV. \quad (24)$$

We have defined the surface element $d\mathbf{S} = \mathbf{n}dS$ with the surface normal vector \mathbf{n} at the boundary of the volume V . One should keep in mind that the reciprocity theorem holds true only for reciprocal materials ($\hat{\varepsilon} = \hat{\varepsilon}^T$, $\hat{\mu} = \hat{\mu}^T$), which is the case for the materials considered in this tutorial. At this point, it is important to introduce some assumptions about our physical system to simplify the reciprocity theorem and ultimately obtain an analytical expression for the far-field response of our dipole ensemble. We define that the dipole ensemble is summarized as source \mathbf{j}_1 and the light source that excites the dipole ensemble corresponds to source \mathbf{j}_2 . We further assume that the light source is far outside the integration volume, which means that the volume integral for source \mathbf{j}_2 must equal zero in the considered volume, so that

$$\oint (\mathbf{E}_1 \times \mathbf{H}_2 - \mathbf{E}_2 \times \mathbf{H}_1) \cdot d\mathbf{S} = \int \mathbf{j}_1 \cdot \mathbf{E}_2 dV. \quad (25)$$

If we consider a set of localized point sources as

$$\mathbf{j}_1(\mathbf{r}) = \sum_n \mathbf{J}_n \delta(\mathbf{r} - \mathbf{r}_n), \quad (26)$$

the integral on the right-hand side can be solved by using Eq. (11):

$$\oint (\mathbf{E}_1 \times \mathbf{H}_2 - \mathbf{E}_2 \times \mathbf{H}_1) \cdot d\mathbf{S} = -i\omega \sum_n \mathbf{p}_n \cdot \mathbf{E}_2(\mathbf{r}_n). \quad (27)$$

At this point, one can already guess that the dipole moments derived in Eq. (17) are required to calculate fields \mathbf{E}_1 and \mathbf{H}_1 generated by the dipole ensemble. Nevertheless, we need to define our electromagnetic fields appropriately to solve the remaining surface integral. While we want to determine \mathbf{E}_1 and \mathbf{H}_1 , we can select suitable fields \mathbf{E}_2 and \mathbf{H}_2 to simplify this task.

Therefore, we define them to be plane waves with the mutually orthogonal transverse electric (TE) and transverse magnetic (TM) polarization vectors:

$$\mathbf{E}_{\text{TE}}^{\pm}(\mathbf{k}_{\parallel}) = \frac{1}{k_{\parallel}} \begin{pmatrix} -k_y \\ k_x \\ 0 \end{pmatrix}, \quad (28a)$$

$$\mathbf{E}_{\text{TM}}^{\pm}(\mathbf{k}_{\parallel}) = \frac{1}{kk_{\parallel}} \begin{pmatrix} k_x k_z \\ k_y k_z \\ \mp k_{\parallel}^2 \end{pmatrix}, \quad (28b)$$

$$\mathbf{H}_{\text{TE}}^{\pm}(\mathbf{k}_{\parallel}) = \frac{1}{Zkk_{\parallel}} \begin{pmatrix} \mp k_x k_z \\ \mp k_y k_z \\ k_{\parallel}^2 \end{pmatrix}, \quad (28c)$$

$$\mathbf{H}_{\text{TM}}^{\pm}(\mathbf{k}_{\parallel}) = \frac{\pm 1}{Zk_{\parallel}} \begin{pmatrix} -k_y \\ k_x \\ 0 \end{pmatrix}, \quad (28d)$$

Here, $Z = \sqrt{\mu/\varepsilon}$ is the wave impedance, \mathbf{k}_{\parallel} is the projection of the wave vector to the xy plane, i.e., it consists of wave vector components k_x and k_y , and $k_{\parallel} = \sqrt{k_x^2 + k_y^2}$ is the corresponding length. Component k_z is linked to the wavenumber via

$$k_z = \sqrt{k^2 - k_{\parallel}^2}. \quad (29)$$

Note that there is an ambiguity in selecting the sign of the square root. Here, we define k_z to correspond to an outgoing plane wave [50]. Hence, the + and - signs in Eqs. (28a) to (28d) denote outgoing and incoming plane waves, respectively.

Since plane waves form a set of orthogonal basis functions and \mathbf{E}_1 and \mathbf{H}_1 are purely outgoing outside the dipole array, we may define them as a superposition of plane waves:

$$\mathbf{E}_1 = \int [\alpha_{\text{TE}}^+(\mathbf{k}_{\parallel}) \mathbf{E}_{\text{TE}}^+(\mathbf{k}_{\parallel}) + \alpha_{\text{TM}}^+(\mathbf{k}_{\parallel}) \mathbf{E}_{\text{TM}}^+(\mathbf{k}_{\parallel})] e^{i\mathbf{k}\cdot\mathbf{r}} d^2\mathbf{k}_{\parallel}, \quad (30a)$$

$$\mathbf{H}_1 = \int [\alpha_{\text{TE}}^+(\mathbf{k}_{\parallel}) \mathbf{H}_{\text{TE}}^+(\mathbf{k}_{\parallel}) + \alpha_{\text{TM}}^+(\mathbf{k}_{\parallel}) \mathbf{H}_{\text{TM}}^+(\mathbf{k}_{\parallel})] e^{i\mathbf{k}\cdot\mathbf{r}} d^2\mathbf{k}_{\parallel}. \quad (30b)$$

To find field amplitudes α_{TE}^+ and α_{TM}^+ , we need to evaluate the integral on the left-hand side of Eq. (27). We consider planar surfaces parallel to the xy plane on the top and bottom and an infinite extension to the left and right. Let us consider an incident plane wave \mathbf{H}_2 from the top with an in-plane component $-\mathbf{k}'_{\parallel}$. We then integrate the planar surfaces at the top (incident polarization is \mathbf{H}^-) and bottom (incident polarization is \mathbf{H}^+) separately for the first term,

$$\begin{aligned} & \int [\mathbf{E}_1 \times \mathbf{H}_2(-\mathbf{k}'_{\parallel})] \cdot \mathbf{n} dx dy \\ & = \pm \int \left[\int \alpha_X^+(\mathbf{k}_{\parallel}) \mathbf{E}_X^+(\mathbf{k}_{\parallel}) \times \mathbf{H}_Y^{\mp}(-\mathbf{k}'_{\parallel}) e^{i(k-k')\cdot\mathbf{r}} d^2\mathbf{k}_{\parallel} \right]_z dx dy \\ & = \pm (2\pi)^2 \alpha_Y^{\pm}(\mathbf{k}'_{\parallel}) [\mathbf{E}_Y^{\pm}(\mathbf{k}'_{\parallel}) \times \mathbf{H}_Y^{\mp}(-\mathbf{k}'_{\parallel})]_z e^{\pm i(k'_z \pm k'_z)z}, \end{aligned} \quad (31)$$

and second term,

$$\begin{aligned} & \int [\mathbf{E}_2(-\mathbf{k}'_{\parallel}) \times \mathbf{H}_1] \cdot \mathbf{n} dx dy \\ &= \pm \int \left[\int \alpha_X^+(\mathbf{k}_{\parallel}) \mathbf{E}_X^{\mp}(-\mathbf{k}'_{\parallel}) \times \mathbf{H}_Y^+(\mathbf{k}_{\parallel}) e^{i(\mathbf{k}-\mathbf{k}') \cdot \mathbf{r}} d^2 \mathbf{k}_{\parallel} \right]_z dx dy \\ &= \pm (2\pi)^2 \alpha_Y^+(\mathbf{k}'_{\parallel}) [\mathbf{E}_Y^{\mp}(-\mathbf{k}'_{\parallel}) \times \mathbf{H}_Y^+(\mathbf{k}'_{\parallel})]_z e^{\pm i(k'_z \pm k'_z)z}, \end{aligned} \quad (32)$$

where X and Y indicate TE and TM polarizations, respectively, and we have used the orthogonality of plane waves and polarization states. Because of this, only the following expressions have to be evaluated [50]:

$$[\mathbf{E}_X^e \times \mathbf{H}_X^h]_z = \frac{h k_z}{Z k}, \quad (33)$$

where $e = \pm 1$ and $h = \pm 1$ indicate incoming or outgoing fields. The result is solely determined by the sign of the magnetic field. Consequently, the difference between Eq. (31) and Eq. (32) equals zero at the bottom surface. Thus, we arrive at

$$\alpha_{\text{TE}}^+(\mathbf{k}_{\parallel}) = \frac{i k^2}{2\epsilon_0 \epsilon S k_z} \sum_n \mathbf{p}_n \cdot \mathbf{E}_{\text{TE}}^-(\mathbf{k}_{\parallel}) e^{-i\mathbf{k}_{\parallel} \cdot \mathbf{r}_n + i k_z(z-z_n)}, \quad (34a)$$

$$\alpha_{\text{TM}}^+(\mathbf{k}_{\parallel}) = \frac{i k^2}{2\epsilon_0 \epsilon S k_z} \sum_n \mathbf{p}_n \cdot \mathbf{E}_{\text{TM}}^-(\mathbf{k}_{\parallel}) e^{-i\mathbf{k}_{\parallel} \cdot \mathbf{r}_n + i k_z(z-z_n)}. \quad (34b)$$

Here, S comes from the orthonormality of plane waves and equals $(2\pi)^2$ for the infinitely extended surfaces. In numerical calculations, however, we truncate our computational space and assume periodic boundary conditions, so that S equals the area of the surface.

This means that the complex field amplitudes depend on all dipole moments \mathbf{p}_n and the incident electric field \mathbf{E}_2 , which can be any arbitrary plane wave. Since the dipole moments \mathbf{p}_n can be computed by solving the set of equations defined in Eq. (17), we can now calculate the FOURIER transform of electric field \mathbf{E}_1 , radiated into the far-field by the ensemble of point dipoles.

B. Disorder in Plasmonic Metasurfaces

With the dipole model discussed in Section 2.A, it is possible to compute the reflectance and transmittance of any arrangement of dipoles. However, to quantify the effects of disorder on plasmonic metasurfaces, it is important to introduce a disorder model that allows one to generate unbiased, randomized but still reproducible structure distributions. It is important to mention that there are many different ways to implement such a disorder model. Here, we introduce the disorder by perturbing a periodic grid of plasmonic structures. This way, it is possible to unambiguously define the non-disordered case and gradually increase the influence of the different disorder types. Figure 4 explains how positional disorder is introduced for a symmetric 3×3 grid of disks with periodicities p_x and p_y . From now on, we refer to the number of structures as n_x

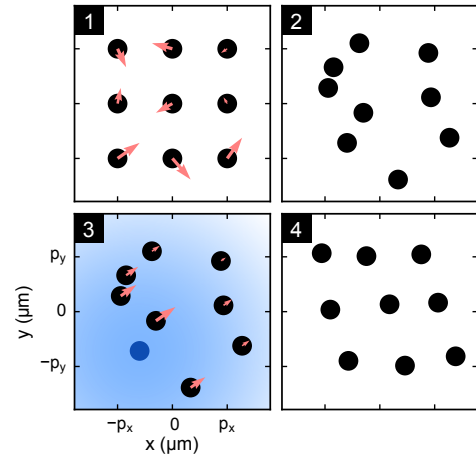


Fig. 4. Introduction of disorder and correlation. The four steps shown in this figure explain how positional disorder is introduced. The situation is similar for rotational and dimensional disorder. (1) Initially, all structures are arranged as a periodic grid with periodicities p_x or p_y and number of structures n_x or n_y in x or y direction, respectively. Random shift vectors (red arrows) are assigned to each structure. (2) Each structure is shifted into the randomly assigned direction. For uncorrelated disorder, the process ends here. (3) Correlation is introduced by iterating through all structures and shifting the residual structures into the same direction with the shift distance being dependent on the spatial distance to the current structure. The blue disk relates to the structure of the current iteration step, and the fading blue area represents the normal distribution that weights the shift distances. (4) Final correlated structure after repeating the iteration step in (3) for each structure.

and n_y and to the periodicities as p_x and p_y , where x and y specify the corresponding spatial directions. The periodic grid is perturbed by assigning random shifts to each of the structures. These random shifts are determined by a probability density function (PDF) $P(\delta\mathbf{r}|s_d\mathbf{p})$, which defines the probability that a structure experiences a shift $\delta\mathbf{r} = (\delta x, \delta y)^T$ in dependence of the periodicities $\mathbf{p} = (p_x, p_y)^T$ and the disorder strength $s_d \in \mathbb{R}_{\geq 0}$. For convenience, the PDF is abbreviated henceforth as $P(\delta\mathbf{r})$.

We distinguish two types of disorder: correlated and uncorrelated. For the latter, the perturbation process finishes after shifting each structure in the random direction $\delta\mathbf{r}$. To establish a correlation between individual structure perturbations, further steps are required. First, a CF $C(\Delta\mathbf{r}, l_c\mathbf{p}) \equiv C(\Delta\mathbf{r})$ with the corresponding correlation length $l_c \in \mathbb{R}_{\geq 0}$ needs to be introduced. This function correlates the perturbations that act on a structure at position \mathbf{r}_i with the perturbations acting on a structure at position $\mathbf{r}_j = \mathbf{r}_i + \Delta\mathbf{r}$. The correlation is introduced by selecting one structure s_i and shifting all other structures $s_j (i \neq j)$ in the same direction until each structure $i = 1, \dots, N (N = n_x \cdot n_y)$ is selected. Depending on the CF $C(\Delta\mathbf{r})$ and the correlation length l_c , the lengths of the shift vectors are weighted differently, while the shift directions stay unaffected by the correlation process.

Thus far, uncorrelated and correlated positional disorder were explained qualitatively. However, the PDF and CF have not been specified at this point. It is important to mention that the PDF needs to be normalized by definition, which is not

the case for CF. Besides that, there are only a few restrictions in choosing distributions for $P(\delta\mathbf{r})$ and $C(\Delta\mathbf{r})$, especially since many PDFs can be generated by applying inverse transform sampling. Within this tutorial, the uniform, normal, and triangular distributions are chosen as available distributions. The corresponding multidimensional expressions are

$$P_u(\delta\mathbf{r}) = \begin{cases} \frac{1}{N_0}, & |\delta\mathbf{r}^T \Sigma_d^{-1} \delta\mathbf{r}| \leq 1/2 \\ 0, & \text{else,} \end{cases} \quad (35a)$$

$$P_n(\delta\mathbf{r}) = \frac{1}{N_0} \exp(-4 \ln 2 \cdot \delta\mathbf{r}^T \Sigma_d^{-1} \delta\mathbf{r}), \quad (35b)$$

$$P_t(\delta\mathbf{r}) = \begin{cases} \frac{1}{N_0} (1 - |\delta\mathbf{r}^T \Sigma_d^{-1} \delta\mathbf{r}|), & |\delta\mathbf{r}^T \Sigma_d^{-1} \delta\mathbf{r}| \leq 1 \\ 0, & \text{else} \end{cases} \quad (35c)$$

for the PDFs and

$$C_u(\Delta\mathbf{r}) = \begin{cases} 1, & |\Delta\mathbf{r}^T \Sigma_c^{-1} \Delta\mathbf{r}| \leq 1/2 \\ 0, & \text{else,} \end{cases} \quad (36a)$$

$$C_n(\Delta\mathbf{r}) = \exp(-4 \ln 2 \cdot \Delta\mathbf{r}^T \Sigma_c^{-1} \Delta\mathbf{r}), \quad (36b)$$

$$C_t(\Delta\mathbf{r}) = \begin{cases} 1 - |\Delta\mathbf{r}^T \Sigma_c^{-1} \Delta\mathbf{r}|, & |\Delta\mathbf{r}^T \Sigma_c^{-1} \Delta\mathbf{r}| \leq 1 \\ 0, & \text{else} \end{cases} \quad (36c)$$

for the CFs. The subscripts u, n, and t correspond to uniform, normal, and triangular distributions, respectively, while N_0 is the required normalization constant of the PDF. In two dimensions, it is $\delta\mathbf{r} = (\delta x, \delta y)^T$, $\Delta\mathbf{r} = (\Delta x, \Delta y)^T$, and

$$\Sigma_d = \begin{pmatrix} (s_d \cdot p_x)^2 & 0 \\ 0 & (s_d \cdot p_y)^2 \end{pmatrix}, \quad (37a)$$

$$\Sigma_c = \begin{pmatrix} (l_c \cdot p_x)^2 & 0 \\ 0 & (l_c \cdot p_y)^2 \end{pmatrix}. \quad (37b)$$

All three distributions are scaled such that the disorder strength and correlation length are proportional to the FWHM of the distributions, so that it is

$$\text{FWHM}_x = s_d \cdot p_x, \quad (38a)$$

$$\text{FWHM}_y = s_d \cdot p_y, \quad (38b)$$

and

$$\text{FWHM}_x = l_c \cdot p_x, \quad (39a)$$

$$\text{FWHM}_y = l_c \cdot p_y, \quad (39b)$$

respectively. Since the FWHM is ambiguous for uniform distribution, we define it as the width between both discontinuous steps. If not stated differently, the PDF is chosen to be uniformly distributed, whereas the CF is normally distributed. The latter is beneficial to establish a correlation over the entire ensemble, since normal distribution is the only distribution with support over the entire space.

Table 1. PDFs and CFs for Positional, Rotational, and Dimensional Disorder^a

	Positional	Rotational	Dimensional
PDF	$P^p(\delta\mathbf{r} s_d^p \mathbf{p})$	$P^r(\delta\phi 2\pi s_d^r)$	$P^d(\delta S s_d^d)$
CF	$C^p(\Delta\mathbf{r}, l_c^p \mathbf{p})$	$C^r(\Delta\mathbf{r}, l_c^r \mathbf{p})$	$C^d(\Delta\mathbf{r}, l_c^d \mathbf{p})$

^aSuperscripts p, r, and d refer to the positional, rotational, and dimensional disorder. All CFs weight the quantity $\delta\mathbf{r}$, $\delta\phi$, or δS that belongs to the corresponding disorder type.

1. Disorder Types

The previous section has given a general overview on the process of introducing disorder and correlation and also specified the underlying distributions. However, all explanations refer only to positional disorder, which affects the centroid positions of each structure. Also, rotational and dimensional disorder and any superposition of all three disorder types can be utilized to perturb the structures. All three types are shown in Fig. 5.

As the name indicates, rotational disorder affects the in-plane orientation of each structure. The disorder strength $s_d \in \mathbb{R}_{\geq 0}$ is now defined relative to a full rotation of 2π , which means that the PDF is now $P(\delta\phi|2\pi s_d)$. The CF is still dependent on the spatial separation $\Delta\mathbf{r}$ of two structures but affects the rotation angle $\delta\phi$ (mathematically positive rotation with $\delta\phi = 0$ being aligned along the x -axis) instead of the spatial shift $\delta\mathbf{r}$, as for positional disorder.

Similarly, dimensional disorder perturbs the size of a structure. As solely rod- and disk-shaped structures are considered within this study, we define the size as either the rod length or disk diameter, respectively. In this case, the PDF randomizes the relative size deviations δS of a structure in dependence of the disorder strength $s_d \in \mathbb{R}_{\geq 0}$, which yields $P(\delta S|s_d)$. For instance, changing a rod with length $S_{\text{pre}} = 200$ nm by $\delta S = -0.05$ yields a rod with length $S_{\text{post}} = (1 + \delta S) \cdot S_{\text{pre}} = 190$ nm. Again, the weights deduced from the CF depend only on the spatial separation $\Delta\mathbf{r}$ of two structures and the correlation length l_c , while now affecting the size deviations δS .

In Table 1, the dependencies of the PDFs and CFs for the three disorder types are shown. For each disorder style, separate disorder strengths, correlation lengths, and distributions can be chosen, which provides a large variety of possible disorder realizations. Since the random numbers utilized for the PDFs are generated computationally as pseudorandom numbers, it is possible to recreate a randomly disordered metasurface by specifying a so-called seed value for the pseudorandom number generator in use. Consequently, in this disorder formalism, a metasurface is fully characterized by specifying the periodicities (p_x, p_y) and number of structures (n_x, n_y) of the unperturbed grid as well as the disorder strengths, correlation lengths, PDFs, and CFs in addition to the random seeds.

2. Disorder Metrics

In the previous sections, we have introduced a disorder model that allows one to perturb any periodic arrangement of plasmonic structures. Thus, the question arises whether it is possible to find certain metrics that quantify the effects of disorder and

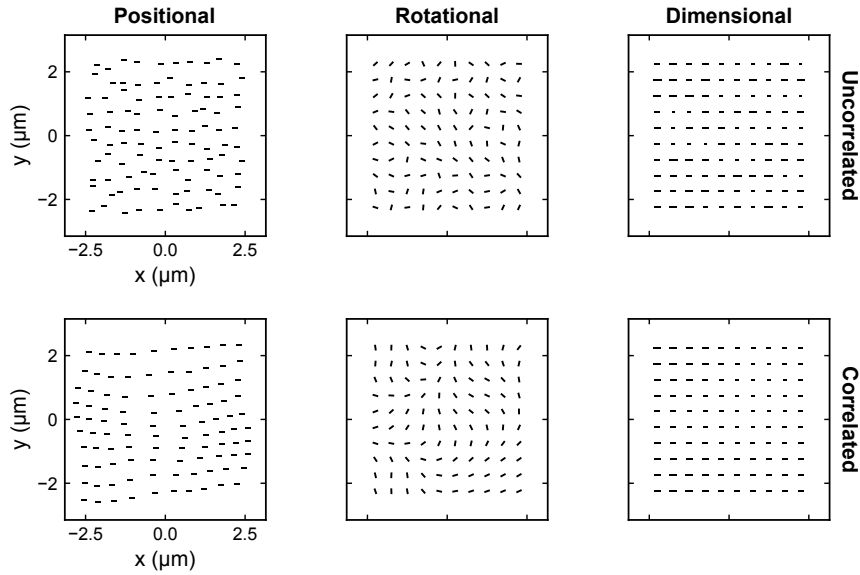


Fig. 5. Disorder types. The top panels display uncorrelated disorder, where each structure is perturbed independently of the neighboring structures. Three different geometrical perturbations of a perfect periodic array are considered here. Left: to obtain positional disorder, all structures are shifted into a random direction starting from a periodic arrangement. Middle: rotational disorder is introduced by rotating the structures around their centers. Right: dimensional disorder stretches or squeezes each structure relative to the initial structure size. In general, any superposition of these disorder types is possible. The correlated disorder in the bottom panels is different from uncorrelated disorder in respect to the dependency on the neighborhood of the introduced perturbations. More specifically, in all three cases of geometrical perturbations, the correlation depends on the spatial distance between the structures. Hence, either the random shift distances, random rotation angles, or relative size deviations are dependent on the neighboring structures.

correlation. At this point we investigate only the effects of positional disorder, so that the quantification of the remaining two disorder types is to be done in future work.

In this section, established metrics from astrophysics and crystallography are applied on structures generated using the disorder formalism introduced before. These metrics are the TPCF and SF and allow one to characterize metasurfaces in real and reciprocal spaces [51–53].

The TPCF is commonly used in astrophysics to characterize the non-uniformity of galaxies due to clustering. There exist various estimators that compensate for errors that originate from the spatially confined nature and finite number of structures in the investigated system [51]. A comparison of these estimators has shown that the LANDY–SZALAY estimator performs best in the context of astrophysics [52] and is therefore utilized to calculate the TPCFs of the disordered metasurfaces in this work. The idea behind the TPCF is to count the number of structure pairs within a certain distance interval. The LANDY–SZALAY estimator requires three different quantities, which are data–data pair counts DD , data–random pair counts DR , and random–random pair counts RR . DD pair counts are calculated by iterating through all the coordinates of the structure ensemble (source) and counting the number of other structures in the source that lie within a certain distance interval. To calculate DR and RR , it is necessary to artificially generate random coordinates used to define complete randomness. If not stated differently, the random dataset is generated by uniformly distributing coordinates in the same spatial range as the coordinates of the source. In most cases, the number of random coordinates is chosen to be 10–100× the number of source

coordinates to ensure a good level of uniformity. Similar to DD , RR is calculated by iterating through all coordinates of the artificial dataset and counting the number of other structures in this artificial dataset within a certain distance range. The computation of DR is slightly different, as it is calculated by iterating through the source, but the number of structures in the artificial dataset within a distance interval to the source structure is counted. After computing DD , DR , and RR , the LANDY–SZALAY estimator of the TPCF is given by

$$\xi = \frac{F^2 \cdot DD - F \cdot 2DR + RR}{RR}. \quad (40)$$

Here, $F = N_R/N_D$ is the fraction of total datapoints in the random and source dataset and is required to adequately normalize the estimator. As shown in Fig. 6, we further distinguish between the radial and Cartesian TPCFs, depending on whether radial distance intervals $[r' - \delta r', r' + \delta r']$ or Cartesian intervals $[x' - \delta x', x' + \delta x'] \cap [y' - \delta y', y' + \delta y']$ are used. Both radial and Cartesian TPCFs have advantages depending on the use case. One of the greatest advantages of the radial TPCF is its one-dimensionality. This provides an easily understandable measure independent of the dimensionality of the investigated system. However, especially for highly non-isotropic systems, the radial TPCF might be deceiving. In such cases, it is inevitable to use the Cartesian TPCF for characterization of the metasurface. Besides these differences, both TPCFs have in common that positive/negative values indicate positive/negative correlation, whereas values close to zero correspond to uncorrelated randomness. This makes the TPCF a powerful metric that vividly reveals spatial correlations.

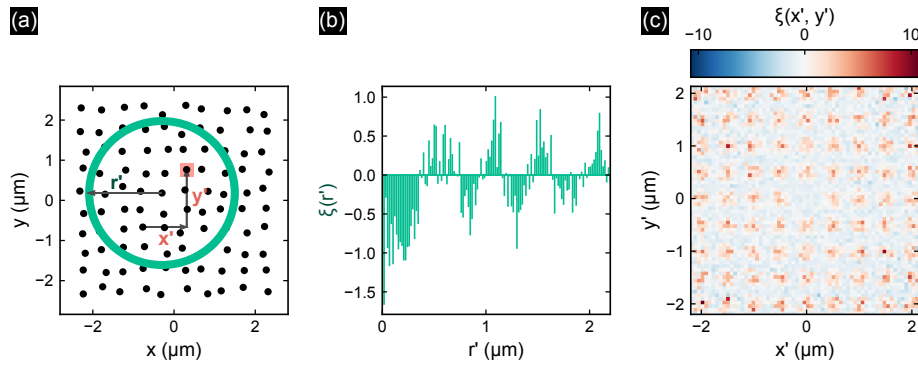


Fig. 6. Explanation of the radial and Cartesian TPCF. (a) Exemplary structure distribution. For the radial TPCF in (b) the data–data pair count DD is calculated by counting the number of structures in the interval $[r' - \delta r', r' + \delta r']$ (green area) for any structure in the source dataset and any distance r' . Similarly, the data–random pair count DR and random–random pair count RR can be computed, which enables to calculate the radial TPCF shown (b) using the LANDY–SZALAY estimator defined in Eq. (40). (c) In the case of the Cartesian TPCF, the numbers of structures in the interval $[x' - \delta x', x' + \delta x'] \cap [y' - \delta y', y' + \delta y']$ (red area) are counted. The exemplary structure distribution illustrates this for one structure in the source dataset. Repeating this for all structures in the source dataset and various distances x' and y' leads to DD , DR , and RR , which yields the computation of the TPCFs.

While the TPCF is suitable to unmask spatial characteristics, it is less convenient to unveil reciprocal properties and long-range characteristics. Therefore, we need to introduce the SF. The SF is a metric commonly used to interpret the diffraction patterns occurring in crystallography. As the name indicates, it describes the contribution to a diffraction pattern that originates from the distribution of structures. The most general form of the SF is given as

$$S(\mathbf{q}) = \frac{\sum_{n=1}^N \sum_{m=1}^N f_n f_m e^{-i\mathbf{q}(\mathbf{r}_n - \mathbf{r}_m)}}{\sum_{n=1}^N f_n^2}, \quad (41)$$

with the reciprocal coordinates $\mathbf{q} = (q_x, q_y)^T$, form factor of the n th particle f_n , position of the n th particle $\mathbf{r}_n = (x_n, y_n)^T$, and total number of particles N [53]. In this context, the form factor is proportional to the scattering amplitudes of a single structure [19]. Eq. (41) significantly simplifies if we consider only systems with equal scattering structures ($f = f_n$):

$$S(\mathbf{q}) = \frac{1}{N} \left| \sum_{n=1}^N e^{-i\mathbf{q} \cdot \mathbf{r}_n} \right|^2. \quad (42)$$

The equation above states the direct way to compute the SF of an ensemble with the structures located at positions \mathbf{r}_n . A second possibility is to calculate the SF from FOURIER transforming the Cartesian TPCF [53]. This method is commonly referred to as the FOURIER transform method. However, we have found that this method is computationally more expensive and often less accurate, which is why we utilize only the direct method of Eq. (42). Besides the fact that the SF is closely related to the angular scattering intensity, it also reveals the occurrence of spatial frequencies, which makes it a powerful tool for spatial frequency analysis. This gets particularly clear when we rearrange Eq. (42):

$$S(\mathbf{q}) = \frac{1}{N} \left| \sum_{n=1}^N \delta(\mathbf{r} - \mathbf{r}_n) e^{-i\mathbf{q} \cdot \mathbf{r}} \right|^2. \quad (43)$$

Thus, it resembles the FOURIER transform

$$F(\mathbf{q}) = \mathcal{F}[f(\mathbf{r})] = \int f(\mathbf{r}) e^{-i\mathbf{q} \cdot \mathbf{r}} d\mathbf{r}. \quad (44)$$

Consequently, we have now found various metrics that are suitable to characterize the spatial and reciprocal properties of disordered metasurfaces. To get a better feeling for these metrics, we discuss the metrics for several different disordered samples in the following.

Figure 7 shows three different metrics for the unperturbed case of a periodic grid of 50×50 structures. Since this case is highly non-isotropic, the radial TPCF is less suitable for characterization. Nevertheless, the strongly pronounced and spatially very confined peaks suggest that there must be some kind of order. The Cartesian TPCF strongly resembles the unperturbed structure distribution itself. Furthermore, the spatial frequencies of $q_x = 2\pi/p_x$ and $q_y = 2\pi/p_y$ can be nicely deduced from the SF.

Figure 8 shows the same structure after increasing the disorder strength to $s_d = 50\%$. The radial TPCF gains significance, since introducing disorder increases the isotropy of the ensemble. The peak positions of $\xi(r)$ are at multiples of the periodicities $p = p_x = p_y$ and exhibit a linewidth of approximately $p/2$, which is in very good agreement with the disorder strength. The same holds true for the Cartesian TPCF, which exhibits broadened peaks due to the introduced positional disorder. However, the SF still looks very much the same as the unperturbed case, which indicates that the spatial frequencies of the unperturbed sample are still dominating. Nevertheless, comparing the colorbars in Figs. 7(d) and 8(d) implies that the amplitudes have indeed dropped by a factor of two.

In Fig. 9, the metasurface is depicted for a disorder strength of $s_d = 200\%$. At this point, most of the features originated from the periodicity of the unperturbed grid have vanished in both TPCFs. However, both TPCFs exhibit a minimum distance below which the probability to have a neighboring structure is much lower compared to a uniformly randomized sample,

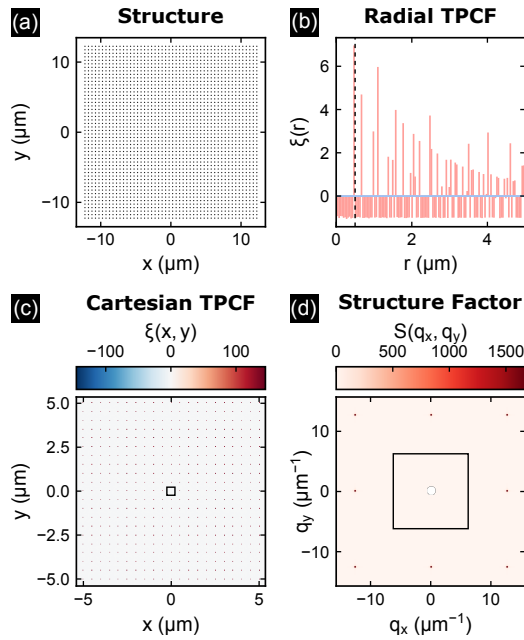


Fig. 7. Disorder metrics for the completely ordered periodic array with $s_d = 0\%$ and $l_c = 0\%$. (a) Top view on the ensemble of structures with (b)–(d) being different metrics that characterize the disorder. The black lines indicate (b) periodicity, (c) unit cell, and (d) first BRILLOUIN zone of the unperturbed grid. Each peak in (b) and (c) corresponds to another particle in the ensemble. The decay in (b) is due to the finite size of the disordered array, which results in fewer particles at large distances. (d) The structure factor emphasizes the discrete spatial frequencies of the unperturbed structures in (a). The zeroth order is removed from the SF so that features at higher frequencies are emphasized.

which is indeed a remnant of the unperturbed periodic grid. In contrast to TPCFs, the SF still shows rather distinct peaks at the spatial frequencies of the unperturbed sample. Nevertheless, the maximum amplitude has decreased by a factor of about 50 compared to the unperturbed case in Fig. 7. This facilitates the visibility of weak spatial frequencies that arise due to the introduced disorder. These quasi-random spatial frequencies still have a lower limit at about $2.5 \mu\text{m}^{-1}$ since large spatial separations of neighboring structures are unlikely.

In Fig. 10, the completely disordered case is depicted, which corresponds to a disorder strength of $s_d \rightarrow \infty$. In this special case, the structures are uniformly distributed over the same range as in the unperturbed case in Fig. 7. This causes an equally distributed noise to be present in all three metrics. In the case of TPCFs, this means that there is no kind of correlation, which is in good agreement with expectations. The uniform noise in the SF indicates that all spatial frequencies are equally present in the structure distribution.

The effects of correlation are shown in Fig. 11 for a correlation length of $l_c = 400\%$ and disorder strength of $s_d = 50\%$. Both TPCFs reveal that the introduced correlation has a twofold effect. The short-range correlation is increased compared to the uncorrelated case in Fig. 8. However, the long-range correlations are strongly disrupted at the same time. The radial and Cartesian TPCFs reveal that the short-range interactions reach up to two to three periodicities in each direction, which is consistent with

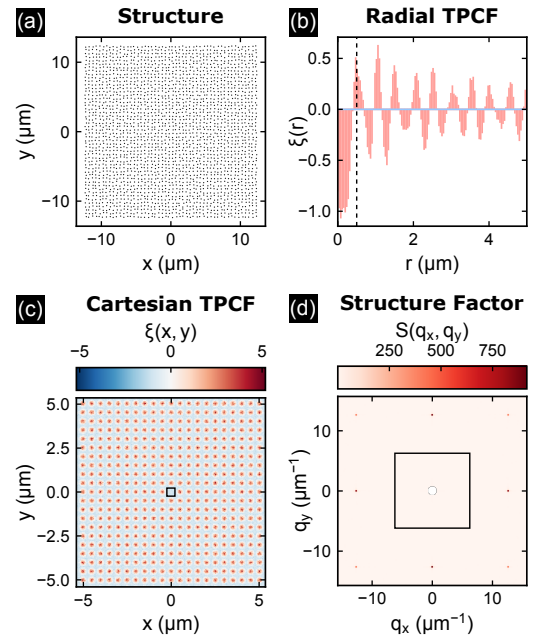


Fig. 8. Same as Fig. 7, but for $s_d = 50\%$ and $l_c = 0\%$. Both peaks exhibit broadened peaks around the periodicity of the unperturbed sample. At 50% disorder strength, particularly the diagonal peaks of the structure factor in (d) have weakened in comparison to the unperturbed case in Fig. 7. The zeroth order is removed from the SF so that features at higher frequencies are emphasized.

the correlation length of $l_c = 400\%$. These short-range correlations foster the formation of small 2×2 or 3×3 sub-grids with

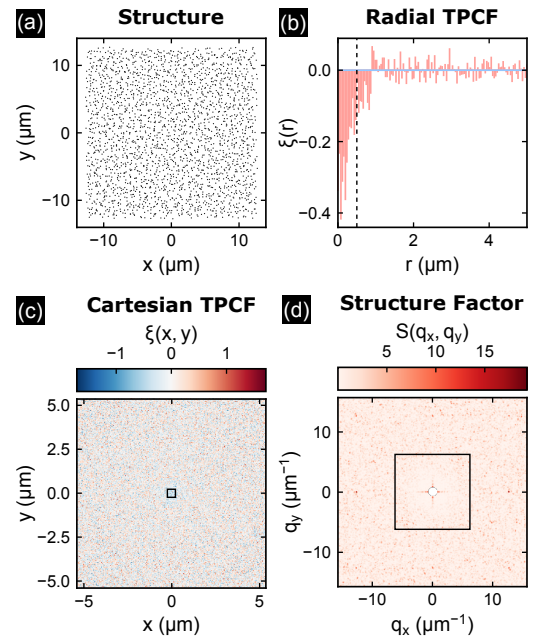


Fig. 9. Same as Fig. 7, but for $s_d = 200\%$ and $l_c = 0\%$. The peaks of the radial and Cartesian TPCFs have completely vanished at 200% disorder strength. Only a minimum distance is still visible as remnant of the initial grid. Looking closely, the structure factor indicates that more spatial frequencies are emerging in the disordered ensemble. However, spatial frequencies below $\approx 2.5 \mu\text{m}^{-1}$ are unlikely since large spatial separations between two neighboring structures are restricted for the uniform PDF.

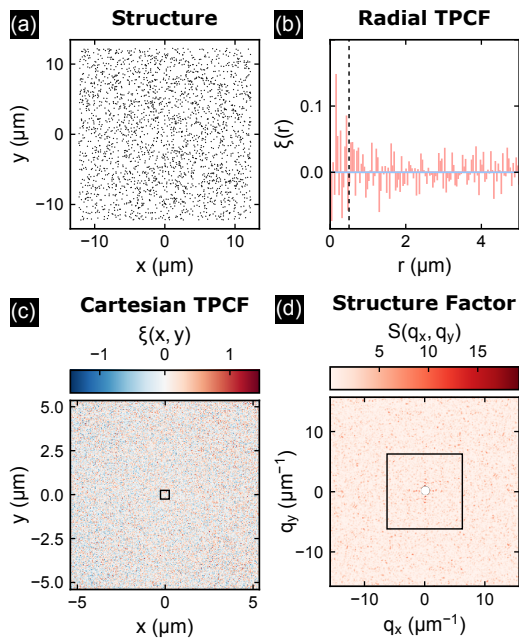


Fig. 10. Same as Fig. 7, but for $s_d \rightarrow \infty$ and $l_c = 0\%$. The radial and Cartesian TPCFs are almost completely arbitrary in the case of a truly randomized sample. In contrast to Fig. 9, there is neither a minimum nor a maximum distance between neighboring structures. However, slightly higher values can be observed in (b) for distances below $p_x = p_y$, since the average particle density is equal to Fig. 7.

slightly different periodicities and orientations. This finding is reinforced by the SF, which reveals the occurrence of scattered peaks around the spatial frequencies present in the unperturbed sample in Fig. 7.

C. Image- and FOURIER-Plane Imaging

So far, we have discussed different metrics that allow one to characterize structural information of disordered metasurfaces. However, these metrics can be utilized only if the precise distribution of the structures is known. In the case of nanostructures, it is necessary to use diffraction-limited and high NA optics, so that the structural information can be optically resolved. However, such optical setups are usually associated with high costs. This poses the question whether there are cheaper methods that allow one to achieve diffraction-limited imaging. Indeed, there exist various approaches for so called lensless imaging that originates from x-ray applications [54,55], as the materials of conventional lenses are highly absorptive in the x-ray regime. These approaches take advantage of the FRAUNHOFER approximation, which states that the diffraction pattern in the far field corresponds to the FOURIER transform of the diffractive element. In principle, this allows one to reconstruct the diffractive element (e.g., a metasurface) by FOURIER transforming the far field. Unfortunately, due to experimental limitations, it is possible to measure only the amplitudes and not the phase of the electromagnetic far field in the x-ray and optical regimes. This problem is known as the phase problem and discards the possibility to retrieve the structure of the diffractive element via the inverse FOURIER transform. However, there exist

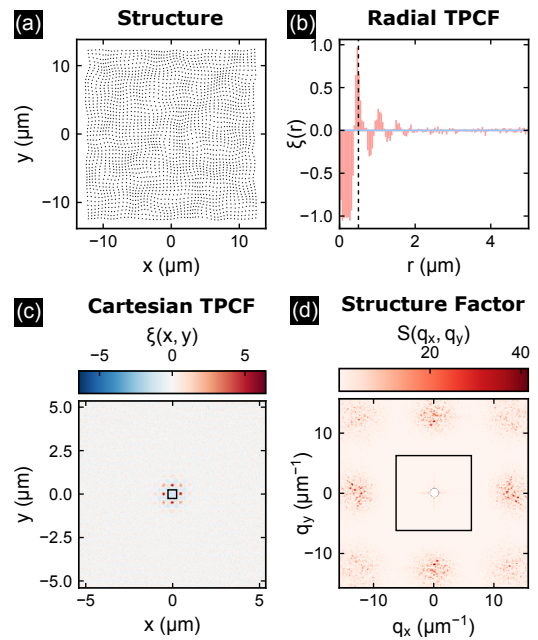


Fig. 11. Same as Fig. 7, but for $s_d = 50\%$ and $l_c = 400\%$. Both TPCFs in (b) and (c) show that the introduced correlation increases the short-range correlation, while breaking the long-range correlation. Particularly the Cartesian TPCF unveils that the correlation affects the four closest neighbors in x and y directions, which is concurrent with the correlation length of $l_c = 400\%$. The short-range correlation facilitates the creation of many small sized sub-grids that are differently oriented and thus spread the diffraction patterns in (d) around the original positions of the unperturbed grid.

various computational approaches that make weak assumptions about the structure of the diffractive element and thus provide the possibility to reconstruct the diffractive element [56,57]. Before discussing these computational approaches, we introduce a lens-based and purely optical approach that allows one to FOURIER transform and inverse FOURIER transform the diffractive elements without loss of the phase information. The idea behind this approach can be understood in terms of a $4f$ system and is visualized in Fig. 12. A $4f$ system consists of two lenses (L_1 and L_2) and a sample placed in the front focal plane of L_1 . Lenses L_1 and L_2 are arranged such that the back focal plane of L_1 and the front focal plane of L_2 overlap. The simplest way to quantitatively describe the $4f$ system is by using the ray transfer matrix analysis, which describes light as rays that propagate with an angle of θ_x at position x . Here, we define each ray to be described by the vector

$$\mathbf{r} = \begin{pmatrix} x \\ \theta_x \end{pmatrix}, \quad (45)$$

while the propagations in z direction and through thin lenses with focal length f are described by the matrices

$$\mathbf{P}_z = \begin{pmatrix} 1 & z \\ 0 & 1 \end{pmatrix}, \quad (46a)$$

$$\mathbf{L}_f = \begin{pmatrix} 1 & 0 \\ -1/f & 1 \end{pmatrix}. \quad (46b)$$

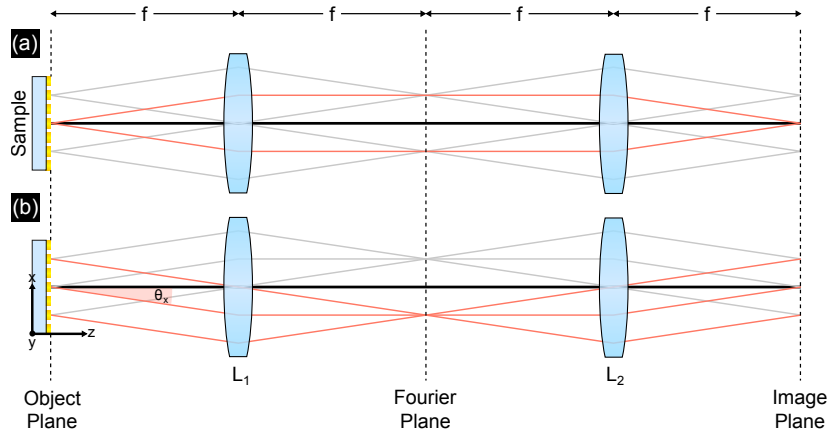


Fig. 12. Explanation of the image and FOURIER planes. (a) Each structure of the sample placed in the front focal plane of L_1 radiates light in different directions. Two rays of the light emitted by the central structure are highlighted in red, so that they can be traced easily. All rays that originate from the same point in the front focal plane must be parallel after passing L_1 . This requires that these parallel beams are imaged in the back focal plane of L_2 . Hence, the back focal plane of L_2 must be conjugated to the image plane. (b) Rays emitted in the same direction but from different locations on the sample must coincide in the back focal plane of L_1 . This means that each point in the back focal plane of L_1 corresponds to light emitted into a certain solid angle. Since the radiation angle θ_i ($i = [x, y]$) relates to the reciprocal coordinates k via $\sin(\theta_i) = k_i/k$, it is possible to convert between spatial coordinates r and reciprocal coordinates k with a $4f$ system for any given wavelength $\lambda = 2\pi/k$.

Hence, any ray that is radiated from the front focal plane of L_1 is given as

$$\begin{pmatrix} x' \\ \theta'_x \end{pmatrix} = \mathbf{P}_f \cdot \mathbf{L}_f \cdot \mathbf{P}_f \cdot \begin{pmatrix} x \\ \theta_x \end{pmatrix} = \begin{pmatrix} 0 & f \\ -1/f & 0 \end{pmatrix} \begin{pmatrix} x \\ \theta_x \end{pmatrix} \quad (47)$$

in the back focal plane of L_1 and as

$$\begin{pmatrix} x'' \\ \theta''_x \end{pmatrix} = \mathbf{P}_f \cdot \mathbf{L}_f \cdot \mathbf{P}_{2f} \cdot \mathbf{L}_f \cdot \mathbf{P}_f \cdot \begin{pmatrix} x \\ \theta_x \end{pmatrix} = \begin{pmatrix} -1 & 0 \\ 0 & -1 \end{pmatrix} \begin{pmatrix} x \\ \theta_x \end{pmatrix} \quad (48)$$

in the back focal plane of L_2 . Hence, the back focal plane of L_2 must be an image plane, as each ray that originates from position x and propagates in direction θ_x ends up at position $-x''$ with an angle of $-\theta''_x$. In contrast to that, Eq. (47) proves that position x' and angle θ'_x in the back focal plane of L_1 reciprocally depend on angle θ_x and position x at the sample site. To prove that position x and angle θ_x are indeed reciprocal quantities, we can consider light diffracted by a periodically structured sample with periodicity p_x :

$$\sin(\theta_x) = \frac{m\lambda}{p_x}. \quad (49)$$

Here, $m \in \mathbb{Z}$ specifies the diffraction order. Since the spatial frequency $q_x = 2\pi/p_x$ is inversely proportional to the periodicity, we can rewrite the diffraction angle θ_x in terms of the spatial frequency q_x and wavenumber k as

$$\sin(\theta_x) = \frac{mq_x}{k}. \quad (50)$$

This already proves that for any given wavelength $\lambda = 2\pi/k$, spatial frequency q_x is proportional to propagation angle θ_x , and hence, θ_x and spatial coordinate x must be reciprocal quantities. Consequently, the field distribution in the back focal plane of L_1 is actually the FOURIER transform of the field distribution in the

front focal plane of L_1 . If we now recall that the x component of wavenumber k is given by the sine of the diffraction angle, we can state that

$$k_x = mq_x, \quad (51)$$

which induces that the components of wave vector \mathbf{k} are integer multiples of the spatial frequencies that occur in the diffracting sample and therefore hold structural information about the sample. This is also the reason that the back focal plane of L_1 is often referred to as the FOURIER plane or k -space, which is the reciprocal plane to the image plane or real space, respectively. The previous findings imply that there must be a way to relate structural information of the diffractive sample with the diffraction pattern in the FOURIER plane. Indeed, the SF defined in Eq. (41) allows one to derive the intensity distribution in k -space. Therefore, we redefine the form factors f_j as complex valued scattering amplitudes $\mathbf{E}_i(\mathbf{q})$, which yields

$$I(\mathbf{q}) = \sum_{i=1}^N \sum_{j=1}^N \mathbf{E}_i(\mathbf{q}) \mathbf{E}_j^*(\mathbf{q}) e^{-i\mathbf{q}(\mathbf{r}_i - \mathbf{r}_j)} \quad (52)$$

for samples consisting of structures with different scattering amplitudes. In the case of identical structures, the latter equation simplifies to

$$I(\mathbf{q}) = |\mathbf{E}(\mathbf{q})|^2 \cdot \left| \sum_{i=1}^N e^{-i\mathbf{q}\mathbf{r}_i} \right|^2, \quad (53a)$$

$$\stackrel{\text{Eq. (42)}}{=} N \cdot |E(\mathbf{q})|^2 \cdot S(\mathbf{q}). \quad (53b)$$

Because of this relation, the intensity $I(\mathbf{q})$ in the FOURIER plane can be decomposed into contributions from the SF $S(\mathbf{q})$ and the intensity $|E(\mathbf{q})|^2$ radiated from individual structures. Piechulla *et al.* [19] discussed the relation between the SF and optical quantities for disordered ensembles of PMMA

nanospheres in great detail. It should not go unmentioned that the intensity distribution that results from Eq. (53b) does not consider any kind of coupling between structures.

Now that we have clarified the physical relation between the image and FOURIER planes, we can move on to discuss how these insights can be utilized for lensless imaging and tailored k -space designs, eventually.

1. Lensless Imaging

The main idea behind lensless imaging comes from the FRAUNHOFER approximation, which states that the structure of a diffracting sample can be reconstructed from the diffracted wave by FOURIER transforming the far field. This approach is used in various fields such as x-ray- or electron-based imaging, where the usage of lenses is difficult due to material shortcomings [54,55,58]. However, lensless imaging is also of interest for optical applications, particularly for imaging macroscopically extended samples with microscopic features that can not be placed within an optical setup.

The main limitation of this approach is that the phase and amplitude information of the electromagnetic fields in the FOURIER plane must be known to reconstruct the original image. Unfortunately, the bandwidth of currently available photodetectors restricts the measurement of phase information in the optical regime. Thus, only the amplitude of optical waves is experimentally available in the FOURIER plane. Nevertheless, there exist various computational approaches that allow one to recover the missing phase information under certain conditions.

Among the iterative approaches, the Gerchberg and Saxton (GS), hybrid input–output (HIO), and oversampling smoothness (OSS) algorithms are arguably the most popular and established approaches [56,57,59,60]. All of them have in common that they repeatedly transform the known FOURIER-plane amplitudes into the image plane and back, while imposing certain constraints on the retrieved amplitudes and phases. To work, the available data must meet certain criteria.

First of all, it is necessary that the known FOURIER-plane field amplitudes are oversampled. In other words, this means that the extent (support) of the image-plane field distribution has to be smaller than the area of the image plane that is recovered. Second, it is necessary to have a good estimate of this support region in the image plane. The size of the support region can be acquired, for instance, by low resolution optics or by using an aperture of known size that artificially limits the support.

From now on, we refer to the support region as S and the electric fields in the FOURIER plane as $E_F(\mathbf{q})$ and in the image plane as $E_I(\mathbf{r})$. Thus, the task of phase-retrieval algorithms is to retrieve the complex-valued fields $E_I(\mathbf{r})$ given the support region S and the oversampled field amplitudes in the FOURIER plane $|E_F(\mathbf{q})|$. The HIO and OSS algorithms tackle this problem very similarly, although there is an additional step in the OSS approach that improves the convergence, robustness against noise, and consistency [56]. In both cases, the initialization is carried out by multiplying $|E_F(\mathbf{q})|$ with a random phase. From this point, the HIO algorithm repeatedly applies the following steps.

1. Inverse FOURIER transform $E_F(\mathbf{q})$ to get $E'_I(\mathbf{r})$.
2. Impose the image-plane constraints

$$E_I^{i+1}(\mathbf{r}) = E_I^i(\mathbf{r}) - \beta E'_I(\mathbf{r}) \quad \text{for } (\mathbf{r} \notin S) \cup (\mathbf{r} \in C).$$

3. FOURIER transform $E_I^{i+1}(\mathbf{r})$ to get $E'_F(\mathbf{q})$.
4. Impose the FOURIER-plane constraints

$$E_F(\mathbf{q}) = |E_F(\mathbf{q})| E'_F(\mathbf{q}) / |E'_F(\mathbf{q})|.$$

For $i = 0$, we choose $E_I^i(\mathbf{r}) = E'_I(\mathbf{r})$ to start off. Parameter $\beta \in [0.5, 1]$ is the step width, and C indicates the set of values that violate the image-plane constraints. These constraints C can be anything known *a priori* about the image plane. The presumably weakest constraint is the so called nonnegativity constraint, which states that $E_I(\mathbf{r})$ must be real and nonnegative [60]. We have extended this constraint so that $E_I(\mathbf{r})$ can be chosen to be larger than a specified percentile of $E_I(\mathbf{r})$. This has empirically shown to be sometimes beneficial for the convergence of sparse image-plane distributions. As mentioned previously, the OSS approach is very similar but has an additional step that makes the algorithm more robust [56,57].

1. Inverse FOURIER transform $E_F(\mathbf{q})$ to get $E'_I(\mathbf{r})$.
2. Impose the image-plane constraints

$$E_I''(\mathbf{r}) = E_I^i(\mathbf{r}) - \beta E'_I(\mathbf{r}) \quad \text{for } (\mathbf{r} \notin S) \cup (\mathbf{r} \in C)$$

3. Perform the OSS step

$$E_I^{i+1}(\mathbf{r}) = \mathcal{F}^{-1} \left[E_F''(\mathbf{q}) G(\mathbf{q}, \sigma_i) \right] \quad \text{for } \mathbf{r} \notin S.$$

4. FOURIER transform $E_I^{i+1}(\mathbf{r})$ to get $E'_F(\mathbf{q})$.
5. Impose the FOURIER-plane constraints

$$E_F(\mathbf{q}) = |E_F(\mathbf{q})| E'_F(\mathbf{q}) / |E'_F(\mathbf{q})|.$$

The function $G(\mathbf{q}, \sigma_i)$ in the OSS step is a GAUSSIAN smoothing function with zero mean and decreasing variance σ_i^2 that filters out high frequencies outside the support region S . A strategy that describes how σ_i can be chosen is discussed in much detail in Ref. [57]. For both phase-retrieval algorithms, it is recommended to perform multiple random phase initializations to increase the chance to converge against the global minimum. We utilize the root mean squared logarithmic error (RMSLE) as a metric to judge convergence quality. For our application, it has shown to be superior to the root mean squared error (RMSE), as it lowers the influence of the strongly pronounced but less important zeroth order in the FOURIER plane.

Figure 13 shows the strength of the HIO and OSS algorithms for a sample with disorder parameters $n_x = n_y = 10$, $p_x = p_y = 1 \mu\text{m}$, $s_d = 100\%$, and $l_c = 200\%$. After only about 100 iterations and 10 initializations of the initial random phase, the HIO and OSS algorithms show already very good agreement with the actual image plane. However, the OSS algorithm further converges in contrast to the HIO algorithm and exhibits excellent agreement with the ground truth after 10,000 steps. Thus, we choose the OSS algorithm for any further results in this tutorial if not stated differently.

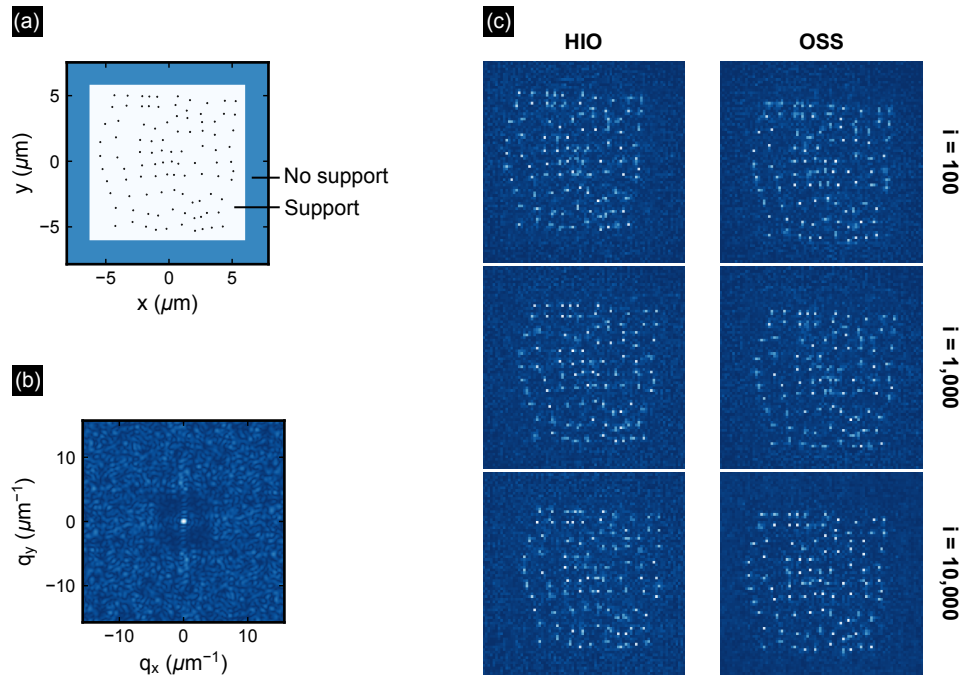


Fig. 13. Phase retrieval for lensless imaging. (a) The original structure distribution is indicated by black points. The white region is the *a priori* known support of the structures and specifies the approximate sample extent. (b) The structure factor of the sample in (a) is the basis of the phase-retrieval algorithm and the only known information together with the sample support S . (c) Comparison of the retrieved image-plane amplitudes after different numbers of steps using the HIO and OSS approaches. The OSS algorithm shows better contrast after 10,000 steps and is therefore favored.

D. Color Science

Color science describes the conversion process from physical properties such as spectral intensities to perceivable colors. Thus, an accurate color model is required to predict the appearance of disordered plasmonic metasurfaces.

The CIE 1931 XYZ color space is one of the most common color spaces and allows one to convert spectral intensities to so called XYZ tristimulus values and eventually RGB values. Similar to the S-, M-, and L-cones of the human eye, the CIE standard observer XYZ color matching functions $\bar{x}(\lambda)$, $\bar{y}(\lambda)$, and $\bar{z}(\lambda)$ are introduced. They are shown in Fig. 14(a) and weight the spectral intensities according to the sensitivity of the human eye. For reflective or transmittive surfaces with reflectance or transmittance $P(\lambda)$, the color appearance fundamentally depends on the spectral intensity distribution $I(\lambda)$ of the illuminating light source:

$$X = \int \bar{x}(\lambda) P(\lambda) I(\lambda) d\lambda, \quad (54a)$$

$$Y = \int \bar{y}(\lambda) P(\lambda) I(\lambda) d\lambda, \quad (54b)$$

$$Z = \int \bar{z}(\lambda) P(\lambda) I(\lambda) d\lambda. \quad (54c)$$

However, within the frame of this work, the illuminant $I(\lambda)$ is chosen such that it has equal power at each wavelength λ . This implies that suitable reference measurements have to be conducted in the experiments to ensure that the spectral influence of the illuminating light source is cancelled out.

It is often desirable to transform the CIE XYZ color space to the CIE xyY color space, which is achieved by normalizing the XYZ tristimulus values

$$x = \frac{X}{(X + Y + Z)}, \quad (55a)$$

$$y = \frac{Y}{(X + Y + Z)}, \quad (55b)$$

$$z = \frac{Z}{(X + Y + Z)} = 1 - x - y. \quad (55c)$$

Since coordinate z is dependent only on chromaticity coordinates x and y , it is not required to consider it hereafter. The xyY representation allows one to distinguish between chromaticity coordinates x and y and luminance Y , which expresses only the brightness of a color independent of its chromaticity. This enables to represent any color solely by specifying chromaticity coordinates x and y , as can be seen in the CIE 1931 chromaticity diagram in Fig. 14(b).

The back transformation from chromaticity coordinates x and y to the XYZ tristimulus can be accomplished by choosing an arbitrary luminance $Y = Y_0$:

$$X = Y_0 \cdot \frac{x}{y}, \quad (56a)$$

$$Y = Y_0, \quad (56b)$$

$$Z = Y_0 \cdot \frac{(1 - x - y)}{y}. \quad (56c)$$

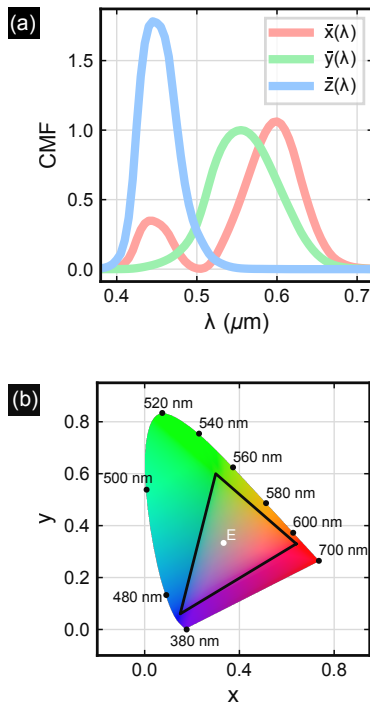


Fig. 14. Color matching functions and CIE 1931 chromaticity diagram. (a) The CIE color matching functions $\bar{x}(\lambda)$, $\bar{y}(\lambda)$, and $\bar{z}(\lambda)$ weight the spectral intensities that are reflected, transmitted, or radiated by the sample of interest. By converting the obtained XYZ color space to the xyY color space, it is possible to represent any perceivable color with the chromaticity coordinates x and y . The CIE 1931 chromaticity diagram in (b) shows all colors at a fixed luminance $Y = Y_0$ for different coordinates x and y . All visible monochrome wavelengths constitute the border of the chromaticity diagram. The corners of the triangle inside the chromaticity diagram indicate the coordinates of the red, green, and blue primaries of the sRGB gamut with the equal energy white point E lying inside the triangle. Only colors within the triangle can be represented using this sRGB gamut.

The previous relations are important to understand the transition from the XYZ tristimulus to RGB values, which are connected by a single matrix \mathbf{M} :

Table 2. Chromaticity Coordinates of the Equal Energy White Point and sRGB Primaries

	White Point	R. Primary	G. Primary	B. Primary
x	0.33	0.64	0.3	0.15
y	0.33	0.33	0.6	0.06

$$\begin{pmatrix} X \\ Y \\ Z \end{pmatrix} = \mathbf{M} \begin{pmatrix} R \\ G \\ B \end{pmatrix}. \quad (57)$$

However, the entries of \mathbf{M} depend on the chosen color gamut and white point, which define the pure red, green, blue, and white of the respective color space. In contrast to the white point, the red, green, and blue primaries are adapted from the widely used sRGB gamut. The reason for this is that the equal energy illuminant E is used in this work, whereas the sRGB color space is defined in terms of the so-called D65 illuminant. Figure 14(b) and Table 2 show the coordinates of the sRGB primaries and the equal energy white point E.

Independent of the specific RGB primaries and white point, matrix \mathbf{M} is given as

$$\mathbf{M} = \begin{pmatrix} X_r & X_g & X_b \\ Y_r & Y_g & Y_b \\ Z_r & Z_g & Z_b \end{pmatrix} \begin{pmatrix} S_r & 0 & 0 \\ 0 & S_g & 0 \\ 0 & 0 & S_b \end{pmatrix}, \quad (58)$$

whereas the auxiliary values S_r , S_g , and S_b are defined as

$$\begin{pmatrix} S_r \\ S_g \\ S_b \end{pmatrix} = \begin{pmatrix} X_r & X_g & X_b \\ Y_r & Y_g & Y_b \\ Z_r & Z_g & Z_b \end{pmatrix}^{-1} \begin{pmatrix} X_w \\ Y_w \\ Z_w \end{pmatrix}. \quad (59)$$

Indices r , g , b , and w indicate that the XYZ values belong to the red, green, and blue primaries or the white point, respectively. These relations allow one to compute RGB values by inverting matrix \mathbf{M} and using Eq. (57). So far, the color model has not considered that human perception of brightness is strongly nonlinear in the physical intensity of light. This means

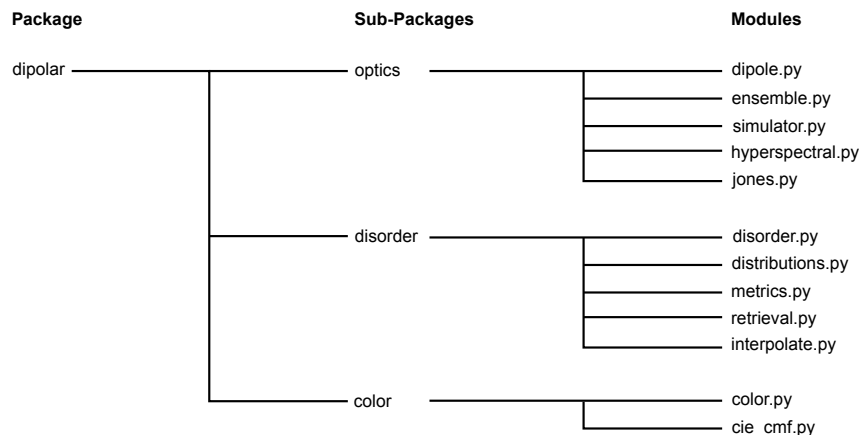


Fig. 15. Architecture of the *dipolar* package. The *dipolar* package is implemented using PYTHON and consists of the *optics*, *disorder*, and *color* sub-packages. These sub-packages represent the three major fields covered in this tutorial and contain all modules in which the details of Section 2 are implemented. The *optics* sub-package covers all models necessary to compute light–matter interactions. Algorithms required for the generation and characterization of (disordered) metasurfaces belong to the *disorder* sub-package, and all color science models essential for the conversion from spectral data to RGB comprise the *color* sub-package.

that at this point, the RGB values are linear and require a γ correction to match human perception. In the case of sRGB color space, the transformation from linear RGB to sRGB is defined as

$$\gamma(u) = \begin{cases} 12.92 \cdot u & u \leq 0.0031308 \\ 1.055 \cdot u^{1/2.4} - 0.055 & \text{otherwise,} \end{cases} \quad (60)$$

where u is the R , G , or B color channel. The sRGB γ -correction is also utilized in this tutorial and completes the color model, which now provides a holistic approach to convert physical intensities to subjective color and brightness impressions.

3. SOFTWARE DESIGN

The aim of this section is to give a short overview on the implementation of the CPDA and the associated disorder and color science models. Thus, the CPDA package will be introduced only so far that the reader has a rough idea of its architecture and knows about the meaning of the most relevant simulation parameters and their impact on the simulation results in Section 4.

The CPDA package is named *dipolar* and is implemented with PYTHON because of the availability of many well-documented open-source packages that provide the possibility to share the full package with the scientific community, once all required functionalities are implemented. A discussion about interesting functionalities that remain to be implemented can be found in Section 6.

As shown in Fig. 15, the *dipolar* package is divided into three sub-packages that correspond to the major fields in this tutorial, which are light–matter interaction models (*optics* sub-package), disorder models (*disorder* sub-package), and color science models (*color* sub-package). Together with the object-oriented implementation of many modules, this ensures the modularity and scalability of the project.

A. Optics Sub-package

The *optics* sub-package comprises the *dipole.py*, *ensemble.py*, *simulator.py*, *hyperspectral.py*, and *jones.py* modules. From those, the first three modules are the most crucial, as they are inevitable for computation of the optical response of plasmonic metasurfaces. Each of these three modules contains a single class that is named like the module itself. The idea behind these classes is that each instance represents a certain unit in the real physical experiment.

An instance of the *Dipole* class represents an individual structure of the plasmonic metasurface and contains the polarizability, position, and orientation of that structure as attributes. The wavelength dependent polarizabilities must be known beforehand and can be computed using FEM or FIT solvers such as COMSOL Multiphysics, CST Microwave Studio, Lumerical, or any other suitable software. All polarizabilities used within this tutorial are acquired via COMSOL Multiphysics.

The *Ensemble* class represents the entirety of metasurfaces and contains all *Dipole* instances contained within this metasurface. This wrapper class provides the possibility to get and set the properties of all dipoles (e.g., position or orientation) at once and is used to construct the *Simulator* object that computes the optical properties of the ensemble.

In principle, it is possible to instantiate the *Simulator* object only by passing the corresponding *Ensemble* instance and the simulation wavelengths as input arguments. Figure 16 shows the most relevant simulation parameters that can be specified as attributes of the *Simulator* instance. These parameters are polar and azimuthal angles θ_i and ϕ_i of the incident plane wave, material independent NA of the objective $\text{NA} = \sin(\theta_{\max})$, permittivity and permeability of the surrounding material ϵ and μ , resolution of the spatial simulation grid $n_{\text{px},x}$ and $n_{\text{px},y}$, scaling factors for the simulated area in image and FOURIER planes δ_i and δ_f , respectively, and height of the simulation volume Δz . Within the scope of this work, the default values of these parameters are $\theta_i = 0^\circ$, $\phi_i = 0^\circ$, $\text{NA} = 1$, $\epsilon = 2.25$, $\mu = 1$, $n_{\text{px},x} = 256$, $n_{\text{px},y} = 256$, $\delta_i = \delta_f = 1$, and $\Delta z = 0$, respectively.

Depending on these simulation parameters, the complex-valued electric field amplitudes in the FOURIER plane, α_{xx}^f , α_{xy}^f , α_{yx}^f , and α_{yy}^f , are computed using the CPDA model introduced in Sections 2.A.1 and 2.A.2. Here, the subscripts indicate the polarization states of incoming or outgoing fields. With these four components, it is possible to express outgoing field \mathbf{E}_{out} in dependence of any normalized incoming field \mathbf{E}_{in} according to the JONES calculus as

$$\mathbf{E}_{\text{out}} = \hat{M}_{\text{post}} \cdot \begin{pmatrix} \alpha_{xx} & \alpha_{yx} \\ \alpha_{xy} & \alpha_{yy} \end{pmatrix} \cdot \hat{M}_{\text{pre}} \cdot \mathbf{E}_{\text{in}}. \quad (61)$$

Matrices \hat{M}_{pre} and \hat{M}_{post} are JONES matrices that allow one to manipulate the polarization state of light before and after interaction with the sample and can be calculated using the *jones.py* module of the *optics* sub-package. The superscripts and arguments of the complex field amplitudes in Eq. (61) have been left out deliberately, as it equally holds true for the complex electric field amplitudes in the image plane, α_{xx}^i , α_{xy}^i , α_{yx}^i and α_{yy}^i , obtained via FFT. Thus, the metasurface can be probed with unpolarized light or any other polarization state that can be expressed in terms of the JONES calculus. If not stated differently, the simulation results are shown for unpolarized light.

For n_λ simulation wavelengths, each of the eight complex field amplitudes α_{xx}^f , α_{xy}^f , α_{yx}^f , α_{yy}^f , α_{xx}^i , α_{xy}^i , α_{yx}^i , and α_{yy}^i are of size $n_{\text{px},x} \times n_{\text{px},y} \times n_\lambda$. For discretization of the reciprocal space, reciprocal grid coordinates K_x and K_y are computed via

$$K_x = k_{\max} \cdot \left(\frac{2 \cdot n}{n_{\text{px},x} - 1} - 1 \right), \quad n = 0, 1, \dots, n_{\text{px},x} - 1, \quad (62a)$$

$$K_y = k_{\max} \cdot \left(\frac{2 \cdot m}{n_{\text{px},y} - 1} - 1 \right), \quad m = 0, 1, \dots, n_{\text{px},y} - 1, \quad (62b)$$

with k_{\max} being the largest wavenumber deduced from the smallest specified simulation wavelength. After computing the complex electric fields for each $K_{x,y}$, the values outside the specified NA are set to zero. Grid coordinates X and Y of the real space are obtained through

$$X = \left(x_{\text{d},\min} - \frac{\delta x}{2} \right) + n \cdot \Delta x, \quad n = 0, 1, \dots, n_{\text{px},x} - 1, \quad (63a)$$

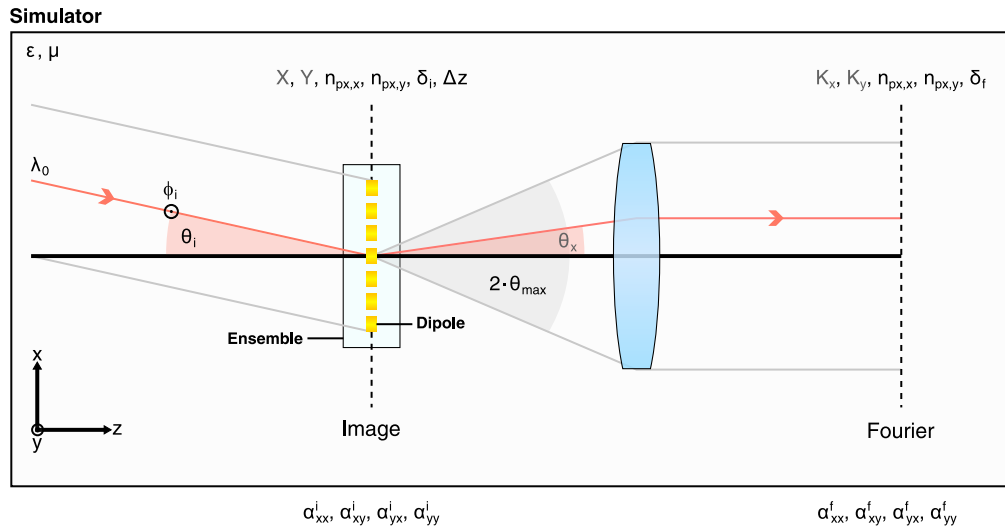


Fig. 16. Explanation of the CPDA simulation parameters. Despite the fact that all simulations are carried out in reflection, the simulation parameters are explained in transmission for better clarity and without loss of generality. The three bold terms correspond to the classes implemented to compute the optical response of plasmonic metasurfaces. Each instance of the *Dipole* class has polarizability, position, and orientation as attributes. The *Ensemble* class wraps all *Dipole* instances of a sample and allows one to access the attributes of all dipoles at once. This *Ensemble* instance is then passed to the *Simulator* class together with several simulation parameters, which are the surrounding material properties ϵ and μ , vacuum wavelength of incident light λ_0 , polar and azimuthal angles θ_i and ϕ_i of the incident plane wave, material-independent numerical aperture of the objective $\text{NA} = \sin(\theta_{\max})$, resolution of the spatial simulation grid $n_{\text{px},x}$ and $n_{\text{px},y}$, scaling factors for the simulated area in image and FOURIER planes δ_i and δ_f , and height of the simulation volume Δz . From these parameters, the complex electric field amplitudes in the FOURIER plane are computed, which yield the complex electric field amplitudes in the image plane using the FOURIER transform (FFT). The remaining gray attributes shown above are derived from the previously mentioned parameters.

$$Y = \left(y_{d,\min} - \frac{\delta y}{2} \right) + m \cdot \Delta y, \quad m = 0, 1, \dots, n_{\text{px},y} - 1, \quad (63b)$$

with $x_{d,\min}/y_{d,\min}$ being the coordinate of the left-/lower-most dipole in the simulated ensemble, $\delta x = \delta y = 2 \mu\text{m}$ being a fixed margin, and

$$\Delta x = \frac{(x_{d,\max} - x_{d,\min}) + \delta x}{n_{\text{px},x} - 1}, \quad (64a)$$

$$\Delta y = \frac{(y_{d,\max} - y_{d,\min}) + \delta y}{n_{\text{px},y} - 1} \quad (64b)$$

being the step size, with $x_{d,\max}/y_{d,\max}$ representing the coordinate of the right-/upper-most dipole in the simulated ensemble. The complex electric fields in real space are computed through FOURIER transform of the complex electric fields in reciprocal space. The program adjusts the grid resolution and outputs a warning in case that the choice of the real space grid violates the NYQUIST-SHANNON sampling theorem. Implementing the calculation of the reciprocal and real grid coordinates in this way ensures that the full desired ranges are simulated with the same resolution in both spaces.

The auxiliary *hyperspectral.py* module is introduced to simplify the handling of such typically large and high dimensional datasets. Briefly speaking, the *hyperspectral.py* module contains the *Hyperspectral* class, which provides methods that allow one to represent the hyperspectral field amplitudes as spatial or spectral projection for a certain polarization state of the incoming and outgoing electric fields. Furthermore, the methods of the

Hyperspectral object allow one to represent the spatial projections either as RGB appearances or as physical intensities at a certain wavelength.

B. Disorder Sub-package

In the *disorder* sub-package, all modules comprise those that can be used for the generation and characterization of (disordered) metasurfaces. It is important to mention that any arbitrary metasurface can be simulated using the *optics* sub-package and that metasurfaces are not required to be generated with the *disorder* sub-package. Nevertheless, the *disorder* sub-package particularly comes in handy if unbiased and reproducible structure distributions are required for the validation of simulation approaches, disorder metrics, or similar.

The main module of this sub-package is the *disorder.py* module, in which the *Disorder* class is implemented. This class is instantiated by passing the number of structures in x and y directions n_x and n_y as well as periodicities p_x and p_y . By calling the *positional*, *rotational*, or *dimensional* methods of the *Disorder* instance, it is possible to introduce the different disorder types in dependence of the specified disorder strength, correlation length, PDF, CF, and random seed. It is noteworthy that the order in which the methods are called yields different results in the case of correlated disorder, since the influence of correlation depends on the spatial separation of the structures. The random numbers to create positional, rotational, and dimensional disorders are generated using the MT19937 implementation of the Mersenne-Twister pseudorandom number generator providing a specific pseudorandom sequence for a

given seed [61]. If no seed is provided, an unpredictable seed is pulled from the operating system.

In the *distributions.py* module, the different PDFs introduced in Section 2.B.1 are implemented.

Furthermore, the *metrics.py* module contains the functions that compute the disorder metrics from Section 2.B.2, given a certain structure distribution.

The phase-retrieval algorithms used to recover the image-plane field distributions are implemented in the *retrieval.py* module and can be executed in parallel to speed up the multiple random phase initializations advised to use for better convergence.

The last module in the *disorder* sub-package is the *interpolate.py* module, which is required for introducing continuous dimensional disorder. As mentioned in the beginning of this section, the polarizability of each structure must be known previous to the CPDA simulations. However, this is a problem if the size deviations δS are continuous, since this would require an infinite number of polarizabilities. This problem can be overcome by providing a large body of polarizabilities and interpolating the polarizabilities of intermediate-sized structures. The *interpolate.py* module supplies the tools required for this task and therefore provides the possibility to implement continuous dimensional disorder.

C. Color Sub-package

The *color* sub-package is the third and last sub-package within the *dipolar* package. Although *cie_cmf.py* is strictly speaking also a module, it actually stores only the values of the XYZ color matching functions shown in Fig. 14. These CMFs are loaded into the *ColorSystem* class of the *color.py* module and used to convert spectral intensities to the RGB color system. Thus, it is necessary to instantiate the *ColorSystem* object by specifying the red, green, and blue primaries as well as the white point. The subsequent conversion to the RGB color system is carried out by the methods of the *ColorSystem* class and strictly follows the derivations in Section 2.D.

4. SIMULATION RESULTS

The previous section briefly introduced the implementation of the CPDA and the most relevant simulation parameters required to understand the results in this section. This section does not aim to present novel metasurfaces with unique properties but rather discusses the general capabilities of the simulation model, so that the reader can assess the usability of this approach for his or her precise use case. Discussing the simulation features on a general level also provides the possibility to check the consistency of the results with fundamental physical laws. All simulation results presented in this work are computed in reflection, meaning that only backscattered light is considered. Towards the end of this section, a second approach is introduced that allows one to compute the FOURIER-plane intensity distribution, and the applicability of phase-retrieval algorithms for so called *k*-space design is discussed.

A. Diffraction Limit

Conventional microscopy setups cannot distinguish two adjacent structures that are closer than a certain spatial distance. This fundamental limitation is due to the finite NA of any microscope, which thus restricts to capture the full diffraction pattern of a sample. Since the diffraction pattern comprises all structural information of the sample, the finite NA causes a limited spatial resolution. This limitation was initially described by ERNST ABBE in 1873 who found that the minimum spatial resolution Δx depends on the NA_C of the condenser, NA_O of the objective, and the vacuum wavelength λ_0 of the light:

$$\Delta x = \frac{\lambda_0}{NA_C + NA_O}. \quad (65)$$

This general formulation of the ABBE limit can be simplified for our simulation model. First of all, in the equation above, the NA is defined as $NA = n \cdot \sin(\theta_{\max})$. However, within this work, the NA is defined independent of the refractive index n of the surrounding material and thus as $NA = \sin(\theta_{\max})$. Second, the incident light in the CPDA model is described by a plane wave, which corresponds to central illumination, and thus, $NA_C = 0$. After adapting the diffraction limit to these specific conditions, we can reformulate the diffraction limit as

$$\Delta x = \frac{\lambda}{NA}, \quad (66)$$

with the NA being the material independent NA of the objective, and $\lambda = \lambda_0/n$.

Figure 17 shows the FOURIER and image planes for different NAs of the objective and a fixed wavelength $\lambda_0 = 0.4 \mu\text{m}$. All simulations are carried out for a periodic arrangement of 8×8 aluminum disks with a diameter of $0.12 \mu\text{m}$, height of $0.06 \mu\text{m}$, and periodicity of $0.5 \mu\text{m}$ in both directions. The simulations vividly demonstrate the implications of a limited NA. If the NA is sufficiently large to capture all diffraction orders, it is possible to distinguish each structure in the image plane. At a NA of $NA = 0.5$, the spatial resolution is $\Delta x = 0.533 \mu\text{m}$ and therefore close to the periodicity of the sample. In this case, it is barely possible to distinguish individual structures. Only due to the finite width of the (1,0), (0,1) diffraction orders are some spatial details still present in the image plane. If the NA is further reduced to $NA = 0.25$, no more spatial details are present in the image plane, since only the (0,0) diffraction order is recorded, which does not hold any spatial information. Therefore, only the borders of the sample can be resolved. Indeed, the NA not only influences the resolution limit but also affects the intensity in the image plane. This is simply caused by the circumstance that the finite NA limits the amount of backscattered optical power that can be captured by the objective. Both the NA dependent scaling of the diffraction limit and of the image-plane intensities are accurately predicted by the CPDA as shown in Fig. 17.

B. Oblique Incidence

Besides the NA of the objective, it is also possible to change the incidence angle of the plane wave that excites plasmonic structures. This is particularly important for determination of

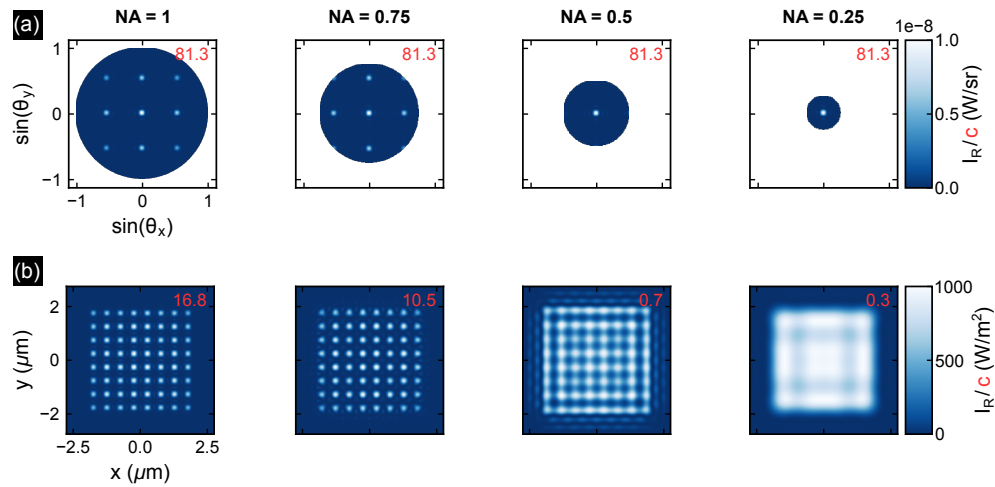


Fig. 17. NA dependent diffraction limit at normal incidence. The simulations are carried out with the CPDA for $\lambda_0 = 0.4 \mu\text{m}$, $n_x = n_y = 8$, $p_x = p_y = 0.5 \mu\text{m}$, and aluminum disks with size $0.12 \times 0.12 \times 0.06 \mu\text{m}^3$. (a) Strongly pronounced diffraction orders are visible in the FOURIER plane due to the periodic arrangement of the dipoles. At NA = 0.5, the (1,0) and (0,1) diffraction orders are hardly visible, resulting in a lowered resolution. At NA = 0.25, the structural details in the image plane (b) have fully vanished, since all diffraction orders besides the (0,0) order are outside of the observed FOURIER plane.

the BRDF, for which the incidence and reflection angle must be considered. The BRDF is defined as

$$\text{BRDF}(\theta_i, \phi_i, \theta_o, \phi_o, \lambda) = \frac{dL_o(\theta_o, \phi_o, \lambda)}{dE(\theta_i, \phi_i, \lambda)}, \quad (67)$$

where θ_i and ϕ_i are the polar and azimuthal angles of incident light, while θ_o and ϕ_o are corresponding angles for reflected light.

To get an idea of how the incidence angle affects the angle of diffraction, one can extend Eq. (49) for a reflective grating with periodicities p_x , p_y and incidence angles of $\theta_{i,x}$, $\theta_{i,y}$ [defined as $k_x = k \sin(\theta_{i,x})$ and $k_y = k \sin(\theta_{i,y})$]:

$$\sin(\theta_{i,x}) + \sin(\theta_x) = \frac{m\lambda}{p_x}, \quad (68a)$$

$$\sin(\theta_{i,y}) + \sin(\theta_y) = \frac{m\lambda}{p_y}. \quad (68b)$$

As before, θ_x and θ_y refer to diffraction angles in x and y directions, respectively, while m indicates the diffraction order. Since the terms on the right-hand side are constant for monochromatic light and a sample with fixed periodicity, the incidence and diffraction angles must change in opposite directions.

For better presentability, the incidence angles in Fig. 18 are specified in terms of $\theta_{i,x}$ and $\theta_{i,y}$ instead of the azimuthal and polar angles ϕ_i and θ_i shown in Fig. 16. The parameters of the sample used in Fig. 18 are chosen such that no diffraction orders are present for perpendicular incidence. It is obvious that the simulated data are self-consistent in the sense that the symmetries of the sample are also present in the FOURIER- and image-plane intensity distributions for each incidence angle. Furthermore, the diffraction orders change with the different incidence angles, as stated by the law of diffraction for a reflective grating in Eq. (68). Because of that, for sufficiently high incidence angles, some of the diffraction orders move into the

observable FOURIER plane and thus reveal some of the previously inaccessible structural information in the image plane. As one can see, the spatial resolution increases only in the direction in which the incidence angle is changed. For that reason, the main structural details become visible at $|\theta_{i,x}| = |\theta_{i,y}| = 30^\circ$, despite sub-diffraction lattice constants p_x and p_y .

Another interesting finding is that the maximum intensity in the image plane is enhanced for oblique incidence. This indicates that increasing the incidence angle facilitates the backscattering intensity.

C. Positional Disorder

Positional disorder describes the perturbation of the center position of each individual structure in the plasmonic metasurface. All metasurfaces shown in this section are generated using the disorder formalism introduced in Section 2.B.1. This comes with the great advantage that the performance of the CPDA model can be assessed without selection bias due to the randomized nature of the presented disorder formalism. Disorder strengths s_d and correlation lengths l_c are chosen as $s_d = m_s \cdot 100/3\%$ and $l_c = m_c \cdot 200\%$ with $m_s \in \{0, 1, 2, 3\}$ and $m_c \in \{0, 1, 2\}$, respectively. Since the correlation length has no influence on $s_d = 0\%$, only $l_c = 0\%$ is considered in that case, which yields the 10 different realizations shown in Fig. 19. It is important to mention that the size of the aluminum disks shown in Fig. 19 are to scale. This means that overlapping structures in this plot would indeed overlap in a real experimental system. The CPDA does not consider the extension of individual structures per definition and hence cannot predict the effects that originate from overlapping structures. This is particularly a problem at high disorder strengths, and low correlation lengths and can lead to severely overestimated scattering. The simulations discussed in this section are carried out for $n_x = n_y = 8$ aluminum disks with a diameter of $0.12 \mu\text{m}$, height of $0.06 \mu\text{m}$, and periodicities of $p_x = p_y = 0.5 \mu\text{m}$. The

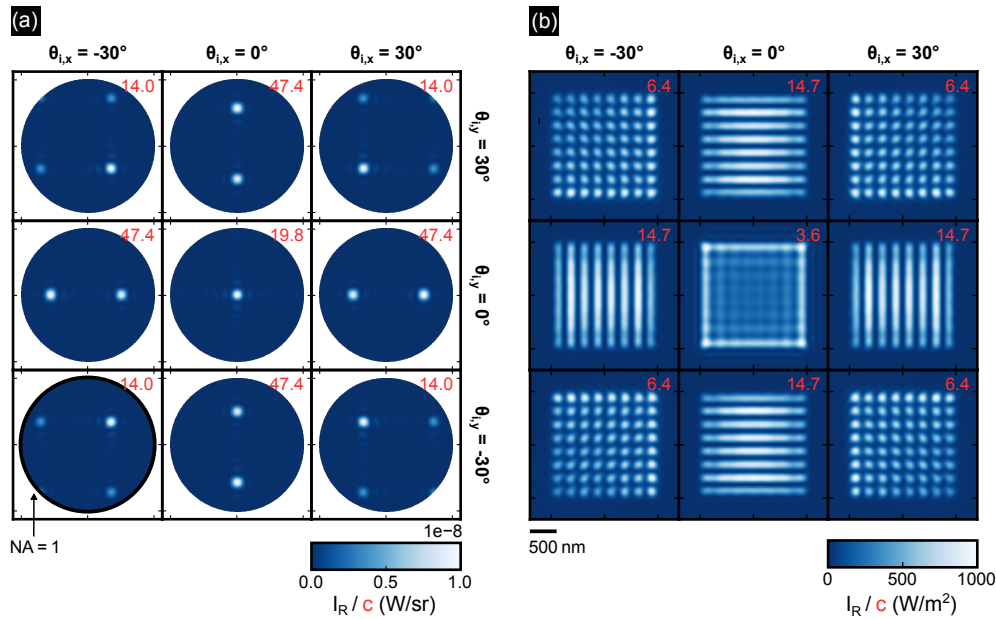


Fig. 18. Image and FOURIER planes for different incidence angles. The simulations were carried out for $NA = 1$, $\lambda_0 = 0.4 \mu\text{m}$, $n_x = n_y = 8$, $p_x = p_y = 0.25 \mu\text{m}$, and aluminum disks with size $0.12 \times 0.12 \times 0.06 \mu\text{m}^3$. According to the law of reflection, the diffraction orders move opposed to the incidence angle in (a). This shifts disks some of the diffraction orders into the captured FOURIER plane and consequently enhances the spatial resolution, as can be seen in (b).

image- and FOURIER-plane intensity distributions are evaluated at the vacuum wavelength of $\lambda_0 = 0.4 \mu\text{m}$.

Figure 19 shows that most of the disordered ensembles have decreased spatial intensities in comparison to the non-disordered case. Only at $s_d = 67\%$ and $s_d = 100\%$ with $l_c = 200\%$ does a single particle show enhanced emission. This indicates that the coupling with neighboring structures is beneficial in these cases. Nevertheless, the CPDA model predicts no enhanced emission or unreasonable intensities for the two overlapping structures at $s_d = 100\%$ and $l_c = 0\%$. Thus, strong emission cannot be reached by simply placing two structures in close vicinity. Besides that, the emission of the different structures gets much less homogeneous with increasing disorder in comparison to the periodic arrangement. This agrees with expectations, since the coupling is very different, depending on the structure distribution in the proximity of each structure. As described in previous sections, only structures with a spatial separation above the diffraction limit are distinguishable in the image plane. Especially at high disorder strengths and low correlation lengths, the intensity distributions of close structures overlap.

Since Eq. (53b) states that the intensity in the FOURIER plane depends on the product of the single particle radiation pattern and the SF, it is expected that the reciprocal intensities shown in Fig. 20 are dominated by the SF for unpolarized light. This means that the monochromatic intensity distributions resemble the SF and thus reveal information about the spatial frequencies and correlations that occur in that system. As expected, for the periodically arranged ensemble, only the first diffraction orders are visible in Fig. 20. Already at only $s_d = 33\%$ the maximum intensity significantly decreases by a factor of about three. For increasing disorder strengths and without correlation, the

diagonal (1,1) diffraction orders vanish first, until all diffraction orders are absent at $s_d = 100\%$. The isotropic angular scattering at such high disorder strengths indicates that no more lattice information is present in the metasurface and hence that the structure distribution approaches a truly random distribution. If correlation is introduced into the system, it is observed that the diffraction orders are more stable against perturbations and therefore persist even at very high disorder strengths. Since the diffraction orders are scattered around their original positions for strongly disordered but correlated perturbations, it can be concluded that the introduced correlation fosters the emergence of smaller subgrids with weakly varying orientations and periodicities.

D. Rotational Disorder

Rotational disorder affects the in-plane orientation of each structure within the metasurface. Mathematically speaking, the rotation is introduced by transforming the polarizability tensor $\hat{\alpha}$ into a rotated coordinate system. The rotation therefore affects only structures that have distinct polarizabilities α_{xx} and α_{yy} . Therefore, the metasurfaces presented in this section are based on rods instead of the disks in Sections 4.C and 4.E. Due to the C_2 symmetry of the rods, the disorder strength is limited to 50%, meaning that the maximum allowed rotation is $\pm 90^\circ$. The correlation lengths are chosen to be between 0% and 400%, as in Section 4.C. Besides that, the simulations were carried out for aluminum rods with size $0.12 \times 0.06 \times 0.06 \mu\text{m}^3$, $n_x = n_y = 8$, $p_x = p_y = 0.5 \mu\text{m}$, and $\lambda_0 = 0.4 \mu\text{m}$. For the sake of consistency with the other disorder types, the polarization state of incident light is kept unpolarized. The introduced correlation is most apparent for low disorder strengths. For higher disorder strengths, it gets increasingly difficult to spot the

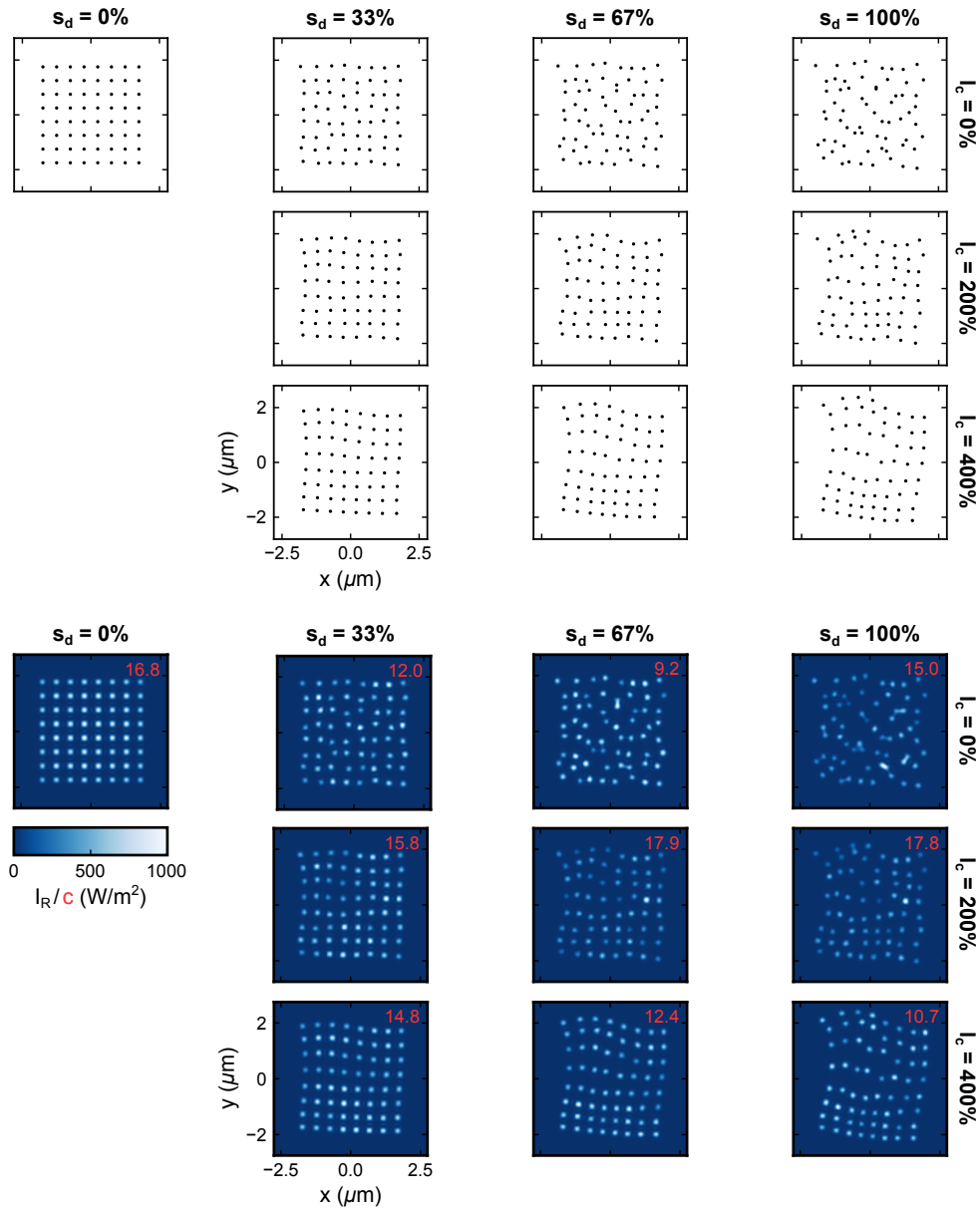


Fig. 19. Structure and image-plane plots for positional disorder. The seed of the pseudorandom number generator to create the positional disorder is zero. The associated simulations were carried out for $NA = 1$, $\lambda_0 = 0.4 \mu\text{m}$, $n_x = n_y = 8$, $p_x = p_y = 0.5 \mu\text{m}$, and aluminum disks with size $0.12 \times 0.12 \times 0.06 \mu\text{m}^3$. The structures are plotted to scale so that overlapping structures can be identified easily. This is particularly often the case for high disorder strengths and can cause inaccuracies in the CPDA, as the spatial extent of individual structures is not considered. Since the periodicity is above the diffraction limit, most individual structures can be identified. For the non-disordered case, the intensity at the dipole sites is almost uniform but decreases towards the borders. The uniformity of the intensities decreases with increasing disorder strengths, while the maximum intensity generally decreases for most combinations of disorder strengths and correlation lengths.

rotational correlation by eye. Unfortunately, no metrics have been found yet that allow one to quantify rotational disorder, so that the effects originating from correlation cannot be measured for the shown samples.

The most obvious finding for the image-plane data in Fig. 21 is that the intensities are actually enhanced for increasing rotational disorder. This suggests that the coupling between the structures is destructive in the unperturbed case and that the introduced perturbations weaken the near-field coupling and hence enhance the emission. Nevertheless, the spatial intensity

variations within a metasurface and also between different metasurfaces are very weak, which indicates that the coupling effects are rather negligible for unpolarized incidence.

This finding is similarly true for intensity distributions in the FOURIER plane shown in Fig. 22. Clearly, all angular radiation patterns are dominated by the effects of diffraction that arise from the periodic arrangement of rods. This is particularly interesting, since Eq. (53b) does not hold true anymore if the individual structures have different radiation patterns due

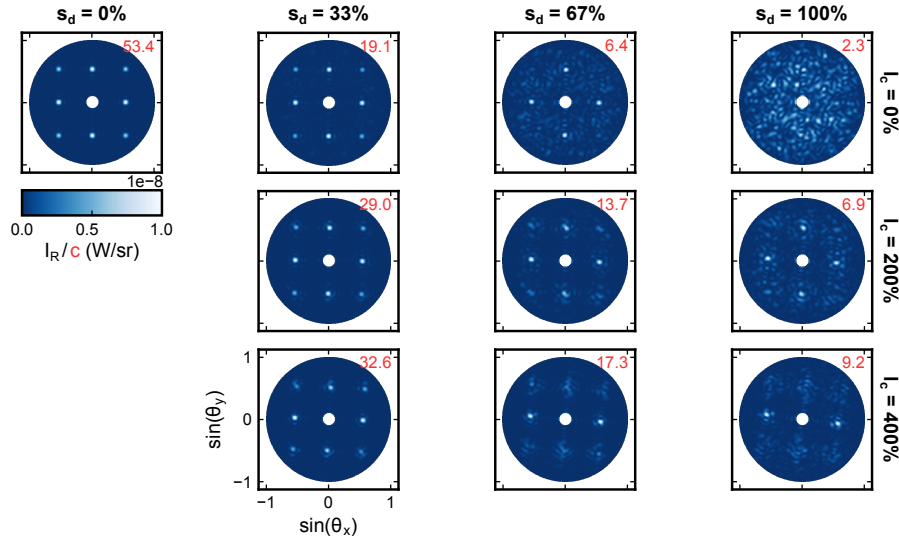


Fig. 20. FOURIER-plane plots for positional disorder. The seed of the pseudorandom number generator to create the positional disorder is zero. The simulations were carried out for $NA = 1$, $\lambda_0 = 0.4 \mu\text{m}$, $n_x = n_y = 8$, $p_x = p_y = 0.5 \mu\text{m}$, and aluminum disks with size $0.12 \times 0.12 \times 0.06 \mu\text{m}^3$. The (0,0) diffraction order is removed to increase the visibility of higher diffraction orders comprising the structural information. For $s_d = 0\%$ and $l_c = 0\%$, the (1,0), (0,1), and (1,1) diffraction orders are visible. In the uncorrelated case, the (1,1) diffraction orders have vanished at $s_d = 67\%$, whereas the (1,0) and (0,1) modes have disappeared at $s_d = 100\%$, which leads to highly isotropic scattering. Especially at intermediate disorder strengths and high correlation lengths, the diffraction orders are spread around the original locations, indicating the formation of several sub-gratings with varying periodicities and orientations.

to their distinct orientations. Therefore, it is actually necessary to describe the total radiation pattern of the metasurface with Eq. (52), which considers ensembles of non-uniform scatterers. However, the radiation patterns of the disordered surfaces strongly resemble the unperturbed case, which suggests that the field distribution of each individual scatterer is rather independent of its orientation for unpolarized incident fields.

This might lead to the false conclusion that rotational effects are not suitable for so called k -space engineering or tailored angular scattering. Indeed, in recent years, many metasurface designs have arisen that utilize sophisticated rotational arrangements to accomplish unique spectral and angular scattering properties [45,62–64]. This means that in contrast to the findings in this section, rotational disorder can indeed be used for k -space engineering, if the structure orientations and incident polarizations are chosen wisely. A good approach to design rotationally disordered metasurfaces can be derived from the generalized law of reflection [63,64]:

$$\sin(\theta_{i,x}) - \sin(\theta_x) = \frac{\lambda_0}{2\pi n} \cdot \frac{d\Phi}{dx}, \quad (69a)$$

$$\sin(\theta_{i,y}) - \sin(\theta_y) = \frac{\lambda_0}{2\pi n} \cdot \frac{d\Phi}{dy}. \quad (69b)$$

It states that reflection angles θ_x and θ_y can be manipulated not only by incidence angles $\theta_{i,x}$ and $\theta_{i,y}$, but also by in-plane phase gradients $d\Phi/dx$ and $d\Phi/dy$. Consequently, it is possible to control the reflection angles by engineering the orientation of individual structures and thereby manipulating the in-plane phase gradients. Yin *et al.* [45] have introduced a metasurface based on the latter principles and exhibits customizable beam

switching capabilities. These metasurfaces are discussed in Section 4.F.

E. Dimensional Disorder

The effects of size variations on individual particles can be estimated from the MIE theory for small spheres with radius R and dipolar resonances. It states that the scattering cross section is proportional to the squared volume V_p of that particle [65],

$$C_{sc} = \frac{8\pi}{3} k^4 R^6 \left(\left| \frac{\varepsilon_p - \varepsilon_e}{\varepsilon_p + 2\varepsilon_e} \right|^2 + \left| \frac{\mu_p - \mu_e}{\mu_p + 2\mu_e} \right|^2 \right) \propto V_p^2, \quad (70)$$

for constant permittivities and permeabilities ε_e , ε_p , μ_e , μ_p of the environment and particle, respectively. The second term of the scattering cross section can be neglected, since only metasurfaces with $\mu_p = \mu_e = 1$ are considered. Obviously, the structures shown in Fig. 23 are not spheres but disks instead. Nevertheless, we use Eq. (70) to justify the findings in this section, as there are generally no analytical solutions for the scattering cross section of arbitrarily shaped particles.

Similar to previous disorder types, the metasurfaces in this section consist of $n_x = n_y = 8$ aluminum disks with size $0.12 \times 0.12 \times 0.06 \mu\text{m}^3$ and periodicities $p_x = p_y = 0.5 \mu\text{m}$. The intensity distributions shown in Figs. 23 and 24 are evaluated for $\lambda_0 = 0.4 \mu\text{m}$. As stated in Section 2, only the particle diameter is affected by the dimensional disorder. The disorder strength is limited at $s_d = 50\%$ to avoid unreasonably small or even negative particle diameters. Since the volume of a disk

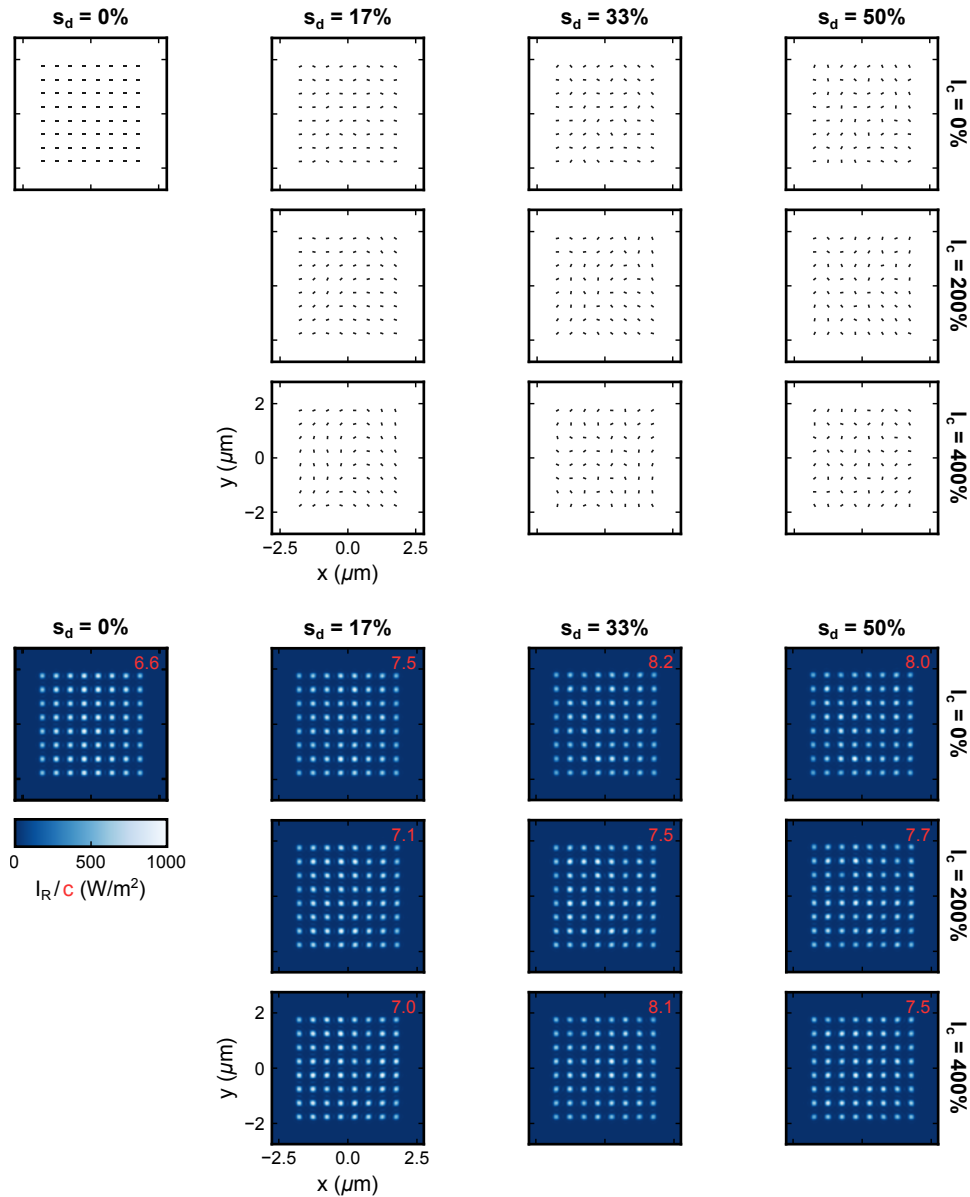


Fig. 21. Structure and image-plane plots for rotational disorder. The seed of the pseudorandom number generator to create the rotational disorder is zero. The associated simulations were carried out for $\text{NA} = 1$, $\lambda_0 = 0.4 \mu\text{m}$, $n_x = n_y = 8$, $p_x = p_y = 0.5 \mu\text{m}$, and aluminum rods with size $0.12 \times 0.06 \times 0.06 \mu\text{m}^3$. Because of the C_2 symmetry of the rods, the maximum disorder strength is limited to $s_d = 50\%$, which corresponds to a maximum rotation of $\pm 90^\circ$. The correlated disorder can be seen best for low disorder strengths and high correlation lengths. For any disorder strength and correlation length, the intensity distribution is very homogeneous. However, the maximum intensity is enhanced in the disordered cases in comparison to the unperturbed case. This indicates that the coupling of the dipoles is destructive, if all rods are aligned with each other.

scales with the square of the diameter, it is expected that the spatial intensity scales with the fourth power of its diameter.

In fact, Fig. 23 indicates that this scaling behavior is in good agreement with Eq. (70). For instance, at $s_d = 50\%$ and $l_c = 400\%$, the largest disks are approximately twice as large as in the unperturbed case, causing a $286.7/16.8 \approx 17\times$ enhanced emission. This is very close to the theoretically expected $16\times$ enhancement, especially regarding the distinct particle shape and the lack of coupling considerations in Eq. (70). The maximum intensity is enhanced for any disordered metasurface because the dimensional disorder always causes some disks to increase in diameter in the shown examples. Consequently, the

highest spatial intensity is predominantly determined by the size of the largest disk in the ensemble.

Similar to the findings for rotational disorder, the angular scattering behavior of the dimensionally disordered metasurfaces depicted in Fig. 23 is rather dominated by the periodic arrangement of the structures. However, the amplitude variations between the different FOURIER-plane intensities are significantly different between the various metasurfaces. In contrast to the image-plane intensities, the FOURIER-plane intensities are enhanced only by a factor of $150.3/53.4 \approx 3$ between the unperturbed surface and disordered surface at $s_d = 50\%$ and $l_c = 400\%$. This is primarily for two reasons.

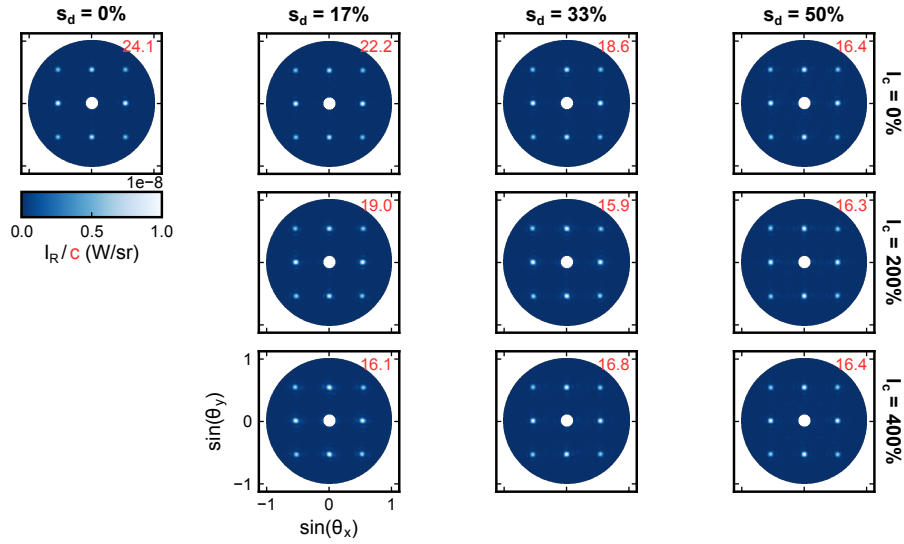


Fig. 22. FOURIER-plane plots for rotational disorder. The seed of the pseudorandom number generator to create the rotational disorder is zero. The simulations were carried out for $\text{NA} = 1$, $\lambda_0 = 0.4 \mu\text{m}$, $n_x = n_y = 8$, $p_x = p_y = 0.5 \mu\text{m}$, and aluminum rods with size $0.12 \times 0.06 \times 0.06 \mu\text{m}^3$. Because of the periodic arrangement of the dipole positions, the angular scattering looks very similar. Only the maximum intensity decreases by a factor of up to 1.5 due to the rotation of the dipoles.

First of all, the FOURIER-plane intensities correspond to the differential scattering cross section

$$\sigma_{\text{sc}}(\theta_x, \theta_y) = \frac{dC_{\text{sc}}}{d\Omega} \quad (71)$$

for 1 W/m^2 illumination intensity and thus must be integrated over all solid angles Ω . Second, integrating over all solid angles also considers the influence of smaller disks so that this would lead to an averaged scattering cross section C_{sc} . Therefore, the proper scaling of the simulation model cannot be derived from the data depicted in Fig. 24. However, in Section 5, the predicted volume scaling of the simulated scattering cross sections is proven to be consistent with Eq. (70).

F. Beam Switching

Yin *et al.* [45] have introduced a metasurface that allows one to switch the deflection angle of a circularly polarized beam. The presented metasurface comprises metallic rods stepwise rotated along the x axis, which causes a constant in-plane phase gradient. The rotation steps are chosen such that a full rotation from zero to π is accomplished within one super-period $P = n_s \cdot p$. In this notation, n_s refers to the number of structures within one super-period and $p = p_x = p_y$ to the spatial separation of the structures in x and y directions. The generalized law of reflection for this metasurface can thus be derived from Eq. (69) for perpendicular incidence:

$$\sin(\theta_x) = \frac{\lambda_0}{2\pi n} \cdot \frac{d\Phi}{dx} = \pm \frac{\lambda_0}{nP}, \quad (72a)$$

$$\sin(\theta_y) = -\frac{\lambda_0}{2\pi n} \cdot \frac{d\Phi}{dy} = 0. \quad (72b)$$

Obviously, the deflection angle θ_x only depends only on the wavelength $\lambda = \lambda_0/n$ of the incident field and super-period P .

To investigate the influence of the total number of structures, we introduce a third parameter n_p that indicates the number of super-periods of the metasurface.

Metasurfaces are designed such that the number of structures in both directions is given by $n_x = n_y = n_s \cdot n_p$. This provides the possibility to examine the influence of the interstructure distance p , number of structures within one super-period n_s , number of super-periods n_p , and thus, also the total number of particles $N = n_x \cdot n_y = (n_s \cdot n_p)^2$ independently.

The directivity

$$D(\theta, \phi) = 4\pi \frac{I_{\text{R}}(\theta, \phi)}{\int I_{\text{R}}(\theta, \phi) \sin(\theta) d\theta d\phi} \quad (73)$$

of the diffraction orders can be manipulated by changing the total number of structures N . However, the directivity actually depends on the size of the metasurface, which is proportional to N only if the interstructure distance p is constant. In the latter equation, the diffraction angles are defined in spherical coordinates with the polar angle $\theta = \arcsin(\sqrt{\sin^2(\theta_x) + \sin^2(\theta_y)})$ and azimuthal angle $\phi = \arctan(\sin(\theta_y)/\sin(\theta_x))$. Besides these coordinate transformations, the JACOBI determinant of the integral in the denominator must be adapted to the modified coordinate system.

Reducing the distance p between structures has essentially two effects. First of all, for constant n_s , the super-period P is equally decreased, which increases the angle of deflection. For the same reason, the angle of deflection stays unchanged if n_s and p are changed such that the super-period $P = n_s \cdot p$ stays unaffected.

The simulated data in Figs. 25(b) and 25(c) are based on the same type of metasurface for $n_s = n_p = 4$, $p_x = p_y = p = 0.3 \mu\text{m}$, and aluminum rods with size $0.12 \times 0.06 \times 0.06 \mu\text{m}^3$.

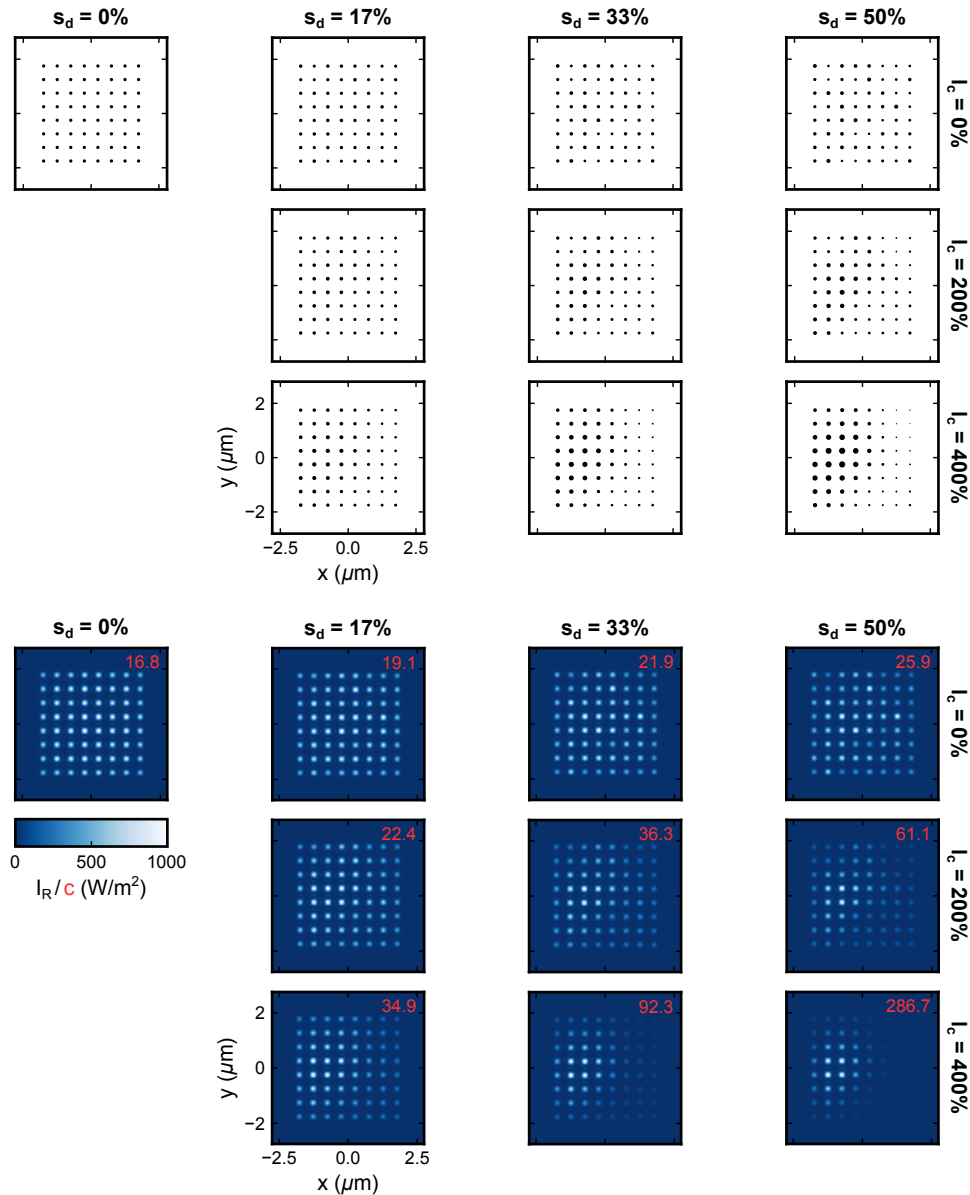


Fig. 23. Structure and image-plane plots for dimensional disorder. The seed of the pseudorandom number generator to create the dimensional disorder is zero. The associated simulations were carried out for $\text{NA} = 1$, $\lambda_0 = 0.4 \mu\text{m}$, $n_x = n_y = 8$, $p_x = p_y = 0.5 \mu\text{m}$, and aluminum disks with $0.12 \times 0.12 \times 0.06 \mu\text{m}^3$. The disorder strength is limited to $s_d = 50\%$ of the original size, so that unreasonably large or small diameters do not occur. Especially at high disorder strengths and correlation lengths, the size deviations are significant. The intensities are particularly strong at the locations of structures with large diameters. This finding is in good agreement with Mie theory, which states that the scattering cross section is proportional to the square of the particle volume.

As previously, the depicted FOURIER-plane intensities are evaluated at $\lambda_0 = 0.6 \mu\text{m}$, but in contrast to the previous simulation, an additional read-out polarization is specified. Yin *et al.* [45] have shown that the polarization of the deflected beam is changed from right-handed circularly polarized (RCP) to left-handed circularly polarized (LCP), if the beam is transmitted. However, in Fig. 25, the deflected beam keeps its polarization state. This originates from the fact that reflection at an interface reverses the handedness of circularly polarized light. For that reason, the light reflected into the zeroth order changes the polarization state from LCP to RCP or vice versa. We also find

that the sign of the deflection angle θ_x depends on the circular polarization state of the incident field. Consequently, both diffraction orders are present if the incident beam is unpolarized.

G. Structure Factor Approximation

The structure defined in Eq. (41) not only can be used to characterize disorder in metasurfaces, but also provides the possibility to predict FOURIER-plane intensity. Although Eq. (52) allows one to compute intensity distributions for arbitrary metasurfaces, we limit our discussion to surfaces with equal structures, so that the simplified formulation in Eq. (53b) applies. Piechulla

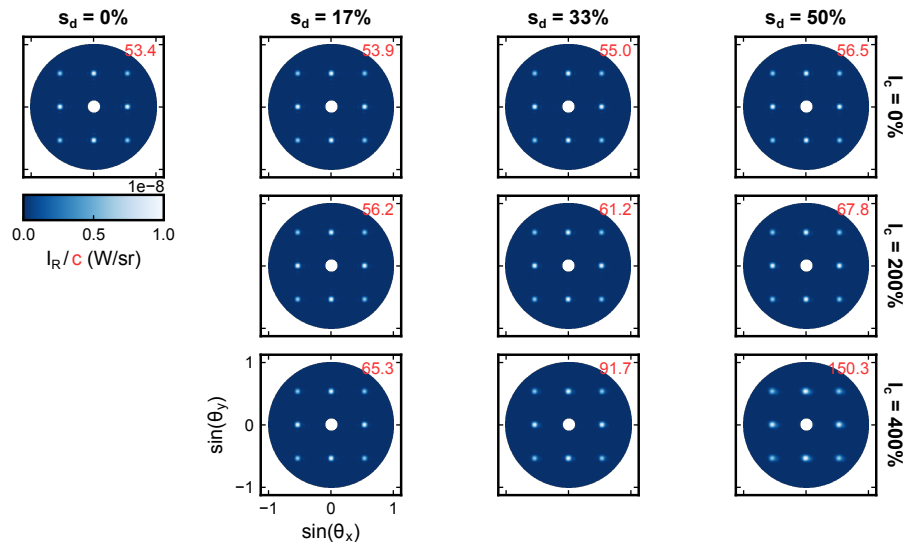


Fig. 24. FOURIER-plane plots for dimensional disorder. The seed of the pseudorandom number generator to create the dimensional disorder is zero. The simulations were carried out for $\text{NA} = 1$, $\lambda_0 = 0.4 \mu\text{m}$, $n_x = n_y = 8$, $p_x = p_y = 0.5 \mu\text{m}$, and aluminum disks with size $0.12 \times 0.12 \times 0.06 \mu\text{m}^3$. Similar to rotational disorder, the diffraction orders appear to be rather unaffected by the dimensional disorder. However, particularly at $s_d = 50\%$ and $l_c = 400\%$, the diffraction orders get blurry due to the strongly varying dipole sizes. Additionally, the angular backscattering is intensified as well, if the sample consists of many large disks with high scattering cross sections.

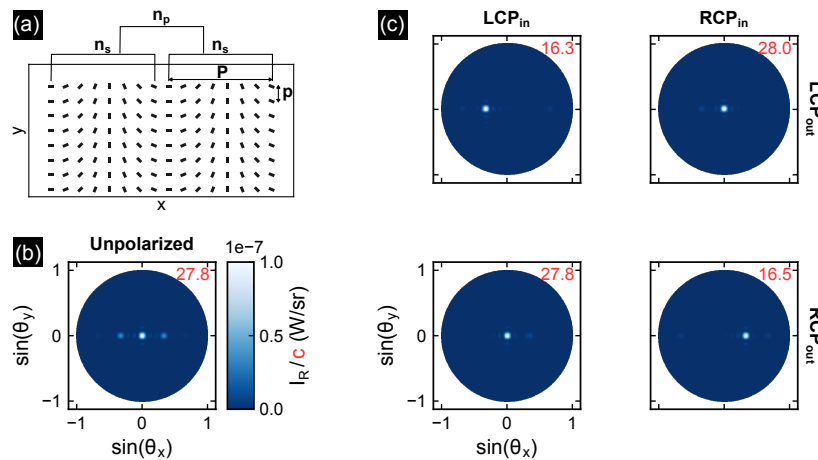


Fig. 25. Parameters and polarization dependence of the beam switching metasurface. (a) The beam switching is accomplished by metasurfaces that consist of metallic rods rotated around their center dependent on the position along the x axis. Since the distance between two neighboring rods is fixed at $p_x = p_y = p$, the diffraction angle is solely determined by the number of structures n_s within one of the n_p super-periods $P = n_s \cdot p$. All metasurfaces in this section have an equal number of structures in both directions $n_x = n_y = n_s \cdot n_p$. The simulations in (b) and (c) were carried out for $\lambda_0 = 0.6 \mu\text{m}$, $n_x = n_y = n_s \cdot n_p$, $n_s = n_p = 4$, $p_x = p_y = p = 0.3 \mu\text{m}$, and aluminum rods with size $0.12 \times 0.06 \times 0.06 \mu\text{m}^3$. (b) Both diffraction orders are present in the FOURIER plane for unpolarized illumination and no manipulation of the polarization state at the output. (c) Incident light with circular polarization is either diffracted or stays unaffected by the metasurface depending on the read-out polarization state at the output.

et al. [19,66] have discussed this approach in great detail for nearly hyperuniform metasurfaces that suppress long-range density fluctuations and thus promise to eliminate the zeroth order of the SF [67–69]. We refer to the approach derived from Eq. (53b) as structure factor approximation (SFA). As depicted in Fig. 26, the scattering amplitudes of individual aluminum rods are obtained from the CPDA approach for incident light polarized along the long axis of the rod. Since the SF does not depend on the shape of the individual structures, it is possible to separate the total response of the metasurface into contributions of the individual structures and the distributions of those.

Figure 26 vividly illustrates that the envelope of the total FOURIER-plane response is determined by the individual structures, while the integral subtleties arise due to the global structure distribution comprising the SF. This comes from the reciprocal relation of $\mathbf{r} = (x, y)^T$ and $\mathbf{q} = (q_x, q_y)^T$, which imposes an inverse relationship of the spatial extents in both spaces.

Figure 26 compares the SFA with the CPDA for the same structure distribution but different rod orientations. The polarization of incident light is always aligned with the orientation of aluminum rods. This means that the SF stays

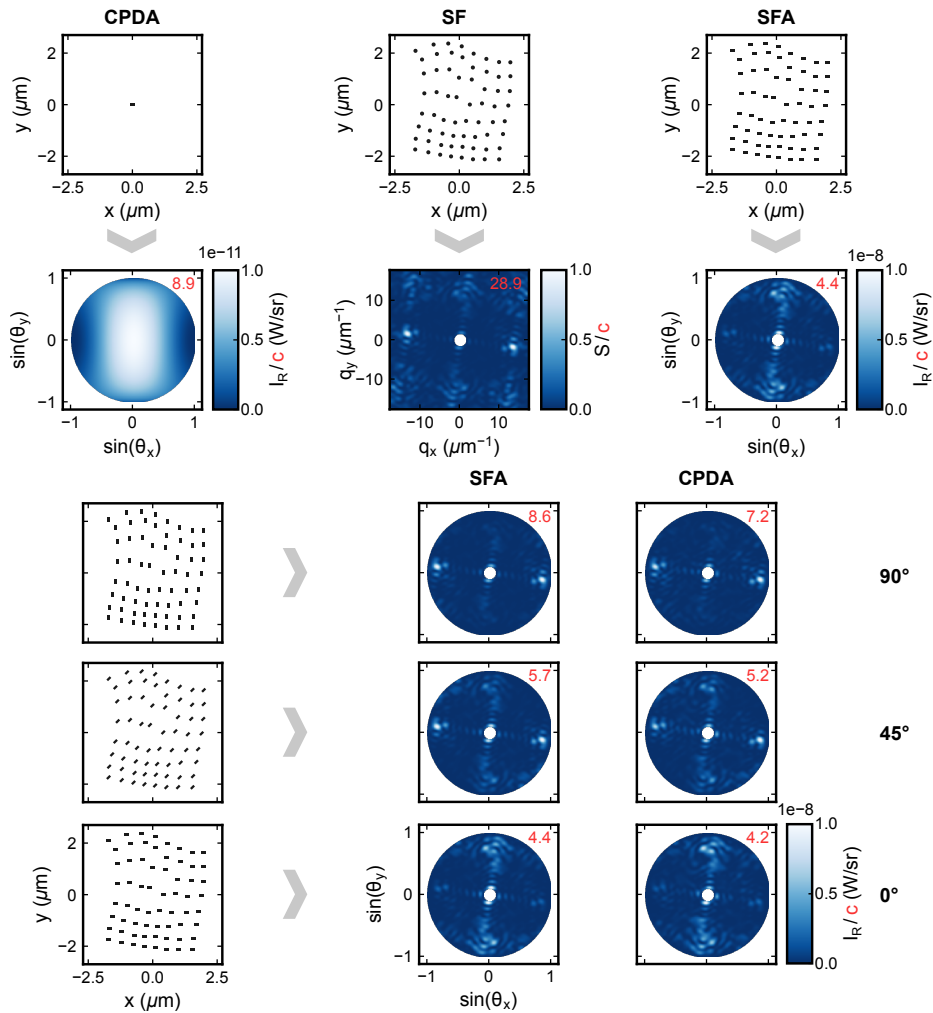


Fig. 26. Explanation of the structure factor approximation (SFA) (top) and comparison of the SFA and CPDA (bottom). The seed of the pseudorandom number generator to create the positional disorder is zero. The simulations were carried out for $\lambda_0 = 0.6 \mu\text{m}$, $n_x = n_y = 8$, $p_x = p_y = 0.5 \mu\text{m}$, $s_d = 100\%$, $l_c = 400\%$, and aluminum rods with size $0.18 \times 0.09 \times 0.06 \mu\text{m}^3$. The single particle intensity is computed for x -polarized light using the CPDA. Here, the structure factor (SF) does not consider the shape of individual particles and therefore returns only the spatial frequency distribution of the dipole positions. Since the sample consists of rods with equal polarizability, it is possible to compute the FOURIER-plane intensity distribution by multiplying the single particle intensity with the SF via the SFA. Note that the polarization of incident light is aligned with the rod orientation. As seen in the bottom panels, the agreement of the CPDA and SFA is very good and mainly differs in the maximum predicted intensities, which is slightly lower for the CPDA. This can be explained by the coupling between the dipoles, which is not considered in the SFA.

unaffected while the scattering amplitudes of the individual structures are altered corresponding to the rod orientation. Both computational approaches yield angular radiation patterns that resemble the SF with different regions of it being more or less pronounced depending on the orientation of the rods. Generally, the agreement of the SFA and CPDA is very good, with only very subtle differences. Figure 26 demonstrates that both models mainly differ in the maximum predicted intensities for which the CPDA predicts slightly lower values than the SFA. It is likely that this is due to the lack of coupling effects in the SFA, especially since Fig. 22 also indicates that the coupling induces weakened emission for aluminum disks and distances around $p_x = p_y = 0.5 \mu\text{m}$. Because of that, it is expected that the differences between the CPDA and SF are greater for metasurfaces in which coupling effects dominate. Although the SFA is not capable of considering the effects of coupling, it allows one

to compute the influence of higher order contributions such as quadrupolar modes, which is by definition not possible with the CPDA. Consequently, both approaches provide complementing features that are beneficial depending on the precise use case. Using both approaches also makes it possible to assess whether certain optical features arise due to strong coupling effects or dominant higher order modes in the metasurface.

H. Tailoring the Angular Scattering

In Section 2.C.1, we have discussed how phase-retrieval algorithms can be applied to solve the phase problem in lensless imaging. Although this is certainly interesting for various applications in the optical regime, this section assesses the applicability of phase-retrieval algorithms for tailored angular

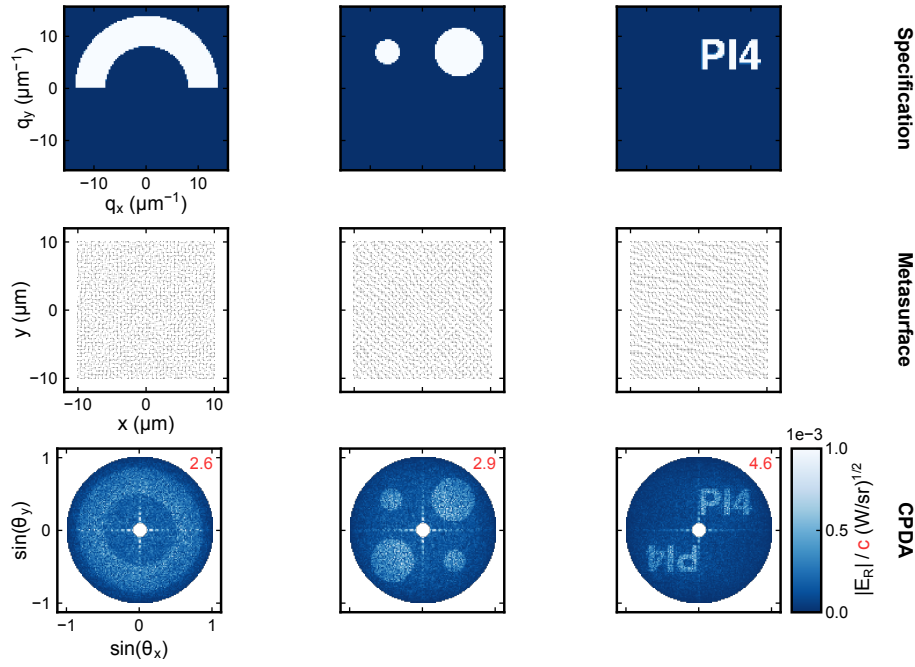


Fig. 27. Tailored FOURIER plane with phase randomized image-plane discretization. The simulations were carried out for $\lambda_0 = 0.6 \mu\text{m}$ and aluminum disks with size $0.12 \times 0.12 \times 0.06 \mu\text{m}^3$. The top row illustrates the specified binary FOURIER-plane amplitude distribution with uniformly randomized phase. The metasurfaces are obtained by placing disks at locations where the real parts of the field are positive. The CPDA simulations in the bottom row yield point-symmetric FOURIER-plane distributions.

radiation patterns. The latter is equivalent to specifying a certain intensity distribution in the FOURIER plane and finding the corresponding metasurface that generates this reciprocal intensity distribution. In principle, it is possible to solve this task by FOURIER transforming the desired intensity distribution. This is different from lensless imaging, since it is not important to find a unique solution to this problem, and thus the phase distribution in the FOURIER plane is not vital. However, it has shown to be beneficial to specify a random phase distribution before FOURIER transforming the desired FOURIER-plane fields. This is due to the fact that the FOURIER transform of an arbitrary FOURIER-plane amplitude distribution $\hat{E}_0(q_x, q_y)$,

$$E(x, y) = \mathcal{F}^{-1} \left[\hat{E}_0(q_x, q_y) \right], \quad (74)$$

often yields a discontinuous field distribution $E(x, y)$ that cannot be reproduced with sensible structure distributions. Introducing a uniformly distributed random phase $\varphi(q_x, q_y)$ convolutes the original field distribution $E(x, y)$ with the FOURIER transform of that random phase:

$$\begin{aligned} E'(x, y) &= \mathcal{F}^{-1} \left[\hat{E}_0(q_x, q_y) \cdot e^{i\varphi(q_x, q_y)} \right] \\ &= E(x, y) * \mathcal{F}^{-1} \left[e^{i\varphi(q_x, q_y)} \right]. \end{aligned} \quad (75)$$

The FOURIER transform of the uniformly distributed random phase results in a complex valued random distribution in the image plane. Because of that, the convolution can be understood in terms of a moving average filter of that random distribution with a window function $E(x, y)$, which generally yields a smoother field distribution $E'(x, y)$.

A smooth field distribution is often beneficial, if the field distribution has to be converted into a producible metasurface design. Because of that, introducing a random phase in the FOURIER plane is recommended as a heuristic principle. A very simple but effective way to convert the obtained field distribution $E'(x, y)$ into a metasurface is to threshold the fields such that structures are placed at locations where the real part of the electric field is positive ($\mathcal{R}[E'(x, y)] > 0$). As illustrated in Fig. 27, only point-symmetric field distributions can be obtained with this simple approach, as the imaginary part of the field distribution is neglected.

A more sophisticated approach to design the angular scattering of metasurfaces is provided by the phase-retrieval algorithms introduced in Section 2.C.1. Since the presented algorithms are iterative, it is usually straightforward to specify further constraints that the metasurfaces must fulfill. For example, the phase-retrieval algorithms intrinsically allow one to target a certain metasurface extent by specifying the size of the support region S accordingly. Zhao *et al.* [26] have realized a holographic display that can be multiplexed by changing the polarization state of incident light. The presented metasurfaces were designed by modifying the GS algorithm such that the polarization dependence can be incorporated using the JONES calculus. Zheng *et al.* [70] accomplished sophisticated field distributions with very high diffraction efficiencies and broad bandwidth by using the GS algorithm, but optimizing only for circularly polarized light. The general idea behind employing phase-retrieval algorithms to tailor the FOURIER plane is depicted in Fig. 28. Here, it is assumed that an unknown metasurface generates the specified FOURIER-plane intensity distribution. Phase-retrieval algorithms can be used to find the

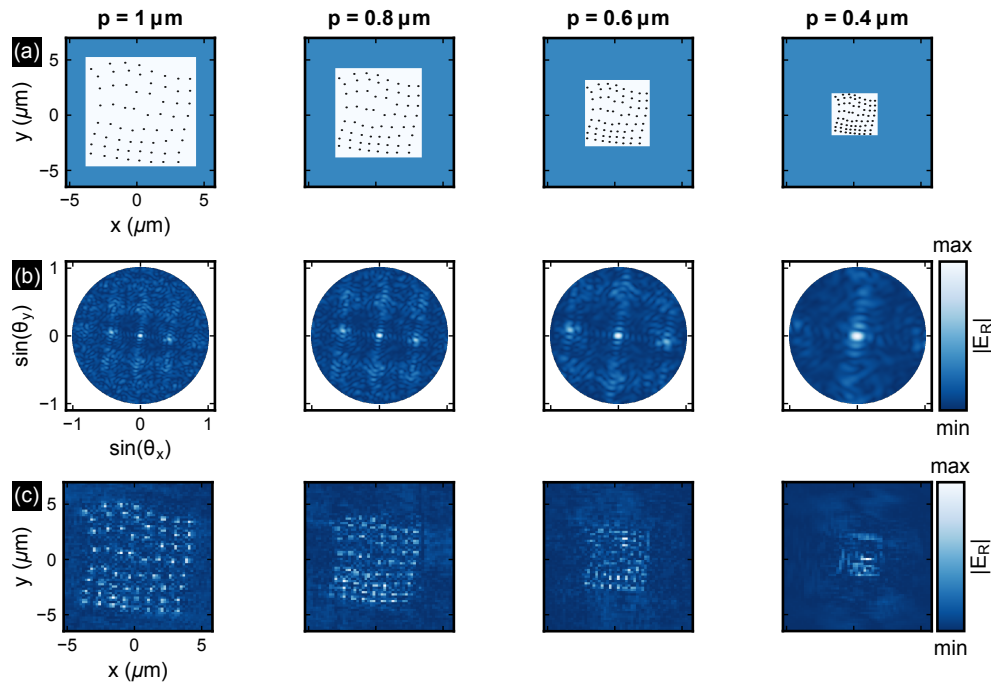


Fig. 28. Recovery of the image-plane fields via phase-retrieval algorithms. The seed of the pseudorandom number generator to create the positional disorder is zero. The simulations were carried out for $\lambda_0 = 0.4 \mu\text{m}$, $n_x = n_y = 8$, $p_x = p_y = p$, $s_d = 100\%$, $l_c = 400\%$, and aluminum disks with size $0.18 \times 0.18 \times 0.06 \mu\text{m}^3$. (a) The metasurfaces differ in their initial periodicity $p = p_x = p_y$ and generate the FOURIER-plane amplitudes depicted in (b). The oversampling smoothness (OSS) algorithm retrieves the image-plane field distributions (only amplitudes are shown) (c) from the specified FOURIER-plane amplitudes (b) and the support region indicated by the white background in (a).

image-plane field distribution that corresponds to the desired FOURIER-plane pattern. Due to the SHANNON–NYQUIST sampling theorem, the phase-retrieval algorithm returns a complex valued image with a pixel pitch half the wavelength of incident light. Figure 28(c) reveals that the retrieved image is in very good agreement with the actual metasurface as long as the structural details of the sample are above the diffraction limit. Finally, the metasurface can be generated by distributing custom structures that comply with the amplitude and phase of the retrieved image-plane field distribution at each pixel. Although this has not been shown yet, the CPDA model is a promising tool for improving the design quality of metasurfaces, as it allows one to efficiently compute the FOURIER-plane response of extended metasurfaces under consideration of coupling effects, various input polarization states, or even structural perturbations.

5. MODEL VALIDATION

While the previous section gave an overview on the capabilities of the CPDA model, the goal of this section is to validate the model by comparing the computed results with external software, theoretical predictions, and experiments. Validating the results against three different sources allows one to take advantage of the strengths of each. First, we will compare the spectrally resolved scattering cross section of a single gold disk predicted by the CPDA model with MIE theory. This is particularly useful, as MIE theory provides an analytical solution for a well-defined problem. Subsequently, a slightly more difficult case of coupled gold dimers is considered. Here, the differential scattering cross

section σ_{sc} at $\theta_x = \theta_y = 0$ is compared with COMSOL simulations. The primary aim of this step is to assess the normalization and accuracy of the coupling model (see Section 2.A.1) of the CPDA. Then, we validate the image-plane, FOURIER-plane, and spectral intensity distributions of largely extended and non-trivial metasurface designs with experimental data. Since no comparable simulational approaches are available that allow one to compute the response of disordered and extended samples with reasonable computational effort, these results cannot be validated using external software.

A. Validation against Mie Theory

MIE theory describes the scattering of electromagnetic waves at spherical objects. The scattering cross section

$$C_{sc} = \frac{P_{sc}}{I_{inc}}, \quad (76)$$

which is predicted by MIE theory for spherical particles and dipolar resonances, is given in Eq. (70) for small particles. The scattering cross section defines the power P_{sc} scattered by a particle if a plane wave with intensity I_{inc} impinges on that particle. The formula in Eq. (70) derived from MIE theory can also be expressed in terms of the polarizability α [65]:

$$C_{sc} = \frac{k^4}{6\pi} |\alpha|^2. \quad (77)$$

Strictly speaking, this relation applies only to spherical objects. Nevertheless, we will assume that it also holds true

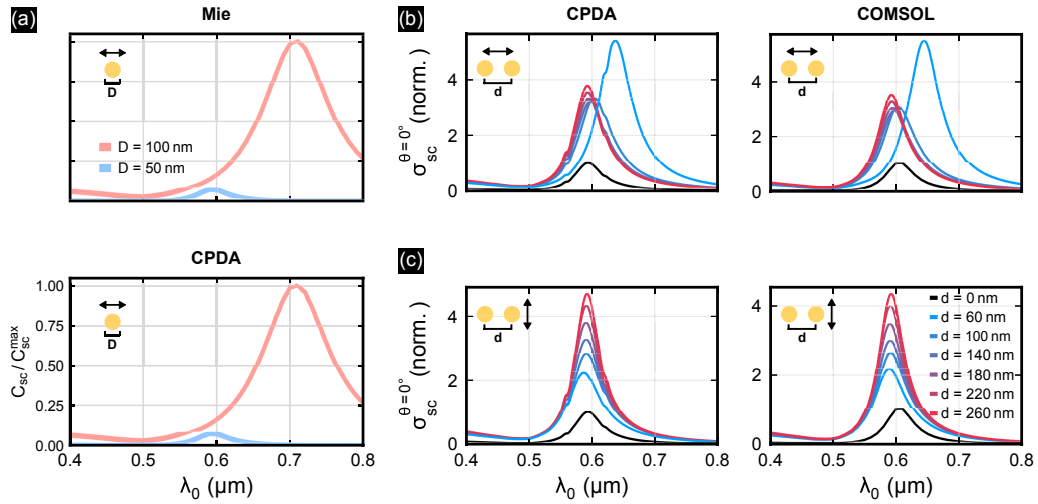


Fig. 29. Validation of the spectral scattering cross sections. (a) The simulations were carried out for a single gold disk with diameter D and shape $D \times D \times 0.03 \mu\text{m}^3$. The normalized scattering cross sections C_{sc} from the CPDA model are in excellent agreement with MIE theory. This indicates that the slight differences in the resonance position of the single particle references in (b) and (c) are due to higher order modes. The simulations in (b) and (c) were carried out for two gold disks with center-to-center distance d and shape $0.05 \times 0.05 \times 0.03 \mu\text{m}^3$. The differential scattering cross section σ_{sc} of a single gold disk with the same shape is provided as reference ($d = 0$ nm). All spectra in (b) and (c) are provided for specular reflection at $\theta_x = \theta_y = 0^\circ$. (b) If incident light is aligned along the dimer axis, the relative amplitudes, resonance widths, and resonance wavelengths agree well with COMSOL simulations. The findings are very similar if the incident light is polarized perpendicular to the structure axis in (c). The dimer differential scattering cross-section spectra are normalized to the amplitude of the single particle spectrum.

for other shapes such as disks. Thus, we imply that all effects emerging from the altered particle shape are contained within the polarizability.

Figure 29(a) compares the backward scattering cross section of the CPDA model with MIE theory. The scattering cross section of the CPDA model is derived from the FOURIER-plane intensity distribution $I_R(\theta_x, \theta_y)$ and Eq. (76) as

$$C_{sc} = \frac{\int I_R(\theta_x, \theta_y) d\Omega}{I_{inc}} \quad (78)$$

for $I_{inc} = 1 \text{ W/m}^2$, while the MIE scattering cross section is computed with Eq. (77). The results shown in Fig. 29(a) are normalized to the maximum scattering cross section C_{sc}^{max} so that the line shape and scaling are emphasized. It is important to point out that both models rely on the same polarizabilities α acquired from COMSOL simulations. For the depicted results, only x -polarized incident and scattered light is considered, meaning that the MIE scattering cross sections are computed from the α_{xx} component of the polarizability tensor. The investigated system consists of a single gold disk with varying diameter D and a height of $0.03 \mu\text{m}$. Both approaches predict much stronger scattering for the disk with $D = 0.1 \mu\text{m}$, which is consistent with Eq. (70). The line shapes exhibit excellent agreement with each other, with no visible differences between both approaches. This is also true for the predicted scaling of the maximum scattering cross section between the disk with $D = 0.1 \mu\text{m}$ and $D = 0.05 \mu\text{m}$.

B. Validation against COMSOL

In the next step, we validate the CPDA model against COMSOL simulations for a slightly more difficult system

of two gold disks with varying center-to-center distance d . Even so, the differential scattering cross section of a single disk is considered as reference. In contrast to the previous section, the differential scattering cross section σ_{sc} instead of the scattering cross section C_{sc} is considered. Both quantities relate to each other as

$$\sigma_{sc}(\theta_x, \theta_y) = \frac{dC_{sc}}{d\Omega}, \quad (79)$$

so that the differential scattering cross section is obtained from the CPDA model as

$$\sigma_{sc}(\theta_x, \theta_y) = \frac{I_R(\theta_x, \theta_y)}{I_{inc}}. \quad (80)$$

As indicated by the y -labels in Figs. 29(b) and 29(c), only the differential scattering cross section in backwards direction ($\theta_x = \theta_y = \theta = 0^\circ$) is considered. In Fig. 29(b), the polarization state of incident light is aligned with the dimer. Here, COMSOL simulations reveal that the resonance amplitudes and wavelengths scale highly nonlinearly with the center-to-center distance d . Nevertheless, the CPDA model accomplishes precisely rendering this behavior of line shapes. This is particularly remarkable, as the CPDA model does not consider any extent or shape of the structure, and the edge-to-edge distance for $d = 60$ nm is only 10 nm. Two minor differences can be found between the models. First of all, the CPDA simulations exhibit sharp features around the resonance positions, which are not present in the COMSOL simulations. It is likely that this is due to numerical errors introduced during the inversion of the transfer matrix \hat{T}_M from Eq. (17), because \hat{T}_M may become ill conditioned if resonances with small linewidths are present. Second, the single gold disk provided as references is slightly blueshifted in comparison to the COMSOL results. The good

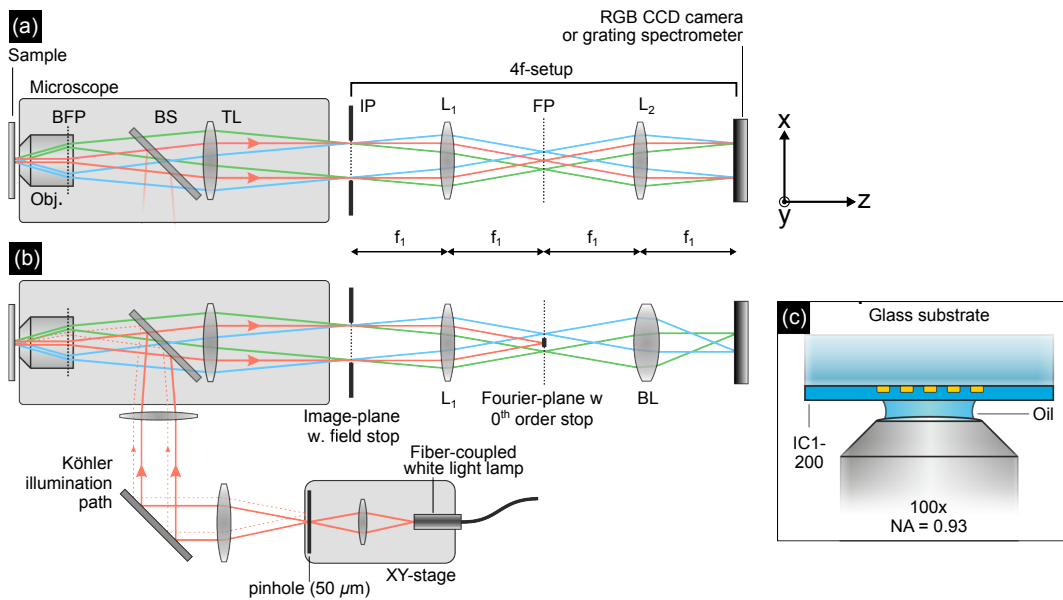


Fig. 30. Schematic of the experimental setup. (a) The setup used to capture the image-plane appearance consists of an objective with a tube lens and subsequent $4f$ setup that projects the sample onto the RGB CCD camera. (b) To capture the FOURIER plane instead of the image plane, the lens L_2 is replaced by a BERTRAND lens that images the FOURIER plane within the $4f$ setup onto the CCD camera. In both setups (a) and (b), the sample is illuminated using KÖHLER illumination and a white light lamp, which is coupled into the setup with a beam splitter. The XY stage enables to change the incidence angle of the illuminating light on the sample. (c) The metasurfaces are attached to a glass substrate and embedded within the IC1-200 dielectric ($n = 1.41$) to approximate a homogeneous refractive index of $n = 1.5$. An oil-immersion objective with a normalized NA of 0.93, $n_{\text{oil}} = 1.518$ and $100\times$ magnification is used. Spectral data are recorded by replacing the RGB CCD camera with a grating spectrometer. The figure has been adapted from Ref. [16] and depicts the same optical setup. BFP, back focal plane; BS, beam splitter; TL, tube lens; IP, image plane; FP, FOURIER plane; BL, BERTRAND lens.

agreement of the CPDA approach with MIE theory for the same scenario suggests that the differences are due to higher order modes, which are considered in COMSOL.

In Fig. 29(c), the same dimers are shown for perpendicular polarization of the incident beam. The findings are very similar and generally reveal very good qualitative agreement between the CPDA and COMSOL simulations. In this case, less variation of the resonance position is observed. This is due to the excitation polarization, which is perpendicular to the dimer axis and thus weakens the near-field coupling between disks. As before, the CPDA simulations exhibit sharp features around the resonance positions and also the single particle reference simulation is blueshifted in comparison to the COMSOL results.

C. Validation against Experiments

Although any simulation model must ultimately resemble the experimental reality, it is often difficult to use experimental data as ground truth for the validation. This comes from the fact that experiments involve plenty of parts that possess properties that are far from ideal. Many of such properties can be compensated for within the experiment or considered in the simulation model, but there will always remain experimental circumstances that are not included in the model. Such experimental circumstances can be the nonlinear response of the detecting camera, absorption losses and dispersion in the optical components, wavefront errors due to aberrations, and scattering at dust particles in the optical setup, among others. For the experimental

setup used in this section, special care had to be taken to embed the metasurface in a constant refractive index environment. Furthermore, matching the color model from Section 2.D to the color model of the CCD RGB camera was a particularly challenging task. Nevertheless, there were no other computational approaches available that allow one to compute the response of plasmonic metasurfaces comprising several thousands of individual structures with reasonable computational effort, so that an experimental validation is the only remaining option.

Figure 30 depicts a sketch of the experimental setup used to acquire the FOURIER- and image-plane intensities as well as the spectrally resolved reflectances. Figure 30(c) illustrates that the metasurfaces, attached to a glass substrate, are covered with IC1-200 dielectric and connected to the objective by an immersion oil to mimic a constant refractive index of $n = 1.5$. The objective has a material independent NA of 0.93, so that very high resolutions can be accomplished. KÖHLER illumination is used for the illumination path to ensure uniform illumination of the sample and enable the independent manipulation of the field and aperture stops. The illumination beam is generated by a spectrally flat laser-driven light source (Energetic EQ99) and coupled into the microscopy setup by a beam splitter located between the objective and tube lens. The imaging path consists of the objective and a tube lens with a subsequent $4f$ system, which projects the intermediate image plane on the RGB CCD camera (Allied Vision Prosilica GC2450) or a grating spectrometer (Princeton Instruments Pixis 256 camera with Princeton Instruments SP-2500i monochromator). The latter depends on whether spatially or spectrally resolved measurements are

conducted. The spectral measurements are recorded along an approximately one-dimensional slice in the FOURIER or image plane so that spatial information can be captured simultaneously. However, this involves considerably more effort to scan both spatial dimensions. To record the FOURIER plane, the L_2 lens in the $4f$ setup is replaced by a BERTRAND lens, which projects the intermediate FOURIER plane onto the RGB CCD camera or grating spectrometer, respectively. For such measurements a zeroth order stop can be assembled in the intermediate FOURIER plane, as illustrated in Fig. 30(b).

The fabrication steps of the metasurfaces used for the experimental validation are as follows. First, a positive resist

is spin-coated followed by electron beam lithography to define the structure distribution. After developing the resist, the aluminum is deposited onto the substrate with electron beam evaporation. A N-ethyl pyrrolidone (NEP)-based liftoff process removes the residual resist. Eventually, the remaining aluminum nanostructures are spin-coated with IC1-200 to approximate a constant refractive index of $n = 1.5$.

The following description applies to all data depicted in Figs. 31–34. The simulated image- and FOURIER-plane appearances are derived from hyperspectral simulations in the wavelength range of $0.38 \mu\text{m} \leq \lambda_0 \leq 0.8 \mu\text{m}$ so that all perceivable wavelengths are covered. This means that each pixel

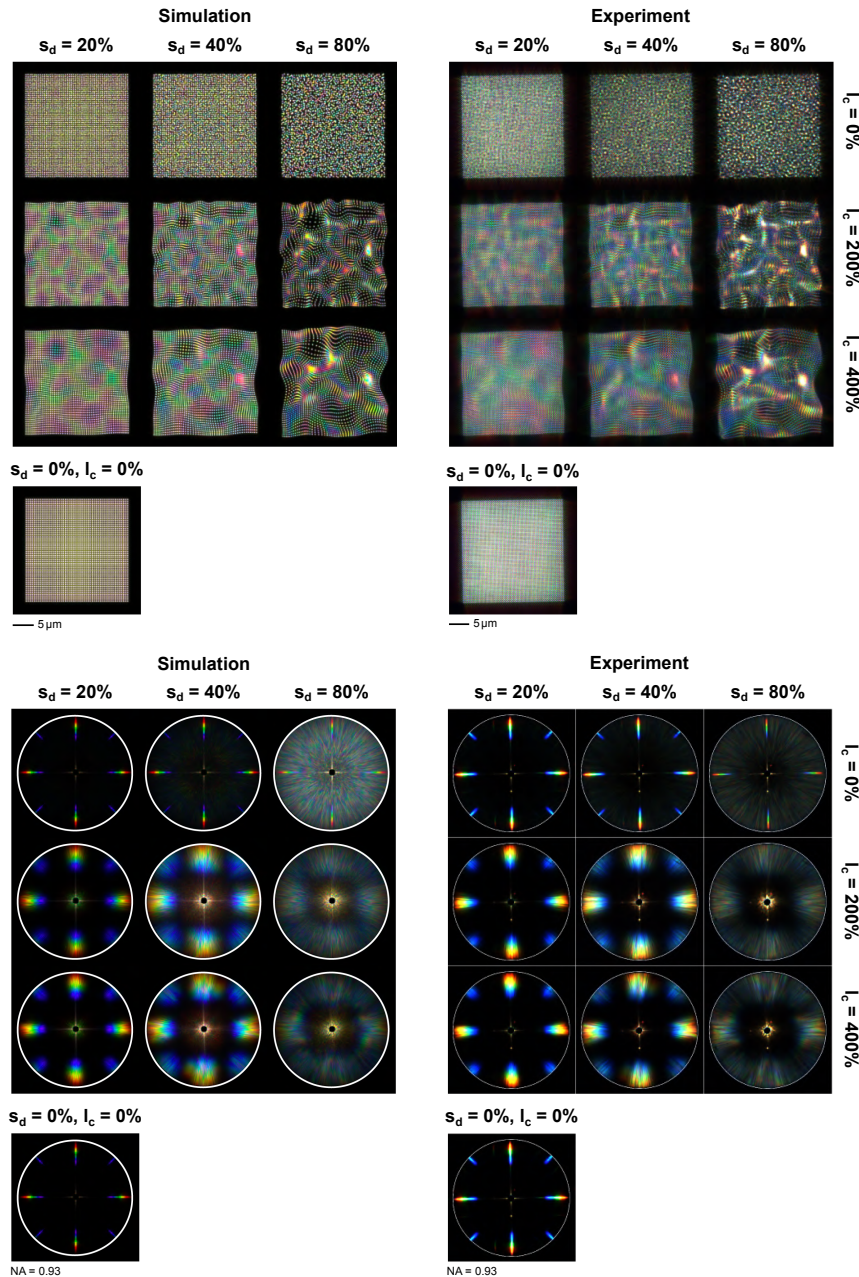


Fig. 31. Experimental validation of the image-plane and FOURIER-plane appearances at $0.5 \mu\text{m}$ periodicity. The seed of the pseudorandom number generator to create the positional disorder is zero. The corresponding metasurfaces consist of $n_x = n_y = 50$ aluminum disks with size $0.12 \times 0.12 \times 0.06 \mu\text{m}^3$. The simulated appearances are derived from the hyperspectral datasets using the color model explained in Section 2.D. The luminosities of the simulations and measurements are matched to render the same visual impression. These results are published in Ref. [16].

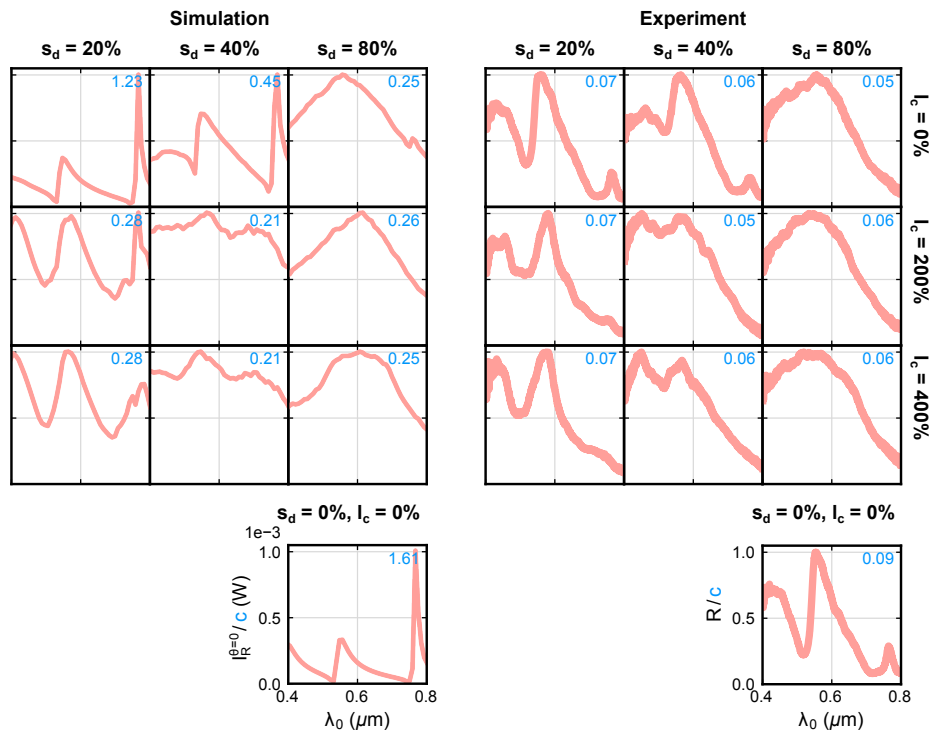


Fig. 32. Same as in Fig. 31, but for spectral reflectance. It is important to mention that the simulated and experimental data do not show precisely the same spectral quantities.

in the image or FOURIER plane has an underlying spectrum, which is converted to the sRGB color space with the color model explained in Section 2.D. The simulation NA is matched with the NA of the objective for better comparability. The white balance of the experimental data is adjusted with a reference aluminum mirror, and all depicted images are background corrected by subtracting an image without a sample from the recorded image of interest. This method of correcting the background is inaccurate but assumed to be sufficient. Both the simulated and experimental appearances have been adjusted in brightness to match the visual impression and bring out all relevant features. The simulated spectra are taken from the zeroth order in the FOURIER plane, while the experimental spectra are acquired from reflectance measurements across a central slice of the sample. This difference causes many uncertainties, which is why the spectral data have to be taken with care. An approach that provides better comparability of the spectral data is discussed in Section 6.

The first set of measurements was performed for a super-diffraction grating with $p_x = p_y = 0.5 \mu\text{m}$ and $n_x = n_y = 50$ aluminum disks with size $0.12 \times 0.12 \times 0.06 \mu\text{m}^3$. The disorder parameter sets are $s_d \in \{0\%, 20\%, 40\%, 80\%\}$ and $l_c \in \{0\%, 200\%, 400\%\}$, whereas only $l_c = 0\%$ is considered for $s_d = 0\%$, yielding 10 different realizations.

Figure 31 shows at the top the computationally and experimentally acquired image-plane appearances for different disorder parameters. Generally, the agreement is very good. A slight mismatch in the tone of the simulated appearances can be observed. In comparison to the experimental data, a warmer and more purple tint is present. The differences are particularly present at low disorder strengths. This indicates that the

mismatch arises from structural perturbations introduced in the manufacturing process and not considered in the simulation model. These unwanted perturbations get increasingly negligible with growing disorder strength, which leads to better agreement between simulations and measurements. The accuracy of the predicted appearances gets particularly obvious for high disorder strengths and correlation lengths. For these metasurfaces, almost all spatial features are predicted precisely in their extension, hue, and luminosity.

The FOURIER-plane appearances are depicted in Fig. 31 at the bottom. Again we find very good agreement between simulations and measurements. The radiation pattern of the simulated and non-disordered metasurface exhibits purple features at the inner edges of the diffraction orders. These features are not present in the measurements and thus suggest that certain spectral regions are overestimated in the simulations. Possible reasons are additional structural defects in the measured metasurfaces, oxidation of the aluminum disks, absorption losses in the optical components, or strong higher order moments not considered in the CPDA model. Besides these purple features, we find that the isotropic scattering that emerges at high disorder strengths is overestimated by the simulations. However, the simulations correctly predict that the (1,0) and (0,1) diffraction orders are still present at $s_d = 80\%$ and $l_c = 0\%$, while the (1,1) orders have vanished. Another observation that is true for most of the presented appearances is that weakly pronounced characteristics are less visible in the measurements. A possible reason for this is that the RGB camera can record a maximum of 12 bit, while the simulation model performs the calculations with 64 bit. The higher bit depth allows one to distinguish

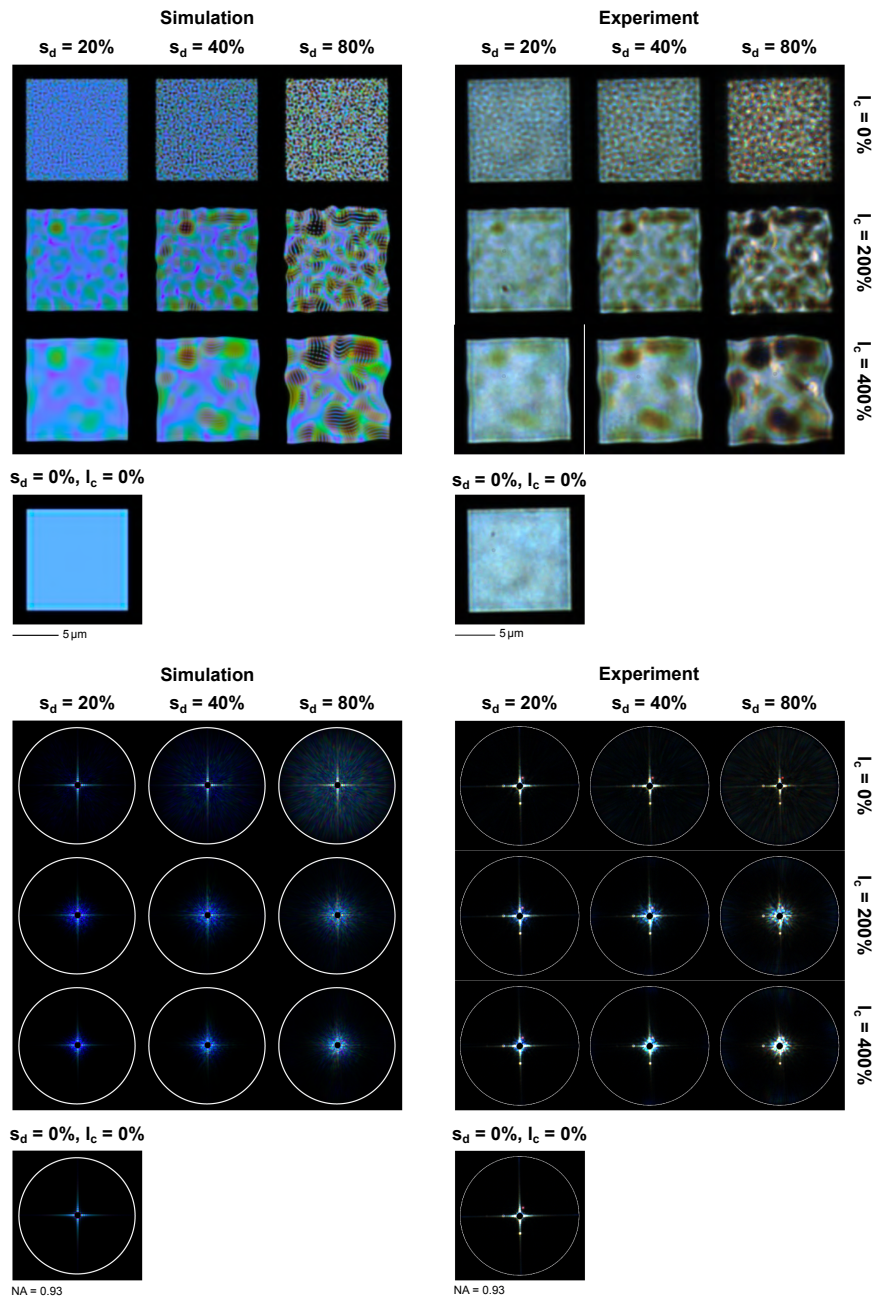


Fig. 33. Same as in Fig. 31, but for a periodicity of $0.25 \mu\text{m}$. These results are partially published in [16].

dark features much longer from an actually black pixel and thus facilitates their visibility.

Before discussing the spectral data shown in Fig. 32, it must be stressed again that the simulations and measurements do not show precisely the same quantities. The simulated intensities are acquired from the intensities in zeroth order of the FOURIER plane, while the measurements correspond to the reflectance along a central slice of the metasurface. Thus, perfectly matching results cannot be expected from the outset, and the results must be taken with care. The most obvious difference between the measurements and simulations is that the simulations overestimate the peak that occurs close to $\lambda_0 = 0.8 \mu\text{m}$ for low to intermediate disorder strengths. This

certainly contributes to the deviations in the predicted appearances to some extent. However, it is questionable how strong the influence of this spectral feature on the appearance actually is, since human perception ends at $0.78 \mu\text{m}$ and is very weak just below. The measurements generally exhibit a stronger decay towards longer wavelengths in comparison to simulations. Besides that, we often find good agreement between the relative heights and spectral positions of the computed and measured peaks.

The second set of measurements was performed for a sub-diffraction grating with $p_x = p_y = 0.25 \mu\text{m}$ and $n_x = n_y = 50$ aluminum disks with size $0.12 \times 0.12 \times 0.06 \mu\text{m}^3$. The disorder parameter sets are $s_d \in \{0\%, 20\%, 40\%, 80\%\}$ and

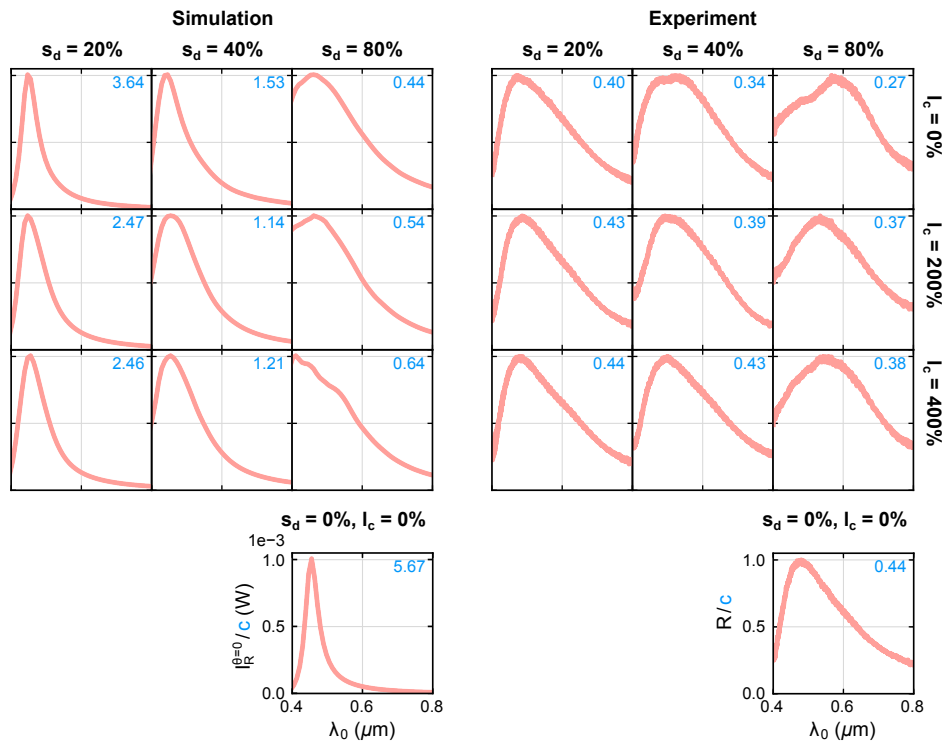


Fig. 34. Same as in Fig. 32, but for the spectral reflectance at 0.25 μm periodicity.

$l_c \in \{0\%, 200\%, 400\%\}$, whereas only $l_c = 0\%$ is considered for $s_d = 0\%$, yielding again 10 different realizations.

Figure 33 displays at the top the image-plane appearance of sub-diffraction metasurfaces. The agreement between simulation and measurement is particularly good for the non-disordered case. Both show very similar appearances and exhibit several edge modes with purple and cyan tint. However, effects of a non-uniform illumination, possibly due to pollution of some optical elements, are visible in the measured image-plane appearances, which are additional sources of disturbances not considered in the simulation model. Similar to the super-diffraction metasurfaces, the appearances of the simulated data are shifted towards the purple tones. Furthermore, dark features are again much less pronounced in the measurements, which is presumably caused by the lower bit depth of the RGB camera. Besides that, very good predictive power of the CPDA model is observed. The occurrence of the green areas is accurately reproduced by the simulations. Also, the red and purple domains that appear at high correlation lengths are present in measurements and simulations. However, especially, the purple regions are much less pronounced in the measured data.

Figure 33 displays the FOURIER-plane appearance of the sub-diffraction metasurfaces at the bottom. As expected for a sub-diffraction grating, no diffraction modes are visible so that only specular reflection is present in the non-disordered metasurface. For uncorrelated disorder, the simulations predict specular reflections as the dominant feature up to $s_d = 40\%$, while at $s_d = 80\%$, isotropic scattering sets in. This is different from the measurements, for which specular reflection is dominant for all uncorrelated disorder strengths. However, the simulations accurately predict the desaturation of specular

features with increasing uncorrelated disorder. The simulations generally predict a more saturated appearance of the FOURIER plane, which comes from differences in the predicted spectral intensities, as can be seen in Fig. 34. Besides that, the simulation model precisely predicts the emergence of a broadened zeroth order for correlated disorder. Both simulations and measurements exhibit slightly more pronounced broadening for smaller correlation lengths and $s_d > 0\%$.

As explained before, it should not go unmentioned that also the measured and simulated spectral data in Fig. 34 represent slightly different quantities.

Most obviously, the simulations differ from the measurements in the predicted linewidth of the resonance. This is to be expected to some extent, since the manufactured metasurfaces always show imperfections that introduce additional damping losses and thus broaden the resonance. Furthermore, the formation of aluminum oxide within the aluminum nanostructures is commonly known to promote differences between theoretical and experimental data [71]. The narrow linewidth of the simulated data is also the reason for the enhanced saturation in the simulated appearances depicted at the bottom of Fig. 33. Besides that, the resonance position is predicted with good agreement for low disorder strengths. For higher disorder strengths, the measured resonances are redshifted, while the simulated resonances shift to shorter wavelengths. Although the resonance shifts are not predicted correctly, the spectral broadening caused by disorder is reproduced well by the CPDA model.

6. CONCLUSION AND OUTLOOK

This tutorial provided the theoretical basis required to understand and implement the CPDA model. We have presented a disorder formalism that allows one to generate plasmonic metasurfaces with a tunable degree of disorder and correlation. We have shown that the disorder formalism is designed such that the location, orientation, and size of individual nanostructures can be manipulated progressively by setting the disorder parameters s_d and l_c . Especially, the positional disorder was quantified using the TPCF and SF, which both are established metrics in different fields of research. The SF was connected with the scattering properties of nanostructure ensembles via the so called SFA, which allows one to separate the contributions from the structure distribution and the individual scattering characteristics of the nanostructures. With these disorder metrics, the influence of the different disorder parameters s_d and l_c was quantified, and the observed effects were discussed. Since the CPDA is capable of computing spectrally resolved, angular, and spatial far-field distributions, the concepts of the FOURIER and image planes were explained using the example of a $4f$ setup. A dedicated color model was introduced that is derived from the sRGB color space and allows one to convert the computed hyperspectral FOURIER- and image-plane intensities into color appearances.

A short overview on the implementation of the CPDA package with the associated disorder and color model was given in Section 3. This overview provided insights on the structure of the developed package and specified the most relevant simulation parameters.

The capabilities of the implemented models were demonstrated, and the consistency of the predictions with theoretical expectations was discussed. It was shown that the model can not only compute the scattering of disordered metasurfaces, but is also able to reproduce the results of recently published metasurface designs [45,72,73] for different polarization states. The CPDA model was compared with the SFA, and excellent agreement was found for the examined metasurfaces. A first step towards truly tailored scattering properties of plasmonic metasurfaces was taken, and the underlying phase-retrieval concepts were explained.

The spectral, spatial, and angular intensities predicted by the CPDA model were validated against Mie theory, FEM simulations, and experiments. While excellent agreement with theory and FEM simulations was found for most of the characteristics, the normalization of the CPDA was shown to be not correct yet. The agreement between the CPDA and experimental data of the FOURIER- and image-plane appearances was mostly very good and exhibited only a slight mismatch in the global tint. Dark features, such as isotropic scattering backgrounds, were generally less pronounced in the experimental data. The spectral agreement with the experiment was satisfactory but showed deviations in the predicted linewidths and amplitudes. However, many of these deviations were traced back to differences in the data acquisition, fabrication inaccuracies, and oxidation of the aluminum nanostructures.

The CPDA model has demonstrated great predictive power for a variety of disordered and very sophisticated plasmonic metasurfaces. As shown in Fig. 35, it is capable of simulating the monochrome scattering properties of metasurfaces with 10,000

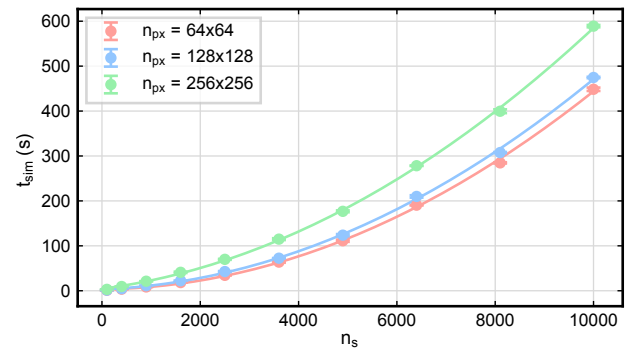


Fig. 35. Computation times for varying numbers of structures and grid resolutions. The mean and standard deviations of the image- and FOURIER-plane computations at $\lambda_0 = 0.6 \mu\text{m}$ are displayed. The resolution of the image- and FOURIER-plane grid is $n_{px} = n_{px,x} \cdot n_{px,y}$. Each set of simulation parameters is computed five times to derive the statistical parameters. All simulations were carried out for n_s aluminum disks of shape $0.12 \times 0.12 \times 0.06 \mu\text{m}^3$ and randomly distributed over intervals $-p_x \cdot (n_x - 1)/2 \leq x < p_x \cdot (n_x - 1)/2$ and $-p_y \cdot (n_y - 1)/2 \leq y < p_y \cdot (n_y - 1)/2$ for $p_x = p_y = 0.5 \mu\text{m}$ and $n_x = n_y = \sqrt{n_s}$. All quadratic polynomial fits (solid lines) have $R^2 > 0.999$ and thus confirm the quadratic dependency on the number of structures. These simulations are executed on a Linux machine with 128 GB RAM and 16 cores to reach high values of n_s . However, note that most simulations here have been calculated on a standard desktop.

nanostructures in only a few minutes with good resolution. The run time is mainly determined by a quadratic dependence on the number of structures [see Eq. (17)] and a linear dependence on the number of pixels and wavelengths. The memory requirements are also governed by the quadratic dependence on the number of structures to store the transfer matrix \hat{T}_M and are mostly independent of the size of the simulation domain. In this tutorial, most simulations were run on a Windows machine with 16 GB RAM and four cores. The simulations in Figs. 31–34 were computed on a Linux machine with 128 GB RAM and 16 cores for speed reasons. However, assuming that the transfer matrix consists of $m = 128$ bit double precision complex entries for n_s structures in $n_{dim} = 3$ dimensions, it is possible to roughly estimate that on a nowadays common $M = 16$ GB desktop machine, simulations with up to $n_s = 10,000$ structures should be possible [$M = m \cdot (n_{dim} \cdot n_s)^2$]. This makes it a very powerful tool for tackling the challenge of tailored scattering under the consideration of structural defects and coupling effects present in real systems. Due to the integration of the sRGB color model, the CPDA is not only applicable for physical computations, but additionally enables to derive the spatial and angular appearances of plasmonic metasurfaces.

Nevertheless, many tasks remain to be done in future work. Some of these tasks revolve around the completion of the CPDA, while others involve the application of the approach on new problems. First and foremost, the correct normalization of the model has to be found so that all simulated properties can be related precisely to the physical reality. Also, the reciprocity theorem can be formulated such that it provides a solution for the forward scattering (transmission) of plasmonic metasurfaces. This is interesting not only as it allows one to predict the

transmission characteristics, but also because the absorption within the metasurface can be deduced from the computed forward and backward scattering. Another measure that would allow one to compute a wider range of metasurfaces is to extend the database of available nanostructure polarizabilities. This particularly concerns the polarizabilities of bigger structures, since a large body of published metasurfaces relies on those. Besides these rather straightforward steps, there are also some steps that are certainly more difficult to implement but still very interesting. First of all, the model would tremendously benefit from the implementation of a substrate beneath the metasurface for the simple reason that the substrate is indispensable in experimental systems. Generally, a formalism that allows one to efficiently incorporate layered structures would yield a model with much broader applicability.

Another yet untackled task is to consider magnetic modes in the CPDA model. This is required to accurately predict the scattering of dielectric metasurfaces, which often exhibit strong magnetic modes. Besides these issues directly related to the CPDA, the quantification of the rotational and dimensional disorder with suitable metrics remains to be done.

Although the results have not been validated at this point, it is possible to examine three-dimensional structure distributions with the implemented CPDA. However, even if three-dimensional metamaterials would certainly yield interesting scattering distributions, it is questionable whether those designs can be fabricated with reasonable effort. From an experimental perspective, the application of the CPDA model on structure distributions with unique long- and short-range orders is of great interest. Hyperuniformity [67–69], MATÉRN type processes [74,75], or random sequential adsorption [76] are very promising disorder-based concepts for enhancing the conversion efficiency of solar cells and creating flexible interfaces, among others [19]. While these structure distributions come from theoretical considerations about order, very sophisticated scattering distributions can be obtained from the application of phase-retrieval algorithms [26]. The underlying concepts have been discussed in this tutorial, but the proof that the CPDA model is a very effective tool for the precise design of angular scattering is still pending.

There is also space for improvement regarding the experimental validation of the CPDA model. Most importantly, the validation of the appearance should not be carried out anymore by directly measuring the RGB appearance. Instead, it is much more reasonable to measure the monochromatic FOURIER- and image-plane intensity distributions and derive the appearances with the same color model used for the simulated data. This way, it is not necessary to consider any differences caused by deviations in the illuminating light source, inaccurate white balances, or differences in the employed color models. Additionally, it allows one to directly compare the measured and simulated scattering characteristics at different wavelengths. Furthermore, the experimentally acquired spectral data should be measured in the zeroth order of the FOURIER plane. This ensures that there are no avoidable ambiguities in the interpretation of the experimental data. It is also advisable to use gold structures in prospective experimental validation measurements, since this avoids the problem of oxidation that aluminum suffers from.

So far, the fabricated metasurfaces are derived from metasurface designs passed to the CPDA model. However, this comes with the disadvantage that inaccuracies originating from the manufacturing process cannot be considered in the simulations. It is conceivable to overcome this problem by extracting the precise location, orientation, and size of the fabricated metasurfaces from scanning electron microscope (SEM) images and feeding these into the simulation model.

APPENDIX A

SYMBOLS

$\hat{\alpha}$	polarizability tensor.
α	polarizability.
c_0	speed of light in vacuum.
C_{sc}	scattering cross section.
c	speed of light in matter.
D	dielectric displacement vector.
δ_f	scaling factor for simulated Fourier-plane size.
δ_i	scaling factor for simulated image-plane size.
Δz	height of integration volume in z direction.
E	electric field.
E	electric field vector.
$\hat{\epsilon}$	relative permittivity tensor/dielectric function tensor.
ϵ	relative permittivity/dielectric function.
FWHM	full width half maximum.
\hat{G}	GREEN's dyadic.
\hat{G}_{far}	GREEN's dyadic for far-field interaction.
G	GREEN's function.
\hat{G}_{inter}	GREEN's dyadic for intermediate-field interaction.
\hat{G}_{near}	GREEN's dyadic for near-field interaction.
H	magnetic field vector.
$\hat{1}$	identity matrix.
j	current density.
k	wavenumber.
k_{\parallel}	in-plane component of the wave vector.
k_{\parallel}	in-plane component of the wave vector.
k_x	x component of the wave vector.
k_y	y component of the wave vector.
k_z	z component of the wave vector.
k	wave vector.
λ	wavelength.
l_c	correlation length.
B	magnetic flux density vector.
$\hat{\mu}$	relative permeability tensor.
μ	relative permeability.
NA	numerical aperture.
n_x	number of structures in x direction.
n_y	number of structures in y direction.
n	refractive index.
$n_{px,x}$	number of pixels in x direction.
$n_{px,y}$	number of pixels in y direction.
p_x	periodicity in x direction.
p_y	periodicity in y direction.
ϕ_i	azimuthal illumination angle.
p	dipole moment.
q_x	spatial frequencies in x direction.
q_y	spatial frequencies in y direction.

(Table continued)

ρ	charge density.
σ_{sc}	differential scattering cross section.
s_d	disorder strength.
\hat{T}_M	transfer matrix.
θ_i	polar illumination angle.
ω	angular frequency.
$\bar{x}(\lambda)$	red color matching function.
ξ	two-point correlation function.
$\bar{y}(\lambda)$	green color matching function.
Z	wave impedance.
$\bar{z}(\lambda)$	blue color matching function.

ACRONYMS

BRDF	bidirectional reflectance distribution function.
CF	correlation function.
CMF	color matching function.
CPDA	coupled point dipole approximation.
FDFD	finite difference frequency domain.
FDTD	finite difference time domain.
FEM	finite element method.
FFT	fast Fourier transform.
FIT	finite integral technique.
FMM	Fourier modal method.
GS	Gerchberg and Saxton.
HIO	hybrid input–output.
LCP	left-handed circularly polarized.
OSS	oversampling smoothness.
PDF	probability density function.
RCP	right-handed circularly polarized.
RMSE	root mean squared error.
RMSLE	root mean squared logarithmic error.
SEM	scanning electron microscope.
SF	structure factor.
SFA	structure factor approximation.
SIM	surface integral method.
T-matrix	transition matrix.
TE	transverse electric.
TM	transverse magnetic.
TPCF	two-point correlation function.
VIM	volume integral method.

Funding. European Research Council (ERC Advanced Grant COMPLEXPLAS); Baden-Württemberg Stiftung; Bundesministerium für Bildung und Forschung; Deutsche Forschungsgemeinschaft (SPP1839-Tailored Disorder).

Disclosures. The authors declare no conflicts of interest.

Data availability. See Code 1, Ref. [77] for data underlying the results presented in this paper.

REFERENCES

- M. G. Moharam and T. K. Gaylord, "Rigorous coupled-wave analysis of planar-grating diffraction," *J. Opt. Soc. Am.* **71**, 811–818 (1981).
- B. T. Draine and P. J. Flatau, "Discrete-dipole approximation for scattering calculations," *J. Opt. Soc. Am. A* **11**, 1491–1499 (1994).
- L. Li, "Fourier modal method for crossed anisotropic gratings with arbitrary permittivity and permeability tensors," *J. Opt. A* **5**, 345–355 (2003).
- T. Weiss, G. Granet, N. A. Gippius, S. G. Tikhodeev, and H. Giessen, "Matched coordinates and adaptive spatial resolution in the Fourier modal method," *Opt. Express* **17**, 8051–8061 (2009).
- J. Niegemann, W. Pernice, and K. Busch, "Simulation of optical resonators using DGT and FDTD," *J. Opt. A* **11**, 114015 (2009).
- B. Gallinet, J. Butet, and O. J. F. Martin, "Numerical methods for nanophotonics: standard problems and future challenges," *Laser Photon. Rev.* **9**, 577–603 (2015).
- G. Unger, A. Trügler, and U. Hohenester, "Novel modal approximation scheme for plasmonic transmission problems," *Phys. Rev. Lett.* **121**, 246802 (2018).
- P. Lalanne, W. Yan, A. Gras, C. Sauvan, J.-P. Hugonin, M. Besbes, G. Demézy, M. D. Truong, B. Gralak, F. Zolla, A. Nicolet, F. Binkowski, L. Zschiedrich, S. Burger, J. Zimmerling, R. Remis, P. Urbach, H. T. Liu, and T. Weiss, "Quasinormal mode solvers for resonators with dispersive materials," *J. Opt. Soc. Am. A* **36**, 686–704 (2019).
- C. Carlson and S. Hughes, "Disordered nanophotonic surfaces for enhanced light collection in semiconductor solar cells," *J. Opt. Soc. Am. B* **35**, 1093–1104 (2018).
- Y. J. Donie, M. Smeets, A. Egel, F. Lentz, J. B. Preinfalk, A. Mertens, V. Smirnov, U. Lemmer, K. Bittkau, and G. Gomard, "Light trapping in thin film silicon solar cells via phase separated disordered nanopillars," *Nanoscale* **10**, 6651–6659 (2018).
- S. Nanz, A. Abass, P. M. Piechulla, A. Sprafke, R. B. Wehrspohn, and C. Rockstuhl, "Strategy for tailoring the size distribution of nanospheres to optimize rough backreflectors of solar cells," *Opt. Express* **26**, A111–A123 (2018).
- B. Redding, S. F. Liew, R. Sarma, and H. Cao, "Compact spectrometer based on a disordered photonic chip," *Nat. Photonics* **7**, 746–751 (2013).
- W. Hartmann, P. Varytis, H. Gehring, N. Walter, F. Beutel, K. Busch, and W. Pernice, "Broadband spectrometer with single-photon sensitivity exploiting tailored disorder," *Nano Lett.* **20**, 2625–2631 (2020).
- L. Maiwald, S. Lang, D. Jalas, H. Renner, A. Y. Petrov, and M. Eich, "Ewald sphere construction for structural colors," *Opt. Express* **26**, 11352–11365 (2018).
- D. T. Meiers, M.-C. Heep, and G. von Freymann, "Invited article: Bragg stacks with tailored disorder create brilliant whiteness," *APL Photon.* **3**, 100802 (2018).
- F. Sterl, E. Herkert, S. Both, T. Weiss, and H. Giessen, "Shaping the color and angular appearance of plasmonic metasurfaces with tailored disorder," *ACS Nano* **15**, 10318–10327 (2021).
- K. Vynck, R. Pacanowski, A. Agreda, A. Dufay, X. Granier, and P. Lalanne, "The visual appearances of disordered optical metasurfaces," *Nat. Mater.* **21**, 1035–1041 (2022).
- M. Rothhammer, C. Zollfrank, K. Busch, and G. von Freymann, "Tailored disorder in photonics: learning from nature," *Adv. Opt. Mater.* **9**, 2100787 (2021).
- P. M. Piechulla, L. Muehlenbein, R. B. Wehrspohn, S. Nanz, A. Abass, C. Rockstuhl, and A. Sprafke, "Fabrication of nearly-hyperuniform substrates by tailored disorder for photonic applications," *Adv. Opt. Mater.* **6**, 1701272 (2018).
- D. Wang and P. Schaaf, "Plasmonic nanosponges," *Adv. Phys. X* **3**, 1456361 (2018).
- Q. Yuan, J. Döll, H. Romanus, H. Wang, H. Bartsch, A. Albrecht, M. Hoffmann, P. Schaaf, and D. Wang, "Surface-nanostructured Al–AlN composite thin films with excellent broad-band antireflection properties fabricated by limited reactive sputtering," *ACS Appl. Nano Mater.* **1**, 1124–1130 (2018).
- M. Ziegler, A. Dathe, K. Pollok, F. Langenhorst, U. Hübner, D. Wang, and P. Schaaf, "Metastable atomic layer deposition: 3D self-assembly toward ultradark materials," *ACS Nano* **14**, 15023–15031 (2020).
- F. Mayer, D. Ryklin, I. Wacker, R. Curticean, M. Čalkovský, A. Niemeyer, Z. Dong, P. A. Levkin, D. Gerthsen, R. R. Schröder, and M. Wegener, "3D two-photon microprinting of nanoporous architectures," *Adv. Mater.* **32**, 2002044 (2020).

24. D. Neshev and I. Aharonovich, "Optical metasurfaces: new generation building blocks for multi-functional optics," *Light Sci. Appl.* **7**, 58 (2018).
25. M. Khorasaninejad, F. Aieta, P. Kanhaiya, M. A. Kats, P. Genevet, D. Rousso, and F. Capasso, "Achromatic metasurface lens at telecommunication wavelengths," *Nano Lett.* **15**, 5358–5362 (2015).
26. R. Zhao, B. Sain, Q. Wei, C. Tang, X. Li, T. Weiss, L. Huang, Y. Wang, and T. Zentgraf, "Multichannel vectorial holographic display and encryption," *Light Sci. Appl.* **7**, 95 (2018).
27. Y. Wang, C. Zhao, J. Wang, X. Luo, L. Xie, S. Zhan, J. Kim, X. Wang, X. Liu, and Y. Ying, "Wearable plasmonic-metasurface sensor for noninvasive and universal molecular fingerprint detection on biointerfaces," *Sci. Adv.* **7**, eabe4553 (2021).
28. P. Georgi, M. Massaro, K.-H. Luo, B. Sain, N. Montaut, H. Herrmann, T. Weiss, G. Li, C. Silberhorn, and T. Zentgraf, "Metasurface interferometry toward quantum sensors," *Light Sci. Appl.* **8**, 70 (2019).
29. S. Fasold, S. Linß, T. Kawde, M. Falkner, M. Decker, T. Pertsch, and I. Staude, "Disorder-enabled pure chirality in bilayer plasmonic metasurfaces," *ACS Photon.* **5**, 1773–1778 (2018).
30. E. A. Muljarov, W. Langbein, and R. Zimmermann, "Brillouin-wigner perturbation theory in open electromagnetic systems," *Europhys. Lett.* **92**, 50010 (2010).
31. S. Both and T. Weiss, "Resonant states and their role in nanophotonics," *Semicond. Sci. Technol.* **37**, 013002 (2022).
32. S. V. Lobanov, G. Zorinians, W. Langbein, and E. A. Muljarov, "Resonant-state expansion of light propagation in nonuniform waveguides," *Phys. Rev. A* **95**, 053848 (2017).
33. S. Neale and E. A. Muljarov, "Resonant-state expansion for planar photonic crystal structures," *Phys. Rev. B* **101**, 155128 (2020).
34. E. A. Muljarov and W. Langbein, "Resonant-state expansion of dispersive open optical systems: creating gold from sand," *Phys. Rev. B* **93**, 075417 (2016).
35. E. A. Muljarov, "Full electromagnetic Green's dyadic of spherically symmetric open optical systems and elimination of static modes from the resonant-state expansion," *Phys. Rev. A* **101**, 053854 (2020).
36. S. Uppendar, I. Allayarov, M. A. Schmidt, and T. Weiss, "Analytical mode normalization and resonant state expansion for bound and leaky modes in optical fibers—an efficient tool to model transverse disorder," *Opt. Express* **26**, 22536–22546 (2018).
37. S. G. Tikhodeev, E. A. Muljarov, W. Langbein, N. A. Gippius, H. Giessen, and T. Weiss, "Influence of disorder on a Bragg microcavity," *J. Opt. Soc. Am. B* **38**, 139–150 (2021).
38. A. Egel, L. Pattelli, G. Mazzamuto, D. S. Wiersma, and U. Lemmer, "Celes: Cuda-accelerated simulation of electromagnetic scattering by large ensembles of spheres," *J. Quant. Spectrosc. Radiat. Transfer* **199**, 103–110 (2017).
39. D. Theobald, D. Beutel, L. Borgmann, H. Mescher, G. Gomard, C. Rockstuhl, and U. Lemmer, "Simulation of light scattering in large, disordered nanostructures using a periodic T-matrix method," *J. Quant. Spectrosc. Radiat. Transfer* **272**, 107802 (2021).
40. A. Abass, M. Zilk, S. Nanz, S. Fasold, S. Ehrhardt, T. Pertsch, and C. Rockstuhl, "A Green's function based analytical method for forward and inverse modeling of quasi-periodic nanostructured surfaces," *J. Appl. Phys.* **122**, 183103 (2017).
41. P. Lalanne, W. Yan, K. Vynck, C. Sauvan, and J.-P. Hugonin, "Light interaction with photonic and plasmonic resonances," *Laser Photon. Rev.* **12**, 1700113 (2018).
42. I. M. Fradkin, S. A. Dyakov, and N. A. Gippius, "Fourier modal method for the description of nanoparticle lattices in the dipole approximation," *Phys. Rev. B* **99**, 075310 (2019).
43. V. G. Kravets, A. V. Kabashin, W. L. Barnes, and A. N. Grigorenko, "Plasmonic surface lattice resonances: a review of properties and applications," *Chem. Rev.* **118**, 5912–5951 (2018).
44. F. E. Nicodemus, "Reflectance nomenclature and directional reflectance and emissivity," *Appl. Opt.* **9**, 1474–1475 (1970).
45. X. Yin, T. Steinle, L. Huang, T. Taubner, M. Wuttig, T. Zentgraf, and H. Giessen, "Beam switching and bifocal zoom lensing using active plasmonic metasurfaces," *Light Sci. Appl.* **6**, e17016 (2017).
46. L. Novotny and B. Hecht, *Principles of Nano-Optics*, 2nd ed. (Cambridge University, 2012).
47. C. Sauvan, J. P. Hugonin, I. S. Maksymov, and P. Lalanne, "Theory of the spontaneous optical emission of nanosize photonic and plasmon resonators," *Phys. Rev. Lett.* **110**, 237401 (2013).
48. J. Yang, J. P. Hugonin, and P. Lalanne, "Near-to-far field transformations for radiative and guided waves," *ACS Photon.* **3**, 395–402 (2016).
49. T. Weiss, M. Schäferling, H. Giessen, N. A. Gippius, S. G. Tikhodeev, W. Langbein, and E. A. Muljarov, "Analytical normalization of resonant states in photonic crystal slabs and periodic arrays of nanoantennas at oblique incidence," *Phys. Rev. B* **96**, 045129 (2017).
50. T. Weiss and E. A. Muljarov, "How to calculate the pole expansion of the optical scattering matrix from the resonant states," *Phys. Rev. B* **98**, 085433 (2018).
51. S. D. Landy and A. S. Szalay, "Bias and variance of angular correlation functions," *Astrophys. J.* **412**, 64–71 (1993).
52. M. Kerscher, I. Szapudi, and A. S. Szalay, "A comparison of estimators for the two-point correlation function," *Astrophys. J.* **535**, L13 (2000).
53. H. Liu and S. J. Paddison, "Direct calculation of the x-ray structure factor of ionic liquids," *Phys. Chem. Chem. Phys.* **18**, 11000–11007 (2016).
54. J. M. Rodenburg, A. C. Hurst, A. G. Cullis, B. R. Dobson, F. Pfeiffer, O. Bunk, C. David, K. Jefimovs, and I. Johnson, "Hard-x-ray lensless imaging of extended objects," *Phys. Rev. Lett.* **98**, 034801 (2007).
55. H. N. Chapman and K. A. Nugent, "Coherent lensless x-ray imaging," *Nat. Photonics* **4**, 833–839 (2010).
56. Y. Shechtman, Y. C. Eldar, O. Cohen, H. N. Chapman, J. Miao, and M. Segev, *Phase Retrieval with Application to Optical Imaging* (2014).
57. J. A. Rodriguez, R. Xu, C. C. Chen, Y. Zou, and J. Miao, "Oversampling smoothness: an effective algorithm for phase retrieval of noisy diffraction intensities," *J. Appl. Crystallogr.* **46**, 312–318 (2013).
58. J. C. Spence, U. Weierstall, and M. Howells, "Phase recovery and lensless imaging by iterative methods in optical, x-ray and electron diffraction," *Philos. Trans. R. Soc. A* **360**, 875–895 (2002).
59. R. W. Gerchberg and W. O. Saxton, "Practical algorithm for the determination of phase from image and diffraction plane pictures," *Optik* **35**, 237–246 (1972).
60. J. R. Fienup, "Phase retrieval algorithms: a comparison," *Appl. Opt.* **21**, 2758–2769 (1982).
61. M. Matsumoto and T. Nishimura, "Mersenne twister: a 623-dimensionally equidistributed uniform pseudo-random number generator," *ACM Trans. Model. Comput. Simul.* **8**, 3–30 (1998).
62. X. Yin, M. Schäferling, B. Metzger, and H. Giessen, "Interpreting chiral nanophotonic spectra: the plasmonic Born-Kuhn model," *Nano Lett.* **13**, 6238–6243 (2013).
63. N. Yu and F. Capasso, "Flat optics with designer metasurfaces," *Nat. Mater.* **13**, 139–150 (2014).
64. N. Yu, P. Genevet, M. A. Kats, F. Aieta, J.-P. Tetienne, F. Capasso, and Z. Gaburro, "Light propagation with phase reflection and refraction," *Science* **334**, 333–337 (2011).
65. S. A. Maier, *Plasmonics: Fundamentals and Applications* (Springer, 2007).
66. P. M. Piechulla, B. Fuhrmann, E. Slivina, C. Rockstuhl, R. B. Wehrspohn, and A. N. Sprafke, "Tailored light scattering through hyperuniform disorder in self-organized arrays of high-index nanodisks," *Adv. Opt. Mater.* **9**, 2100186 (2021).
67. S. Torquato and F. H. Stillinger, "Local density fluctuations, hyperuniformity, and order metrics," *Phys. Rev. E* **68**, 041113 (2003).
68. S. Torquato, "Hyperuniformity and its generalizations," *Phys. Rev. E* **94**, 022122 (2016).
69. S. Torquato, "Disordered hyperuniform heterogeneous materials," *J. Phys. Condens. Matter* **28**, 414012 (2016).
70. G. Zheng, H. Mühlenbernd, M. Kenney, G. Li, T. Zentgraf, and S. Zhang, "Metasurface holograms reaching 80% efficiency," *Nat. Nanotechnol.* **10**, 308–312 (2015).
71. M. W. Knight, N. S. King, L. Liu, H. O. Everitt, P. Nordlander, and N. J. Halas, "Aluminum for plasmonics," *ACS Nano* **8**, 834–840 (2014).
72. J. Ratzsch, J. Karst, J. Fu, M. Ubl, T. Pohl, F. Sterl, C. Malacrida, M. Wieland, B. Reineke, T. Zentgraf, S. Ludwigs, M. Hentschel, and H. Giessen, "Electrically switchable metasurface for beam steering using PEDOT polymers," *J. Opt.* **22**, 124001 (2020).

73. J. Karst, M. Floess, M. Ubl, C. Dingler, C. Malacrida, T. Steinle, S. Ludwigs, M. Hentschel, and H. Giessen, "Electrically switchable metallic polymer nanoantennas," *Science* **374**, 612–616 (2021).
74. C. D. Kemp and B. Matern, "Spatial variation," in *The Statistician* (1988).
75. J. Møller, M. L. Huber, and R. L. Wolpert, "Perfect simulation and moment properties for the Matérn type III process," in *Stochastic Processes and Their Applications* (2010), pp. 2142–2158.
76. B. Widom, "Random sequential addition of hard spheres to a volume," *J. Chem. Phys.* **44**, 3888–3894 (1966).
77. E. Herkert, "CPDA," GitHub (2022), <https://github.com/EdKaHe/cpda>.